COARSE-GRAINING OF ATOMISTIC DESCRIPTION AT FINITE TEMPERATURE

Thesis by

Yashashree Kulkarni

In Partial Fulfillment of the Requirements

for the Degree of

Doctor of Philosophy

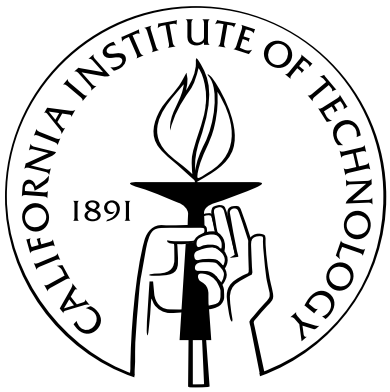

California Institute of Technology

Pasadena, California

2007

(Defended October 20, 2006)

© 2007

Yashashree Kulkarni

All Rights Reserved

To my parents

Acknowledgements

I take this opportunity to acknowledge all the people who have been a part of my experience at Caltech and who have made this journey a uniquely enriching one. I will always be indebted to my advisor, Professor Michael Ortiz, for giving me the opportunity to work with him and for his significant contribution to my growth as a researcher. His acute insight, the breadth and depth of his knowledge base, and his amazing source of ideas are indeed inspiring. I would also like to thank him for his constant encouragement and support during the course of this work.

I would like to express my sincere gratitude to Professor Marsden, Professor Bhattacharya, Professor Ravichandran, and Dr. Knap for kindly taking time out of their busy schedules to be on my defense committee and for providing valuable input on my thesis. I am thankful to Professor Marsden for the insightful discussions on averaging and the WKB method. I would also like to thank Professor Bhattacharya for being on my candidacy committee and for his valuable feedback during the course of this work.

Jaroslaw Knap, my computing guru, played a crucial role in the computational aspects of this work. I am very grateful to him for always being there, even after leaving Caltech, whenever I needed his help in resolving issues with the implementation or interpreting some of the simulation results. I also wish to thank him for his quasicontinuum code, which was used for implementing the methods proposed in this work.

I would also like to thank Dr. Laurent Stainier for interesting discussions on the variational formulation of rate problems and for suggesting the insightful adiabatic tests.

It has been a pleasure to know Lydia Suarez and Marta Kahl, the administrative pillars of our group, whose efficient working keeps us so comfortably focused on our work. I would also like to thank Lydia for all the wonderful conversations and for the innumerable things that I have gone knocking on her door for.

I have enjoyed the company of many wonderful friends within the group and outside. Special thanks go to Amir, Anu, George, Matias, Radhika, Raquel, Sujata, and Vikram, who have made my Caltech experience memorable. I would also like to acknowledge Lotty, my apartment-mate for three years. For all the interesting conversations, for exposing me to world cuisines and music, and for her being there in my moments of crisis and joy, living with her has truly been a home away from home. Our playful roommate, Cleo (our cat), also deserves a special mention for being a source of pure joy and for being completely oblivious to the fact.

Words seem futile when attempting to express my gratitude to my parents. They have and will always be my source of strength. From being the"little Yashashree" to whom my mother's thesis was dedicated to being at this point writing my own, what more can I say than my inadequate gesture of dedicating this thesis to them. I am also grateful to my uncle Manohar and aunt Sushama, who stood behind me through the different phases of my PhD, providing encouragement and sharing experiences. Finally, I would like to acknowledge my husband, Ashutosh Agrawal, for his unfailing love and support in spite of the long-distance marriage. Brainstorming with me on my research problems, helping me find a direction when I was groping in darkness, and sharing (and bearing !) my highs and lows, he has come to be my anchor, for which I shall always be grateful.

Abstract

This thesis presents a computational method for seamlessly bridging the atomistic and the continuum realms at finite temperature. The theoretical formulation is based on the static theory of the quasicontinuum and extends it to model non-equilibrium finite temperature material response.

At non-zero temperature, the problem of coarse-graining is compounded by the presence of multiple time scales in addition to multiple spatial scales. We address this problem by first averaging over the thermal motion of atoms to obtain an effective temperature-dependent energy on the macroscopic scale. Two methods are proposed to this end. The first method is developed as a variational mean field approximation which yields local thermodynamic potentials such as the internal energy, the free energy, and the entropy as phase averages of appropriate phase functions. The chief advantage of this theory is that it accounts for the anharmonicity of the interaction potentials, albeit numerically, unlike many methods based on statistical mechanics which require the quasi-harmonic approximation for computational feasibility. Furthermore, the theory reduces to the classical canonical ensemble approach of Gibbs under the quasi-harmonic approximation for perfect, isotropic, infinite crystals subjected to uniform temperature. In the second method, based on perturbation analysis, the internal energy is derived as an effective Hamiltonian of the atomistic system by treating the thermal fluctuations as perturbations about an equilibrium configuration.

These energy functionals are then introduced into the quasicontinuum theory, which facilitates spatial coarse-graining of the atomistic description. Finally, a variational formulation for simulating rate problems, such as heat conduction, using the quasicontinuum method is developed. This is achieved by constructing a joint incremental energy functional whose Euler-Lagrange equations yield the equilibrium equations as well as the time-discretized heat equation.

We conclude by presenting the results for numerical validation tests for the thermal expansion coefficient and the specific heat for some materials and compare them with classical theory, molecular dynamics results, and experimental data. Some illustrative examples of thermo-mechanical coupled problems such as heat conduction in a deformable solid, adiabatic tension test, and finite temperature nanoindentation are also presented which show qualitative agreement with expected behavior and demonstrate the applicability of the method.

Contents

List of Figures

Chapter 1

Introduction

That all natural phenomena are inherently multiscale is a fascinating notion. In the context of material response, it means that what we see on the scale of observation is a manifestation of the mechanics of the underlying microstructure and microscopic processes. Furthermore, there is an order in this hierarchy, and typically, we can distinguish these length scales as (i) the atomic scale at which the interactions are dictated by quantum mechanics, (ii) the microscopic scale at which the dynamics of the atoms and molecules is the key player, and (iii) the macroscopic scale at which the system may be treated as a continuous medium and the physical behavior is governed by the laws of continuum thermodynamics. Phenomena at these length scales also exhibit an hierarchy of time scales.

What makes this multiscale nature even more intriguing is that our perception of physical quantities and phenomena also has to change across the scales. A primary example that illustrates this point and which is the focus of this work is the concept of temperature. A measure of heat in a body is an elementary understanding of temperature. In thermodynamics, it is introduced empirically as a state variable associated with a system in equilibrium. The zeroth law states that when two systems are brought into contact, they are in thermal equilibrium only when their temperatures are equal. This need for an empirical definition for the temperature field stems from the fact that the origin of the notion of temperature

lies in the microscopic nature of material. At this scale, macroscopic entities such as stress, strain, and temperature result purely from the dynamics of the atoms or molecules. In classical theory, this implies solving Newton's equations of motion for the atomic degrees of freedom given an interaction potential. Then, the temperature may be defined naturally as the "average" energy of the atomic oscillations. This link between the macroscopic temperature field and microscopic dynamics has been well-understood owing to the fundamental contributions of Boltzmann, Gibbs and others to statistical thermodynamics [6, 41, 45]. As we shall see in Chapter 2, based on the canonical ensemble of Gibbs, the temperature for a system in thermal equilibrium can be defined rigorously as the phase average of the kinetic energy of the system using an appropriate probability density –

$$\frac{3}{2}k_B T = \langle \frac{1}{2} | \boldsymbol{p} |^2 \rangle . \tag{1.1}$$

Thus, established theory ranging from quantum mechanics to statistical mechanics to continuum thermodynamics and efficient computational models such as molecular dynamics, monte carlo methods, and finite element analysis exist at each of these spatio-temporal scales, which have been rigorously developed and used for traditional scientific pursuit and engineering applications.

1.1 Motivation for multiscale modelling of materials

Recent years have witnessed a drive towards developing unified multiscale methods to facilitate material modelling across several spatial and temporal scales. The rapidly progressing area of nanotechnology, with its miniaturization of devices and efforts to design materials with specific properties at small scales, has provided the primary impetus. Furthermore,

ever-increasing computing power has established computational modelling as a complement to theory and experiment for studying natural phenomena. Although the same has also made possible the simulation of very large fully-atomistic systems to study their behavior across scales using atomistic models, the interest in multiscale analysis is immense. This is largely due to the fact that in atomistic methods, the length scale is determined by interatomic spacing, which is on the order of a few angstroms, while a typical time step in molecular dynamics, for instance, is of the order of femtoseconds. Evidently, this imposes a severe limitation on the size of the material sample and the time span of the process that can be modelled. Thus, in the context of materials science, multiscale modelling may be viewed as a paradigm whose ultimate goal is the predictive simulation of full-scale systems on the sole basis of fundamental theories, thereby

- reducing empiricism from macroscopic models by establishing a link between macroscopic material response and the underlying microscopic processes, and
- facilitating the simulation of material response at length and time scales inaccessible to atomistic models.

1.2 Brief review of some existing methods

Several multiscale methods have been developed till date [24] such as the quasicontinuum method (QC), the heterogenous multiscale method (HMM), the macroscopic atomistic *ab initio* dynamics (MAAD), and the coarse-grained molecular dynamics method (CGMD), to name a few. The basic philosophy of the methods other than QC is the efficient coupling of an atomistic model, such as molecular dynamics, with a macroscopic model. They are distinct with regards to the coupling technique, the pathway of information exchange between

the different scales and applicability. HMM was developed by E and Engquist [11, 12] as a general framework for designing numerical methods for dynamical problems and is capable of employing different physical models at different scales. It is a top-down model in that the microscopic solver is used only to supplement the macroscopic model wherever information from the fine scale is needed. It has been shown to have a wide applicability to modelling the behavior of fluids as well as solids. MAAD was developed by Abraham and coworkers [24] to address problems involving several length scales and combines the quantum-mechanical tight binding approach, molecular dynamics and the finite element method. One of the limitations of this approach is that the time-step used in the entire domain is that of the domain of quantum mechanics, which may be a computational overburden. CGMD was developed by Rudd and Broughton [31] and bears some resemblance with QC in that both are based on constructing an effective macroscopic energy for the system from atomistics. It is derived solely from the molecular dynamics method and uses statistical ensemble averages to obtain the coarse-grained description. Their basic idea is to derive the equations of motion for a mean displacement field defined on the nodes. MAAD and CGMD have been effectively applied to dynamic problems such as crack propagation. Since all these methods can support dynamics and exploit atomistic models at the fine scale, they are suitable for finite temperature calculations.

The static theory of the quasicontinuum was originally developed by Tadmor et al. [38] and furnishes a computational scheme for seamlessly bridging the atomistic and the continuum realms. This is achieved by introducing kinematic constraints such that full atomistic resolution is retained in the region of interest, such as defects, whereas coarse-graining is systematically introduced as we move away from this region and the displacement field becomes slow varying on the scale of the lattice. The equilibrium configurations are deter-

mined by minimizing the energy of the system constructed from the interatomic potential. An appealing feature of the QC method is that it is "seamless", which means that the energy calculation in the fine region as well as the coarse-grained region is based purely on the atomistic model. Hence, there are no distinct interfaces separating the regions with varying degree of coarse-graining. Different variants of the QC theory have been developed and applied to many applications such as nanoindentation, dislocations, atomic scale fracture, grain boundaries, and nanovoids [25, 26, 27]. However, one of the main limitations of the quasicontinuum method is that it is a static theory and, hence, energy minimization is performed at zero temperature.

1.3 Finite temperature QC: existing methods and challenges

Temperature plays an important role in many physical phenomena. The thermal energy of the system affects processes such as dislocation nucleation and propagation, void growth, and, under extreme conditions, can also lead to failure by melting. Moreover, thermal expansion also changes the properties of the material (such as thermal softening) and consequently affects the material response. An example to illustrate the effect of temperature is the failure of a nanowire carrying current and having a geometric defect. The failure may occur by melting or necking in the region of the defect, as the current causes an increase in temperature due to Joule heating.

However, the problem of incorporating finite temperature effects in the quasicontinuum theory is a challenging one due to many reasons. As described earlier, at finite temperature, atoms oscillate about their equilibrium positions and temperature is defined as the statistical average of the energy contained in the phonons or the thermal fluctuations of the atoms. Thus, the conversion between phonons and temperature requires some kind of

averaging. Moreover, the time period of these fluctuations is on the order of picoseconds. However, macroscopic processes such as thermal expansion have much longer relaxation times. Consequently, the problem of coarse-graining at finite temperature is compounded by the presence of multiple time scales in addition to multiple spatial scales. The seamlessness of the QC method also adds to the complexity of the problem of adding thermal effects in the form of atomistic dynamics in the atomistic zone and of temperature in the coarse-grained region.

Some effective methods have been proposed to date to address this issue. The work of Shenoy et al. [33] is based on deriving an effective coarse-grained free energy for the system by integrating out the constrained degrees of freedom using the canonical distribution. The calculation is simplified further by assuming the Einstein model to obtain the local frequencies, and the resulting free energy is minimized using Monte Carlo simulations. It has been used to study the temperature dependence of the core structure of dislocations in Al. Another method has been proposed by Wu and coworkers [43] in which they define a coarse-grained partition function based on the canonical ensemble but depending only the representative atoms. The coarse-grained energy and nodal forces are derived from it by computing phase averages, which are evaluated using Monte Carlo simulations. Dupuy et al. [10] address this problem by integrating MD with the quasicontinuum framework. Their basic idea is also to derive an effective potential energy by integrating out the constrained degrees of freedom. The equations of motion of representative atoms are derived from the coarse-grained Hamiltonian. The method has been used to show the temperature dependence of nanoindentation in Al. One of the limitations of the methods proposed by Shenoy et al. and Dupuy et al. is that they employ the local quasi-harmonic approximation for computational efficiency, which restricts them to temperatures about half the melting point

of the material. More importantly, all the above methods have so far been developed only for equilibrium problems at constant temperature. Thus, due to these limitations of existing methods, the problem of adding temperature effects to QC merits further investigation in order to develop an extension of the quasicontinuum theory that retains all the attractive features and also possesses wider applicability in terms of finite temperature phenomena.

As a first step to this end, we propose a three-dimensional non-equilibrium finite temperature version of the theory of quasicontinuum. This goal is achieved in two steps. The basic idea is to first eliminate dependence on the thermal motion of the atoms by averaging and obtaining temperature-dependent potentials. Thus, the energy of the oscillations is represented in the macroscopic energy functional through the dependence on temperature. We propose two methods for achieving this coarse-graining on the time scale. One method is developed as a mean field theory and uses the principle of maximum entropy to obtain the probability distribution functions for the system. The other method is based on perturbation theory, or formal asymptotics, to arrive at an effective Hamiltonian for the atomistic system which may be interpreted as the internal energy for systems undergoing quasistatic processes. Finally, we incorporate the energy functionals furnished by the aforementioned methods into the quasicontinuum framework to achieve a seamless coarse-graining on the spatial scale. We also extend this framework for simulating non-equilibrium processes such as heat conduction. This is based on the work of Yang et al. [44] on the variational formulation of rate problems for general dissipative solids. This enables the quasicontinuum method to be applied to problems such as thermal expansion, heat transport through the crystal under non-uniform temperature, and thermo-mechanical coupled phenomena.

1.4 Organization of the thesis

The thesis is structured as follows. Chapter 2 presents the theoretical formulation of the method based on the principle of maximum entropy. The probability distribution functions for the atomistic system are derived and used to obtain thermodynamic potentials. The chapter concludes with some simple analytical results, providing insight into the method and establishing a link with statistical mechanics. In Chapter 3, we apply this approximation scheme to develop a finite temperature version of the quasicontinuum method. A variational formulation for extending QC to simulate heat conduction through a crystal is proposed. Chapter 4 presents the theoretical formulation for the averaging scheme based on perturbation theory. The scope of the method and its integration with the quasicontinuum method are discussed. In Chapter 5, we analyze the proposed methods by way of computations. The results for various validation tests simulating bulk properties of materials are discussed. The applicability of the method is demonstrated by way of illustrative examples such as heat conduction in a deformable solid, adiabatic tension tests, and finite temperature nanoindentation. We conclude by summarizing the highlights and limitations of the work and presenting some avenues for future investigations in Chapter 6.

Chapter 2

The *max-ent* method

In this chapter, we propose a computational method based on maximum entropy formalism for coarse-graining atomistic dynamics at finite temperature. As in statistical mechanics, the basic idea is to account for the energy contained in the thermal oscillations of the atoms to obtain effective macroscopic thermodynamic potentials while circumventing the treatment of all the atomic degrees of freedom. We achieve this goal by constructing a probability distribution function for the system by way of a mean field approximation. Owing to its development from the maximum entropy principle, we shall refer to this method as the *max-ent* method in subsequent sections. The key distinction of this approach from statistical thermodynamics based on the Gibbs canonical ensemble is that we impose local constraints on the mechanics of the atoms instead of constraining the energy, thereby obtaining local analogs for the probability distribution functions which are Gaussian in form. This imparts the method its two main features:

- ability to derive *local* forms of the thermodynamic potentials, which enables the modelling of non-equilibrium phenomena; and
- ability to account for the *anharmonicity* of the interatomic potentials, albeit numerically, in the macroscopic free energy.

The chapter is structured as follows. In section 2.1, we present an outline of the maximum entropy principle and use it to obtain local probability distribution functions and partition functions. Section 2.2 presents the derivation of some thermodynamic potentials from appropriate phase functions. In section 2.3, we discuss our approach as a variational mean field theory. In section 2.4, we demonstrate the application of the *max-ent* approach in calculating the internal energy and the free energy for some empirical interaction potentials. Section 2.5 aims to provide a deeper insight into the implications of the *max-ent* approach by way of some simple analytical results and their comparison with those derived from statistical mechanics.

2.1 Local *max-ent* distribution

Let us consider a system of N atoms in configuration space X. Let $\boldsymbol{q} \in X \equiv \mathbb{R}^{3N}$ represent the array of atomic positions and $\boldsymbol{p} \in Y \equiv \mathbb{R}^{3N}$ be the array of corresponding momenta. For simplicity of subsequent calculations, let $\boldsymbol{q}$ and $\boldsymbol{p}$ be mass-reduced coordinates defined as

$$\boldsymbol{q}_a \rightarrow \frac{1}{\sqrt{m_a}}\,\boldsymbol{q}_a \;,\;\; \boldsymbol{p}_a \rightarrow \sqrt{m_a}\,\boldsymbol{p}_a \,, \tag{2.1}$$

where $\boldsymbol{q}_a$ and $\boldsymbol{p}_a$ denote the position and the momentum of atom a. Then, the Hamiltonian of the system is

$$H(\boldsymbol{q},\boldsymbol{p}) = \frac{1}{2}|\boldsymbol{p}|^2 + V(\boldsymbol{q}) \,, \tag{2.2}$$

$V(\boldsymbol{q})$ being the potential energy of the system. Thus, $(\boldsymbol{q},\boldsymbol{p})$ denotes a point in the phase space $X \times Y$. Any function $f(\boldsymbol{q},\boldsymbol{p})$ whose instantaneous value can be completely determined by the microstate, i.e., the positions and momenta of the atoms at that instant of time, is referred to as a phase function. According to a fundamental premise of statistical mechanics

[6, 41], there exists a function, $p(\boldsymbol{q}, \boldsymbol{p}) \geq 0$, known as the probability distribution function and interpreted as the probability that the system be at point $(\boldsymbol{q}, \boldsymbol{p})$ in the phase space. The phase average of a function $f(\boldsymbol{q}, \boldsymbol{p})$ with respect to $p(\boldsymbol{q}, \boldsymbol{p})$ is defined as

$$\langle f \rangle = \frac{1}{N! h^{3N}} \int_{\Gamma} p\, f \, d\boldsymbol{q}\, d\boldsymbol{p}\,, \tag{2.3}$$

where we have used the following to simplify the notation:

$$d\boldsymbol{q}\, d\boldsymbol{p} \equiv \prod_{a=1}^{N} \prod_{i=1}^{3} dq_{ai} dp_{ai}\,.$$

Γ denotes the phase space and h is the Planck's constant. The factor $(N!\, h^{3N})^{-1}$ arises from taking the classical limit of the analog of the phase averaging operation in quantum mechanics. It is also essential for the entropy to be extensive in classical statistical thermodynamics.

Principle of maximum entropy

We now wish to determine the probability distribution of the system under consideration based on the principle of maximum entropy [19]. To this end, we define the global entropy of the system as postulated by Boltzmann

$$S = -\frac{k_B}{N! h^{3N}} \int_{\Gamma} p\, \log p \, d\boldsymbol{q}\, d\boldsymbol{p}\,, \tag{2.4}$$

where k_B is the Boltzmann constant introduced as a proportionality constant. The principle of maximum entropy is very well established in the field of statistical mechanics and has its origin in the information-theoretical point of view of the notion of entropy. Information

theory was first introduced in statistical mechanics by Jaynes [16]. From this perspective, entropy is defined as a measure of the uncertainty in the information about a system of particles. For instance, let us consider a thought experiment of observing a given system at an arbitrary instant of time. Any point $(\boldsymbol{q}, \boldsymbol{p})$ in the phase space accessible to the system constitutes an outcome. Then, the entropy defined by Eq. (2.4) is the uncertainty associated with the experiment. The principle of maximum entropy then states that *the least biased probability distribution function maximizes the entropy of the system subject to all the imposed constraints or the information about the system which is already known.* Thus, our objective is to find the probability distribution that maximizes the entropy of the system subject to the following constraints. First, the probability distribution should satisfy the normalization condition

$$\frac{1}{N! h^{3N}} \int_{\Gamma} p \; d\boldsymbol{q} \, d\boldsymbol{p} = 1 \,, \tag{2.5}$$

which simply means that the system certainly has to be at some point in the phase space at any instant of time. Suppose in addition that we have additional knowledge of the configuration of the ensemble. In particular, suppose that we know that atom a moves in the vicinity of point $\bar{\boldsymbol{q}}_a$ with standard deviation $\sqrt{3}\,\tau_a$ and has momentum in the vicinity of $\bar{\boldsymbol{p}}_a$ with standard deviation $\sqrt{3}\,\sigma_a$. Thus, $\bar{\boldsymbol{q}}_a$ and $\bar{\boldsymbol{p}}_a$ are the mean position and the mean momentum of atom a defined as the first moment of $\boldsymbol{q}_a$ and $\boldsymbol{p}_a$, respectively,

$$\langle \, \boldsymbol{q}_a \, \rangle = \bar{\boldsymbol{q}}_a \,, \; \langle \, \boldsymbol{p}_a \, \rangle = \bar{\boldsymbol{p}}_a \,, \;\; \forall \, a = 1, \ldots, N \,. \tag{2.6}$$

Physically, we interpret $\bar{\boldsymbol{q}}_a$ and $\bar{\boldsymbol{p}}_a$ as variables on the continuum scale following the dynamics of the system on the macroscopic time scale. For instance, for a quasistatic process,

$\bar{\boldsymbol{p}} = 0$ and $\bar{\boldsymbol{q}}$ represents an equilibrium configuration of the system. Taking second moments of $\boldsymbol{q}_a$ and $\boldsymbol{p}_a$ introduces the following constraints:

$$\langle |\boldsymbol{q}_a - \bar{\boldsymbol{q}}_a|^2 \rangle = 3\tau_a^2 \,, \ \forall\, a = 1, \ldots, N \,, \tag{2.7a}$$

$$\langle |\boldsymbol{p}_a - \bar{\boldsymbol{p}}_a|^2 \rangle = 3\sigma_a^2 \,, \ \forall\, a = 1, \ldots, N \,. \tag{2.7b}$$

The factor of 3 is included merely to keep the subsequent expressions simple and to motivate the physical interpretation of these parameters. In order to simplify the interpretation further, we replace the parameter τ_a by ω_a defined as

$$\omega_a = \frac{\sigma_a}{\tau_a}, \tag{2.8}$$

and having the unit of frequency. This changes Eq. (2.7a) to

$$\omega_a^2 \, \langle |\boldsymbol{q}_a - \bar{\boldsymbol{q}}_a|^2 \rangle = 3\sigma_a^2 \,, \ \forall\, a = 1, \ldots, N \,. \tag{2.9}$$

σ_a and ω_a are also macroscopic variables. As we shall see in section 2.5, they establish a link between the energetics of the microscopic scale and the thermodynamic quantities. Adding Eq. (2.7b) and Eq. (2.9) yields

$$\langle |\boldsymbol{p}_a - \bar{\boldsymbol{p}}_a|^2 \rangle + \omega_a^2 \, \langle |\boldsymbol{q}_a - \bar{\boldsymbol{q}}_a|^2 \rangle = 6\sigma_a^2 \,, \ \forall\, a = 1, \ldots, N \,. \tag{2.10}$$

Introducing the $N+1$ constraints given by Eq. (2.5) and Eq. (2.10) as Lagrange multipliers

[22], the extremum problem may be stated as

$$\sup_{p} -\frac{k_B}{N!h^{3N}} \int_{\Gamma} p \log p + p\lambda + p \sum_{a=1}^{N} \beta_a \left[|\boldsymbol{p}_a - \bar{\boldsymbol{p}}_a|^2 + \omega_a^2 |\boldsymbol{q}_a - \bar{\boldsymbol{q}}_a|^2 \right] d\boldsymbol{q}\, d\boldsymbol{p}\,, \tag{2.11}$$

where λ corresponds to Eq. (2.5) and the N Lagrange multipliers β_a correspond to Eq. (2.10). Taking the variation of Eq. (2.11) with respect to p and enforcing stationarity yields

$$\int_{\Gamma} \left[\log p + 1 + \lambda + \sum_{a=1}^{N} \beta_a \left(|\boldsymbol{p}_a - \bar{\boldsymbol{p}}_a|^2 + \omega_a^2 |\boldsymbol{q}_a - \bar{\boldsymbol{q}}_a|^2 \right) \right] \delta p\, d\boldsymbol{q}\, d\boldsymbol{p} = 0\,, \tag{2.12}$$

where δp is an admissible variation. The solution of this maximization problem gives the desired probability distribution function

$$p(\boldsymbol{z}|\bar{\boldsymbol{z}}, \{\sigma\}, \{\omega\}) = Z^{-1} \exp\left[-\sum_{a=1}^{N} \beta_a \{ |\boldsymbol{p}_a - \bar{\boldsymbol{p}}_a|^2 + \omega_a^2 |\boldsymbol{q}_a - \bar{\boldsymbol{q}}_a|^2 \} \right], \tag{2.13}$$

where $Z = \exp[1 + \lambda]$ is the partition function of the system. For economy of notation, we have also introduced $\boldsymbol{z} \equiv (\boldsymbol{q}, \boldsymbol{p})$ to denote the microstate and $\bar{\boldsymbol{z}}, \{\sigma\}$ and $\{\omega\}$ to represent the corresponding arrays of macroscopic variables. Thus, $\bar{\boldsymbol{z}} \equiv (\bar{\boldsymbol{q}}, \bar{\boldsymbol{p}})$ and $\{\sigma\}, \{\omega\} \in \mathbb{R}^N$. "|" is used to separate the microscopic and the macroscopic variables. Z may be evaluated by substituting Eq. (2.13) in Eq. (2.5). This yields

$$Z = \frac{1}{N!h^{3N}} \int_{\Gamma} \exp\left[-\sum_{a=1}^{N} \beta_a \{ |\boldsymbol{p}_a - \bar{\boldsymbol{p}}_a|^2 + \omega_a^2 |\boldsymbol{q}_a - \bar{\boldsymbol{q}}_a|^2 \} \right] d\boldsymbol{q}\, d\boldsymbol{p}\,. \tag{2.14}$$

This integral may be evaluated analytically to give

$$Z = \frac{1}{N!h^{3N}} \prod_{a=1}^{N} \left(\sqrt{\frac{\pi}{\beta_a}} \right)^3 \left(\sqrt{\frac{\pi}{\beta_a}} \frac{1}{\omega_a} \right)^3. \tag{2.15}$$

By substituting Eq. (2.13) in either Eq. (2.10) or Eq. (2.7b) and using Eq. (2.15) we obtain the Lagrange multipliers as

$$\beta_a = \frac{1}{2\sigma_a^2}\,. \tag{2.16}$$

The final expressions for the *max-ent* probability distribution and partition function are

$$p(\boldsymbol{z}|\bar{\boldsymbol{z}}, \{\sigma\}, \{\omega\}) = Z^{-1} \exp\left[-\sum_{a=1}^{N} \frac{|\boldsymbol{p}_a - \bar{\boldsymbol{p}}_a|^2 + \omega_a^2 |\boldsymbol{q}_a - \bar{\boldsymbol{q}}_a|^2}{2\sigma_a^2}\right], \tag{2.17a}$$

$$Z = \frac{1}{N! h^{3N}} \prod_{a=1}^{N} \left(\sqrt{2\pi}\sigma_a\right)^3 \left(\sqrt{2\pi}\frac{\sigma_a}{\omega_a}\right)^3 . \tag{2.17b}$$

It may be striking to note that p and Z do not depend on the interaction potential of the system. However, the dependence is implicit in the $\{\omega\}$ which are unspecified so far. We also observe that owing to the local constraints, the global partition function and probability distribution are derived naturally as products of terms associated with each atom. This enables us to write Eq. (2.17a) and Eq. (2.17b) as

$$p(\boldsymbol{z}|\bar{\boldsymbol{z}}, \{\sigma\}, \{\omega\}) = \prod_{a=1}^{N} p_a(\boldsymbol{z}_a \,|\, \bar{\boldsymbol{z}}_a, \sigma_a, \omega_a)\,, \tag{2.18a}$$

$$Z = \prod_{a=1}^{N} Z_a\,. \tag{2.18b}$$

In statistical thermodynamics, this multiplicative form is obtained as a consequence of treating the system as comprising of small systems locally in thermal equilibrium and in weak interaction with each other [41]. In our approach, although the constraint equations are based on both the assumptions, the latter is not enforced on the potential energy when computing phase averages.

Since equations (2.7a) and (2.7b) play a key role in the development of the *max-ent* ap-

proach, they merit further elucidation. First, the *local-equilibrium hypothesis* [19, 45, 8] is implicit in the statement of the constraints and forms a basis of all our later work. It postulates that if a system can be hypothetically split into subsystems, each very close to thermal equilibrium, then the thermodynamic relations hold within each cell. Thus, it assumes the existence of two relaxation times – the relaxation time for the establishment of statistical equilibrium in the whole system and another, much shorter, for establishing equilibrium within a small cell. This enables a rigorous definition of thermodynamic state variables such as temperature and entropy locally. Hence, the local-equilibrium hypothesis forms a fundamental premise of classical non-equilibrium thermodynamics. Likewise, in our approach, it enables us to define phase averages locally and also introduce atomic notions of entropy and temperature.

Second, the constraints distinguish our approach from the canonical ensemble approach of Gibbs in that the latter imposes a constraint on the global energy of the system. For a system in thermal equilibrium, this may be stated as

$$\langle\, H(\boldsymbol{q},\boldsymbol{p})\,\rangle = E\,, \tag{2.19}$$

where H is the Hamiltonian, and E the total internal energy of the system. The resulting probability distribution function has the form

$$p(\boldsymbol{q},\boldsymbol{p}) = Z^{-1}\exp\left[-\frac{H}{k_B T}\right]. \tag{2.20}$$

This form may also be used to derive local thermodynamic quantities by assuming local thermal equilibrium. However, due to the difficulty of integrating this function in the case of anharmonic interaction potentials, the partition function and the thermodynamic po-

tentials may be obtained analytically only for the harmonic approximation. In contrast, the probability distribution function given by (2.17a) involves Gaussian functions. Consequently, the phase averages may be computed analytically for many functions, or at least numerically by Gauss quadrature in order to obtain macroscopic properties.

Finally, we emphasize that our approach of determining a simplified solution for the probability distribution by imposing additional constraints may be regarded as a variational mean field approach. We also note that in this process we have introduced into the problem $2N$ additional unknowns, $\{\sigma\}$ and $\{\omega\}$, referred to as the mean field parameters. For the purpose of computing thermodynamic quantities, it will suffice to accept them as known macroscopic variables. In section 2.3, we shall discuss in detail the variational theory of mean field approximation and seek a way to determine these mean field parameters.

2.2 Thermodynamic potentials

Having constructed a suitable probability distribution, we proceed to obtain the desired thermodynamic potentials, namely, the entropy, the internal energy, and the free energy. In particular, we seek local forms of these potentials and hence appeal to the hypothesis of local thermal equilibrium described earlier.

Entropy

Substituting the probability distribution and the partition function given by Eq. (2.17a) and Eq. (2.17b) in the expression (2.4), the integral for the global entropy evaluates to

$$S = k_B \left[-\log N! + 3N + 3 \sum_{a=1}^{N} \log \frac{\sigma_a^2}{\hbar\, \omega_a} \right] . \tag{2.21}$$

For a system with a very large number of particles, we use Sterling's formula [6]

$$\log N! \approx N \log N - N \tag{2.22}$$

to reduce Eq. (2.21) to

$$S = k_B \left[-N \, \log N + 4N + 3 \sum_{a=1}^{N} \log \frac{\sigma_a^2}{\hbar \, \omega_a} \right] . \tag{2.23}$$

We know that the entropy is an extensive property of the system. That is, if we consider two systems with entropy S_A and S_B, each in thermal equilibrium, then the entropy of the combined system will be $S_A + S_B$. Hence, we can write

$$S \equiv \sum_{a=1}^{N} S_a \, , \tag{2.24}$$

where

$$S_a = 3k_B \, \log \frac{\sigma_a^2}{\hbar \, \omega_a} + 4k_B - k_B \, \log N \tag{2.25}$$

can be interpreted as the contribution of atom a to the total entropy. The relation (2.25) can be inverted to yield

$$\sigma_a = \sqrt{\hbar \, \omega_a} \exp[\frac{S_a}{6k_B} - \frac{4}{6} + \frac{1}{6} \log N] \, . \tag{2.26}$$

Thus, we have an explicit expression for the parameter σ_a, and we use it henceforth to replace σ_a by a function of S_a and ω_a.

Internal energy

In order to derive the internal energy of the system, we suppose that the atoms move according to a Hamiltonian $H(\boldsymbol{z})$. In statistical mechanics, internal energy is defined as the phase average of the Hamiltonian of the system [41]:

$$E(\bar{\boldsymbol{z}}, \{S\}, \{\omega\}) = \langle\, H \,\rangle = \frac{1}{N! h^{3N}} \int_{\Gamma} H(\boldsymbol{z})\, p\,(\boldsymbol{z} \,|\, \bar{\boldsymbol{z}}, \{S\}, \{\omega\})\, d\boldsymbol{q}\, d\boldsymbol{p}\,. \tag{2.27}$$

Suppose that the Hamiltonian has an additive structure

$$H(\boldsymbol{z}) = \sum_{a=1}^{N} H_a(\boldsymbol{z})\,, \tag{2.28}$$

and let $H_a(\boldsymbol{z})$ be of the form

$$H_a(\boldsymbol{z}) = \frac{1}{2}|\boldsymbol{p}_a|^2 + V_a(\boldsymbol{q})\,. \tag{2.29}$$

We emphasize that Eq. (2.28) does not involve any localizing approximation since $V_a(\boldsymbol{q})$ comprises of all the bonds involving the atom a. This is denoted by the dependence of $V_a(\boldsymbol{q})$ on the entire array $\boldsymbol{q} \in X$. Then, Eq. (2.27) becomes

$$E(\bar{\boldsymbol{z}}, \{S\}, \{\omega\}) = \frac{1}{N! h^{3N}} \sum_{a=1}^{N} \int_{\Gamma} \left[\frac{1}{2}|\boldsymbol{p}_a|^2 + V_a(\boldsymbol{q})\right]\, p\,(\boldsymbol{z}|\bar{\boldsymbol{z}}, \{S\}, \{\omega\})\, d\boldsymbol{q}\, d\boldsymbol{p}\,. \tag{2.30}$$

The phase average of the kinetic energy can be computed analytically atom by atom and

reduces to

$$\langle \frac{1}{2}|\boldsymbol{p}_a|^2 \rangle = \int_{-\infty}^{\infty}\int_{-\infty}^{\infty}\int_{-\infty}^{\infty} \frac{1}{2}|\boldsymbol{p}_a|^2 \frac{1}{(\sqrt{2\pi}\sigma_a)^3} \exp(-\frac{|\boldsymbol{p}_a - \bar{\boldsymbol{p}}_a|^2}{2\sigma_a^2}) \prod_{i=1}^{3} dp_{ai} \tag{2.31a}$$

$$= \frac{1}{2}(3\sigma_a^2 + |\bar{\boldsymbol{p}}_a|^2)\,. \tag{2.31b}$$

Unlike kinetic energy, the integration of $V_a(\boldsymbol{q})$ involves all the neighbors of atom a, and in most cases, cannot be computed analytically. Traditionally, the harmonic approximation is used in order to facilitate analytical calculations. However, in our approach, the phase integrals may be computed numerically even for anharmonic potentials by way of Gauss quadrature, and we defer the discussion on the numerical integration of the potential energy till section 2.4. Finally, we summarize that for a system undergoing a quasi-static process, i.e., a process with $\bar{\boldsymbol{p}} = 0$, the internal energy of the system has the form

$$E(\bar{\boldsymbol{q}}, \{S\}, \{\omega\}) = \frac{3}{2}\sum_{a=1}^{N} \hbar\,\omega_a \exp[\frac{S_a}{3k_B} - \frac{4}{3} + \frac{1}{3}\log N] + \sum_{a=1}^{N} \langle\, V_a(\boldsymbol{q})\,\rangle\,, \tag{2.32}$$

where we have made use of Eq. (2.26) to replace σ_a^2.

Equipartition of energy

The equipartition of energy is a fundamental result of statistical mechanics which, loosely speaking, distributes the total energy of the system equally among all the degrees of freedom. More precisely, it states that *for a system in thermal equilibrium, each quadratic term in the Hamiltonian contributes $k_BT/2$ to the mean Hamiltonian or the internal energy of the system, where the phase average is taken with respect to the canonical distribution.* Furthermore, under the assumption of local thermal equilibrium, the equipartition also holds locally. In the present work, we enforce the equipartition of energy through the local

kinetic energy as

$$\langle \frac{1}{2}|\boldsymbol{p}_a|^2 \rangle = \frac{3}{2} k_B T_a \,. \tag{2.33}$$

Comparing this relation with Eq. (2.31b) for a quasistatic process yields a direct interpretation of σ_a in terms of the local temperature:

$$\sigma_a^2 = k_B T_a \tag{2.34}$$

Using this definition of σ_a in Eq. (2.25) gives an equilibrium relation between the local entropy and the local temperature:

$$S_a = 3k_B \, \log \frac{k_B T_a}{\hbar \, \omega_a} + 4k_B - k_B \, \log N \,. \tag{2.35}$$

As we shall see later, although the above expression is local, it is not independent of the atom's surrounding since ω_a contains the effect of the interactions of the atom with its neighbors.

Helmholtz free energy

The Helmholtz free energy is defined as a Legendre transformation of the internal energy with respect to the entropy:

$$F(\bar{\boldsymbol{q}}, \{T\}, \{\omega\}) = \inf_{\{S\}} \left\{ E(\bar{\boldsymbol{q}}, \{S\}, \{\omega\}) - \sum_a T_a S_a \right\} . \tag{2.36}$$

The minimization with respect to S_a yields the equilibrium relation

$$T_a = \frac{\partial E}{\partial S_a}(\bar{\boldsymbol{q}}, \{S\}, \{\omega\}) \,. \tag{2.37}$$

Since the ensemble average of the potential energy $V(\boldsymbol{q})$ can only be computed numerically, Eq. (2.37) cannot be solved to obtain a closed-form relation between T_a and S_a. However, such a relation is furnished by Eq. (2.35). Although due to the aforementioned reason, the equivalence between Eq. (2.37) and Eq. (2.35) cannot be established analytically, we have verified numerically that if we use Eq. (2.35) in our calculations, Eq. (2.37) is satisfied automatically at equilibrium.

Thus, once we have the internal energy, other thermodynamic potentials such as the free energy and the enthalpy may be derived by appropriate Legendre transformations [6, 22]. Then, for a quasistatic process, the problem of finding the equilibrium configurations may be stated as a minimization problem:

$$\inf_{\bar{\boldsymbol{q}}} \Phi \,, \tag{2.38}$$

where Φ is a thermodynamic potential appropriate for the process. For instance, the Helmholtz free energy is a suitable energy functional for isothermal conditions. However, the problem still involves the unspecified parameters, $\{\omega\}$. As will be elucidated in the next section, these parameters are also determined by minimizing the free energy.

As a concluding remark, we note that for a dynamic process, i.e., with $\bar{\boldsymbol{p}} \neq 0$, the minimization problem may be replaced by the canonical equations derived from the macroscopic Hamiltonian:

$$\dot{\bar{\boldsymbol{q}}} = \frac{\partial \bar{H}}{\partial \bar{\boldsymbol{p}}}; \;\; \dot{\bar{\boldsymbol{p}}} = -\frac{\partial \bar{H}}{\partial \bar{\boldsymbol{q}}} \,, \tag{2.39}$$

where $\bar{H} = \langle\, H \,\rangle$. However, we shall not pursue this direction in our current work and shall restrict ourselves to quasistatic processes.

2.3 Variational mean field theory

Mean field theory was developed essentially as an approximation tool for facilitating a theoretical treatment of critical phenomena such as phase transitions ([6], [5]). The basic idea is to study one particle in the system and treat its interactions with the neighboring particles as an average molecular field exerted by the atom's environment. This significantly reduces the degrees of freedom in the problem. In order to understand our *max-ent* approach as a mean field approximation, we briefly review the variational framework for deriving generalized mean field theories. The variational method is implemented as follows: First a simplified functional form with free unspecified parameters is chosen as the trial probability distribution function. We denote it by p. We also let the approximate free energy obtained using this trial function be F_p. Since the effect of the ambience of a particle is approximated as a "mean field", the trial probability distribution is obtained as a product of local probability distribution functions

$$p = \prod_{a=1}^{N} p_a \,. \tag{2.40}$$

As described in section 2.1, the trial functional form may be derived by maximizing the global entropy subject to certain constraints. Then, the trial probability distribution function that best approximates the actual probability distribution function is determined by minimizing the approximate free energy, F_p, with respect to the unspecified parameters in p. The last claim is based on a result known as the *Bogoliubov's inequality*, which states that the approximate free energy based on any probability distribution provides an upper bound for the actual free energy of the system [5]. That is,

$$F \leq F_p \tag{2.41}$$

for any p satisfying the basic properties of a probability distribution. An outline of the proof is as follows. For convenience we use the following notation:

$$\langle \cdot \rangle = \int (\cdot)\, d\boldsymbol{q}\, d\boldsymbol{q}\,, \tag{2.42a}$$

$$\langle \cdot \rangle_p = \int (\cdot)\, p\, d\boldsymbol{q}\, d\boldsymbol{q}\,, \tag{2.42b}$$

and neglect the factor of $(N!\, h^{3N})^{-1}$ since it is simply carried over through the calculations. We begin by reviewing the proof of the following inequality for any random variable.

Claim 2.3.1. *For any random variable ϕ and an associated probability distribution p,*

$$\langle e^{-\lambda\phi} \rangle_p \geq e^{-\lambda \langle \phi \rangle_p}\,, \tag{2.43}$$

where $\lambda \in \mathbb{R}$ is any constant.

Proof. Due to the convexity of the exponential function, the inequality

$$e^{\phi} \geq 1 + \phi \tag{2.44}$$

is valid for any $\phi \in \mathbb{R}$. Thus, applying this inequality we have

$$e^{-\lambda\phi} = e^{-\lambda\langle\phi\rangle_p}\, e^{-\lambda(\phi - \langle\phi\rangle_p)} \geq e^{-\lambda\langle\phi\rangle_p}[1 - \lambda(\phi - \langle\phi\rangle_p)]\,. \tag{2.45}$$

Taking the phase average of both sides of the above inequality yields

$$\langle e^{-\lambda\phi} \rangle_p \geq \langle e^{-\lambda\langle\phi\rangle_p}[1 - \lambda(\phi - \langle\phi\rangle_p)] \rangle = e^{-\lambda\langle\phi\rangle_p}\,, \tag{2.46}$$

□

which proves the inequality (2.43). In statistical thermodynamics, for a system in thermal equilibrium at temperature T, the actual Helmholtz free energy of a system is defined by the relation

$$e^{-\beta F} = \langle\, e^{-\beta H} \,\rangle\,, \tag{2.47}$$

where

$$\beta = \frac{1}{k_B T}\,,$$

and $H(\boldsymbol{z})$ is the Hamiltonian of the system. As an aside, we mention that the right hand side of Eq. (2.47) is the partition function for the Gibb's canonical distribution described by Eq. (2.20). However, in the present work, the right hand side does not identify with the partition function, as is evident by comparing Eq. (2.47) and Eq. (2.17b). In thermodynamics, the Helmholtz free energy is also defined by the following Legendre transformation

$$F = E - TS \tag{2.48}$$

with

$$T = \frac{\partial E}{\partial S}\,. \tag{2.49}$$

By substituting the definitions for the entropy and the internal energy given by Eq. (2.4) and Eq. (2.27), respectively, Eq. (2.48) can be written as

$$F_p = \langle\, H \,\rangle_p + k_B T \,\langle \log p \,\rangle_p \tag{2.50a}$$

$$= \langle\, H + \frac{1}{\beta} \log p \,\rangle_p \tag{2.50b}$$

where F_p is an approximation to the free energy based on the probability density p. Taking exponential of both sides of Eq. (2.50b) and using the inequality (2.43) shows that

$$e^{-\beta F_p} = e^{-\beta\langle H + \frac{1}{\beta}\log p\rangle_p} \tag{2.51a}$$

$$\leq \langle e^{-\beta H - \log p}\rangle_p = \langle e^{-\beta H}\frac{1}{p}p\rangle = \langle e^{-\beta H}\rangle\,. \tag{2.51b}$$

Equations (2.47) and (2.51b) together lead to the Bogoliubov's inequality (2.41). Consequently, the minimization of F_p with respect to the free parameters in p gives the best approximation for the free energy.

To summarize, we have used the variational structure of the mean field theory in order to derive approximate probability distribution functions. The optimal value of the free parameters that we introduced for this purpose can now be determined by minimizing the free energy. We recall that $\{\sigma\}$ can be eliminated by using expression (2.26) or (2.34). Thus, the complete problem of ascertaining the equilibrium configurations of a system undergoing a quasistatic process may be enunciated as

$$\inf_{\bar{\boldsymbol{q}}}\ \inf_{\{\omega\}}\ F\left(\bar{\boldsymbol{q}}, \{T\}, \{\omega\}\right), \tag{2.52}$$

F being the Helmholtz free energy of the system evaluated by the *max-ent* approximation.

2.4 Phase averages by Gauss quadrature

Sections 2.1 and 2.2 describe the procedure for arriving at temperature-dependent potentials as phase averages based on the local *max-ent* approximation scheme. We recall that the average of the kinetic energy can be computed analytically, thereby reducing internal energy

to a function of the state variables as given in Eq. (2.32):

$$E\,(\bar{\boldsymbol{q}},\{S\},\{\omega\}) = \frac{3}{2}\sum_{a=1}^{N}\hbar\,\omega_a\,\exp[\frac{S_a}{3k_B}-\frac{4}{3}+\frac{1}{3}\log N]+\sum_{a=1}^{N}\langle\, V_a(\boldsymbol{q})\,\rangle\,. \tag{2.53}$$

We now wish to evaluate the phase average of the potential energy $V(\boldsymbol{q})$. To this end, we suppose that each function $V_a(\boldsymbol{q})$ involves a small number of neighboring atoms. Then, the integrals in $\langle\, V_a(\boldsymbol{q})\,\rangle$ are likewise of small dimensionality and can effectively be computed by means of Gaussian quadrature, i.e., with integration points and weights corresponding to a Gaussian weight function. This is due to the specific form of the *max-ent* probability densities. We begin by considering an n-body interaction potential, $\phi(\boldsymbol{q}_1,\ldots,\boldsymbol{q}_n)$. The expectation value of this function is computed as

$$\langle\phi(\boldsymbol{q}_1,\ldots,\boldsymbol{q}_n)\rangle = \frac{1}{N!h^{3N}}\int_\Gamma \phi(\boldsymbol{q}_1,\ldots,\boldsymbol{q}_n)\prod_{a=1}^{n} p_a\,d\boldsymbol{p}_a\,d\boldsymbol{q}_a \tag{2.54a}$$

$$= \prod_{a=1}^{n}\frac{1}{(\sqrt{2\pi}\sigma_a/\omega_a)^3}\int \phi(\boldsymbol{q}_1,\ldots,\boldsymbol{q}_n)\prod_{a=1}^{n}\exp(-\frac{\omega_a^2}{2\sigma_a^2}|\boldsymbol{q}_a-\bar{\boldsymbol{q}}_a|^2)\,d\boldsymbol{q}_a \tag{2.54b}$$

$$= \left(\frac{1}{\sqrt{\pi}}\right)^{3n}\int_{-\infty}^{\infty}\cdots\int_{-\infty}^{\infty}\tilde{\phi}(\boldsymbol{x}_1,\ldots,\boldsymbol{x}_n)\exp(-|\boldsymbol{x}_1|^2-\cdots-|\boldsymbol{x}_n|^2)\,d\boldsymbol{x}_1\cdots d\boldsymbol{x}_n\,, \tag{2.54c}$$

where

$$\tilde{\phi}(\boldsymbol{x}_1,\ldots,\boldsymbol{x}_n) = \phi(\boldsymbol{q}_1(\boldsymbol{x}_1),\ldots,\boldsymbol{q}_n(\boldsymbol{x}_n))\,.$$

Eq. (2.54c) is the result of a change of variables:

$$\boldsymbol{x}_a = \frac{1}{\sqrt{2}}\frac{\omega_a}{\sigma_a}(\boldsymbol{q}_a-\bar{\boldsymbol{q}}_a)\,. \tag{2.55}$$

The multiple integral in Eq. (2.54c) is of dimension $3n$ and may be computed by using the Hermite-Gauss quadrature rule appropriate for the dimension of the space [36, 13]. An M-point quadrature reduces the integral to

$$\langle \phi(\boldsymbol{q}_1, \ldots, \boldsymbol{q}_n) \rangle \approx \left(\frac{1}{\sqrt{\pi}} \right)^{3n} \sum_{k=1}^{M} \tilde{\phi}(\xi_k) W_k \,, \tag{2.56}$$

where k denotes a quadrature point in phase space, W_k is the corresponding weight and ξ is a vector of dimension $3n$:

$$\xi = (\boldsymbol{x}_1, \ldots, \boldsymbol{x}_n) \in \mathbb{R}^{3n} \,. \tag{2.57}$$

In our calculations, we use quadrature rules for multiple integrals developed in the work of Stroud [36]. A limiting factor in the choice of quadrature formulae is the dimension of the domain of integration. For a pair potential, we have the choice of using quadrature rules of degrees 3 and 5. For many-body potentials, we are restricted to 3^{rd} degree quadrature due to the high dimension of the space of integration. The details of the quadrature rules that we have used in this work are provided in Appendix B.

Thus, the *max-ent* distribution provides a way to compute an approximate internal energy of the system, which should be exact for up to 3^{rd} or 5^{th} order Taylor expansion of the potential energy about an equilibrium configuration. This implies a considerable improvement over the quasi-harmonic approximation used typically in obtaining thermodynamic quantities from the microscopic dynamics. An important implication of this higher order approximation is the ability to account for the anharmonicity of the interaction potential, although approximately, in studying the thermodynamic behavior of materials.

In the remaining part of the section, we demonstrate the above calculations for two empirical interatomic potentials, namely the Lennard-Jones pair potential and the embedded atom

method involving many-body interactions. Since our ultimate aim is the minimization of free energy, we also provide the expressions for the derivatives of the energy with respect to the atomic positions and the mean field variables, $\{\omega\}$. We also remark that these are mere examples to illustrate the generality of applying the *max-ent* distribution to any empirical interatomic potential and crystal structure.

2.4.1 Lennard-Jones potential

The phase average of the potential energy based on the Lennard-Jones pair potential is of the form

$$\langle V \rangle = \frac{1}{2} \sum_a \sum_b \langle \phi(r_{ab}) \rangle \,, \tag{2.58}$$

where

$$\phi(r) = 4\epsilon \left[(\frac{\sigma}{r})^{12} - 2(\frac{\sigma}{r})^6 \right] \tag{2.59}$$

represents the bond energy and r_{ab} denotes the distance between atoms a and b. Typically, b denotes the nearest neighbors of atom a. Since the potential involves only pairwise interactions, the phase averages can be computed over individual bonds involving two atoms. Consequently, the dimension of the domain of integration is 6. Applying the change of variables given in Eq. (2.55), we have

$$r_{ab} = |\boldsymbol{q}_a - \boldsymbol{q}_b| \tag{2.60a}$$

$$= |\sqrt{2}\frac{\sigma_a}{\omega_a}\boldsymbol{x}_a - \sqrt{2}\frac{\sigma_b}{\omega_b}\boldsymbol{x}_b + \bar{\boldsymbol{q}}_a - \bar{\boldsymbol{q}}_b| \,. \tag{2.60b}$$

Then, the energy of each bond calculated by quadrature is

$$\langle \phi(r_{ab}) \rangle \approx \left(\frac{1}{\sqrt{\pi}} \right)^6 \sum_{k=1}^{M} \phi(\tilde{\xi}_k) W_k \,. \tag{2.61}$$

As described in Appendix B, the 3$^{\text{rd}}$ degree quadrature formula requires 12 quadrature points while the 5$^{\text{th}}$ degree formula requires 44 quadrature points. Taking the derivative of the energy with respect to the atomic positions yields

$$\frac{\partial}{\partial \bar{\boldsymbol{q}}_a} \langle V \rangle = \sum_b \frac{\partial}{\partial \bar{\boldsymbol{q}}_a} \langle \phi(r_{ab}) \rangle \tag{2.62a}$$

$$= \left(\frac{1}{\sqrt{\pi}} \right)^6 \sum_b \sum_{k=1}^{M} \phi'(r_{ab}(\xi_k)) \frac{\boldsymbol{r}_{ab}}{r_{ab}} W_k \,, \tag{2.62b}$$

where prime denotes differentiation with respect to r. Taking the derivative of the internal energy with respect to ω_a yields

$$\frac{\partial}{\partial \omega_a} \langle V \rangle = \sum_b \frac{\partial}{\partial \omega_a} \langle \phi(r_{ab}) \rangle \tag{2.63a}$$

$$= -\frac{1}{\sqrt{2}} \left(\frac{1}{\sqrt{\pi}} \right)^6 \sum_b \sum_{k=1}^{M} \frac{\sigma_a}{\omega_a^2} \frac{\phi'(r_{ab}(\xi_k))}{r_{ab}} \left[\boldsymbol{r}_{ab} \cdot \boldsymbol{x}_a^k \right] W_k \tag{2.63b}$$

and

$$\frac{\partial}{\partial \omega_a} \langle \frac{1}{2} |\boldsymbol{p}_a|^2 \rangle = \frac{3}{2} \hbar \exp[\frac{S_a}{3k_B} - \frac{4}{3} + \frac{1}{3} \log N] \,, \tag{2.64}$$

where Eq. (2.63b) gives the contribution of the potential energy, whereas Eq. (2.64) gives that of the kinetic energy.

2.4.2 EAM potential

The potential energy based on the embedded-atom method [7, 18] is of the form

$$V = \sum_a F(\rho_a) + \frac{1}{2}\sum_a \sum_b \phi(r_{ab})\,. \tag{2.65}$$

In addition to a pair potential, we now have a term $F(\rho_a)$ for each atom, which is known as the embedding function and which depends on the electron density at site a due to all its neighbors. In our calculations, we use two analytical forms for the EAM potential, one proposed by Johnson [18] and another proposed by Sutton and Chen [37]. They are described in Appendix A.2. Although the functional form of the pair potential is different, the expressions for its phase average and its derivatives are identical to those shown for the Lennard-Jones potential. The expressions for the embedding term are calculated below. Let us define

$$V_2 = \sum_{a=1}^{N} F(\rho_a)\,. \tag{2.66}$$

Then,

$$\langle V_2 \rangle = \sum_a \langle\, F(\rho_a)\,\rangle = \left(\frac{1}{\sqrt{\pi}}\right)^{3n} \sum_{k=1}^{M} F\left(\rho_a(\xi_k)\right) W_k\,, \tag{2.67}$$

where n includes the atom a and its contributing neighbors. For an fcc crystal with nearest-neighbor interactions, $n = 13$ for an atom having all its neighbors. The derivative of $\langle V_2 \rangle$ with respect to the atomic positions is of the form

$$\begin{aligned}\frac{\partial}{\partial \bar{\boldsymbol{q}}_a}\langle V_2\rangle = &\left(\frac{1}{\sqrt{\pi}}\right)^{3n_a} \sum_b \sum_{k=1}^{M_a} F'(\rho_a(\xi_k)) f'(r_{ab}(\xi_k))\,\frac{\boldsymbol{r}_{ab}}{r_{ab}}\,W_k \\ &+ \left(\frac{1}{\sqrt{\pi}}\right)^{3n_b} \sum_b \sum_{l=1}^{M_b} F'(\rho_b(\xi_l)) f'(r_{ab}(\xi_l))\,\frac{\boldsymbol{r}_{ab}}{r_{ab}}\,W_l\,,\end{aligned} \tag{2.68}$$

where

$$F' = \frac{d}{d\,\rho}\ ,\quad f' = \frac{d}{d\,r}\,.$$

Similarly, the derivative of $\langle V_2 \rangle$ with respect to the local mean field parameters is

$$\begin{aligned}\frac{\partial}{\partial \omega_a}\langle V_2\rangle = &-\frac{1}{\sqrt{2}}\left(\frac{1}{\sqrt{\pi}}\right)^{3n_a}\frac{\sigma_a}{\omega_a^2}\sum_b\sum_{k=1}^{M_a}F'(\rho_a(\xi_k))\,f'(r_{ab}(\xi_k))\,[\boldsymbol{r}_{ab}\cdot\boldsymbol{x}_a^k]\,W_k \\ &-\frac{1}{\sqrt{2}}\left(\frac{1}{\sqrt{\pi}}\right)^{3n_b}\frac{\sigma_a}{\omega_a^2}\sum_b\sum_{l=1}^{M_b}F'(\rho_b(\xi_l))\,f'(r_{ab}(\xi_l))\,[\boldsymbol{r}_{ab}\cdot\boldsymbol{x}_a^l]\,W_l\,.\end{aligned} \tag{2.69}$$

In Eq. (2.68) and Eq. (2.69), n_a is the total number of atoms in the neighborhood of atom a, and M_a is the number of quadrature points used to compute the phase average $\langle F(\rho_a)\rangle$. Using the 3$^{\text{rd}}$ degree quadrature formula for an atom in an fcc crystal with all its nearest neighbors present requires 78 quadrature points.

It bears emphasis that although ω is introduced as a local parameter associated with each atom, Eq. (2.63b) and Eq. (2.69) show that the minimization of the free energy with respect to ω_a cannot be achieved atom by atom. This reveals the non-local nature of $\{\omega\}$, indicating that it is related to the atomic interactions.

2.5 Analysis of the *max-ent* method

In this section, we present some analytical results that afford some insight into the *max-ent* approach and its connection with the canonical distribution of statistical mechanics. In particular, the first validation test that we demonstrate is the derivation of the ideal gas law using the *max-ent* distribution. Next, we seek a physical interpretation of the mean field parameters, $\{\omega\}$. This is achieved by using a quasi-harmonic approximation for the potential energy in order to compute the thermodynamic potentials for the system

analytically and to determine the $\{\omega\}$. Finally, we review the thermodynamic potentials determined from the canonical ensemble approach and compare with those obtained with the *max-ent* approach, thereby establishing a connection between the two methods, at least under certain conditions.

2.5.1 The ideal gas law

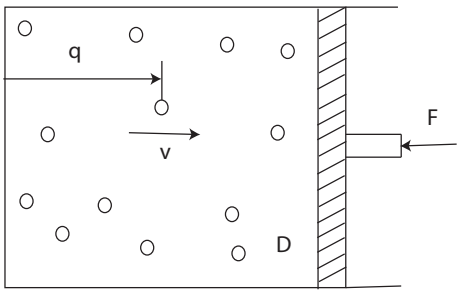

Figure 2.1: Ideal gas enclosed in a container with a piston.

We consider a system of N identical monatomic molecules of an ideal gas in a container of volume V as shown in Figure 2.1. Let $p(\boldsymbol{q}, \boldsymbol{p})$ be the probability distribution function for the system. Since the particles are non-interacting, the only constraint on the positions of the particles is that

$$\boldsymbol{q} \in \mathrm{D}\,,$$

where D is the region enclosed by the container. That is, the probability of finding a particle inside the container is 1 and zero outside. Consequently,

$$\tau_a = 0,\ \forall\, a\,. \tag{2.70}$$

As before, the probability distribution function is determined by maximizing the entropy

$$S = -\frac{k_B}{N!h^{3N}} \int_\Gamma p \log p \, d\boldsymbol{q} \, d\boldsymbol{p} \,, \tag{2.71}$$

subject to the normalization constraint (2.5) and the constraint on the momenta

$$\langle |\boldsymbol{p}_a - \bar{\boldsymbol{p}}_a|^2 \rangle = 3\sigma_a^2 \quad \forall \, a = 1, \ldots, N \,. \tag{2.72}$$

We consider the system to be in thermal equilibrium at a uniform temperature T and with $\bar{\boldsymbol{q}} = 0$. Consequently, we can assume

$$\sigma_a = \sigma \quad \forall \, a \,. \tag{2.73}$$

This gives the partition function and the probability distribution as

$$Z = \frac{k_B}{N!h^{3N}} (\sqrt{2\pi}\sigma)^{3N} V^N \tag{2.74a}$$

$$p = Z^{-1} \exp\left[-\frac{1}{2\sigma^2} \sum_{a=1}^{N} |\boldsymbol{p}_a|^2 \right] \tag{2.74b}$$

since

$$\int_{\mathrm{D}} \prod_{a=1}^{N} d\boldsymbol{q}_a = V^N \,.$$

Using Eq. (2.74a) and Eq. (2.74b) in Eq. (2.71), the entropy of the system becomes

$$\begin{aligned} S &= k_B \log Z + \frac{3}{2} N \\ &= -k_B \log(N! h^{3N}) + 3N k_B \log(\sqrt{2\pi}\sigma) + N k_B \log V + \frac{3}{2} N \,. \end{aligned} \tag{2.75a}$$

The Hamiltonian of an ideal gas with N particles is

$$H(\boldsymbol{p}) = \frac{1}{2}\sum_{i=1}^{N} |\boldsymbol{p}_a|^2 \,. \tag{2.76}$$

Then, the internal energy of the system is

$$E = \langle\, H \,\rangle = \frac{3}{2} N\sigma^2 \,. \tag{2.77}$$

As we saw in section 2.2, enforcing the equipartition of energy yields

$$\sigma = \sqrt{k_B T} \,. \tag{2.78}$$

Substituting the above in Eq. (2.77) yields the internal energy for an ideal gas as desired:

$$E = \frac{3}{2} N k_B T \,. \tag{2.79}$$

Next, the free energy of the system may be computed as

$$\begin{aligned} F &= E - TS \\ &= -k_B T \log(N! h^{3N}) - \frac{3}{2} N k_B T \log(2\pi k_B T) - N k_B T \log V \,, \end{aligned} \tag{2.80a}$$

where we have used Eq. (2.79), Eq. (2.75a), and Eq. (2.78). Then, the pressure p of the gas is defined as

$$p = -\frac{\partial F}{\partial V} = N k_B T \frac{1}{V} \,, \tag{2.81}$$

which yields the ideal gas law

$$pV = Nk_BT\,. \tag{2.82}$$

This shows that the equation of state for an ideal gas can also be derived from the *max-ent* mean field approximation.

2.5.2 Interpretation of the mean field parameters

In this section we investigate the connection between our approach and statistical mechanics in order to obtain an interpretation of the mean field parameters. We have already observed in section 2.2 that σ_a is equivalent to k_BT_a. Through the calculations that follow, we conclude that ω_a for an atom is indeed an approximate average of the local frequencies associated with that atom. In order to make analytical calculations feasible, we begin by considering a quasi-harmonic approximation for the potential energy of the system. This is obtained as a second-order Taylor expansion of $V(\boldsymbol{q})$ about an equilibrium configuration:

$$V(\boldsymbol{q}) \approx V(\bar{\boldsymbol{q}}) + \frac{1}{2}\boldsymbol{x}^{\mathrm{T}}\,\mathrm{K}(\bar{\boldsymbol{q}})\,\boldsymbol{x}\,, \tag{2.83}$$

where $\mathrm{K}(\bar{\boldsymbol{q}}) \in \mathbb{R}^{3N} \times \mathbb{R}^{3N}$ is the stiffness matrix of the system given by

$$\mathrm{K}(\bar{\boldsymbol{q}}) = \left.\frac{\partial^2 V}{\partial \boldsymbol{q}^2}\right|_{\boldsymbol{q}=\bar{\boldsymbol{q}}} \tag{2.84}$$

and

$$\boldsymbol{x} = \{\boldsymbol{x}_1, \ldots, \boldsymbol{x}_N\} \text{ with } \boldsymbol{x}_a = \boldsymbol{q}_a - \bar{\boldsymbol{q}}_a\,.$$

By further assuming weak interactions between the atoms, we reduce Eq. (2.83) to

$$V(\boldsymbol{q}) \approx V(\bar{\boldsymbol{q}}) + \sum_a \frac{1}{2} \boldsymbol{x}_a^{\mathrm{T}} \mathrm{K}_a(\bar{\boldsymbol{q}}) \boldsymbol{x}_a = \sum_a V_a(\boldsymbol{q}) \,, \tag{2.85}$$

where K_a is the 3×3 local dynamical matrix associated with each atom and defined as

$$\mathrm{K}_a(\bar{\boldsymbol{q}}) = \left. \frac{\partial^2 V}{\partial \boldsymbol{q}_a^2} \right|_{\boldsymbol{q}_a = \bar{\boldsymbol{q}}_a} . \tag{2.86}$$

This is known as the *local* quasi-harmonic approximation since it regards each atom as a harmonic oscillator with all its neighbors fixed and, hence, neglects the off-diagonal terms of $\mathrm{K}(\bar{\boldsymbol{q}})$. We note that the coupling of an atom with its neighborhood is retained through the dependence of the local dynamical matrix on the macroscopic variables $\bar{\boldsymbol{q}}$. Then, the phase average of the potential energy may be computed analytically as

$$\langle V_a \rangle = \frac{1}{(\sqrt{2\pi}\sigma_a/\omega_a)^3} \int \left[V_a(\bar{\boldsymbol{q}}) + \frac{1}{2} \boldsymbol{x}_a^{\mathrm{T}} \, \mathrm{K}_a(\bar{\boldsymbol{q}}) \, \boldsymbol{x}_a \right] \exp\left[-\frac{\omega_a^2}{2\sigma_a^2} |\boldsymbol{x}_a|^2 \right] \, d\boldsymbol{x}_a \tag{2.87a}$$

$$= V_a(\bar{\boldsymbol{q}}) + \frac{1}{2} \frac{1}{(\sqrt{2\pi}\sigma_a/\omega_a)^3} \int [\mathrm{K}_{11}^a \, x_{a1}^2 + \mathrm{K}_{22}^a \, x_{a2}^2 + \mathrm{K}_{33}^a \, x_{a3}^2] \prod_{i=1}^{3} \exp\left[-\frac{\omega_a^2}{2\sigma_a^2} x_{ai}^2 \right] \, dx_{ai} \tag{2.87b}$$

$$= V_a(\bar{\boldsymbol{q}}) + \frac{1}{2} \frac{\sigma_a^2}{\omega_a^2} \operatorname{Tr} \mathrm{K}_a(\bar{\boldsymbol{q}}) \,. \tag{2.87c}$$

On substituting the above in Eq. (2.32) the internal energy of the system becomes

$$E(\bar{\boldsymbol{q}}, \{S\}, \{\omega\}) = \sum_a V_a(\bar{\boldsymbol{q}}) + \sum_a \frac{1}{2} \left[3 + \frac{1}{\omega_a^2} \operatorname{Tr} \mathrm{K}_a(\bar{\boldsymbol{q}}) \right] \frac{h\omega_a}{2\pi} \exp[\frac{S_a}{3k_B} - \frac{4}{3} + \frac{1}{3} \log N] \,, \tag{2.88}$$

where Tr denotes the trace of the matrix. The partial derivative of the internal energy with respect to the local entropy yields the equilibrium relation

$$\begin{aligned} T_a &= \frac{\partial E}{\partial S_a} \\ &= \frac{1}{6k_B}\left[3 + \frac{1}{\omega_a^2}\mathrm{Tr}\mathbf{K}_a(\bar{\boldsymbol{q}})\right]\frac{h\omega_a}{2\pi}\exp[\frac{S_a}{3k_B} - \frac{4}{3} + \frac{1}{3}\log N]\,. \end{aligned} \tag{2.89a}$$

We invert the above relation to obtain S_a in terms of T_a. Substituting it in Eq. (2.88) gives the internal energy as a function of the local temperatures:

$$E(\bar{\boldsymbol{q}}, \{T\}, \{\omega\}) = V(\bar{\boldsymbol{q}}) + \sum_a 3k_B T_a\,, \tag{2.90}$$

which is a well known result from statistical mechanics in agreement with the equipartition of energy. By substituting these expressions for the internal energy and the entropy as functions of the temperature in Eq. (2.36), the free energy becomes

$$F(\bar{\boldsymbol{q}}, \{T\}, \{\omega\}) = V(\bar{\boldsymbol{q}}) - 3k_B\sum_a T_a\left[\log\frac{6k_BT_a}{\hbar} - \log\left\{\left[3 + \frac{1}{\omega_a^2}\mathrm{TrK}_a(\bar{\boldsymbol{q}})\right]\omega_a\right\} + \frac{4}{3} - \frac{1}{3}\log N\right]\,. \tag{2.91}$$

Minimizing F with respect to ω_a gives

$$\omega_a^2 = \frac{1}{3}\mathrm{TrK}_a = \frac{1}{3}\sum_{i=1}^{3}\bar{\omega}_{ia}^2(\bar{\boldsymbol{q}})\,, \tag{2.92}$$

where $\bar{\omega}_{ia}$ denotes the three frequencies associated with the atom a. This implies that for a quasi-harmonic approximation, ω_a^2 equals the arithmetic mean of the squares of the quasi-harmonic frequencies associated with that atom. Furthermore, substituting this in

Eq. (2.89a) verifies that at equilibrium

$$\sigma_a^2 = k_B T_a \,, \tag{2.93}$$

as derived in section 2.2. Thus, we conclude that for a system with a general anharmonic potential energy, ω_a provides an approximate average of the local frequencies of the atom a. This is an important result since it reveals the physical nature of the parameters ω_a and confirms that the $\{\omega\}$ and $\{\sigma\}$ establish the link between the energetics of the microscopic dynamics and their cumulative effect on the thermodynamic potential.

2.5.3 Comparison with Gibbs canonical distribution

Here, we present a comparison between the thermodynamic potentials furnished by the *max-ent* approach and those obtained by using the Gibbs canonical ensemble. To this end, we first use the calculations presented in the previous section to summarize the expressions for the thermodynamic potentials for a system under thermal equilibrium at uniform temperature T. For such a system, the *max-ent* partition function and probability distribution are

$$Z = \frac{1}{N!}\left(\frac{1}{\beta}\right)^{3N} \prod_{a=1}^{N} \omega_a^{-3} \tag{2.94a}$$

$$\rho = Z^{-1} \exp\left[-\beta \frac{1}{2} \sum_a \left\{ |\boldsymbol{p}_a - \bar{\boldsymbol{p}}_a|^2 + \omega_a^2 |\boldsymbol{q}_a - \bar{\boldsymbol{q}}_a|^2 \right\}\right] , \tag{2.94b}$$

where $\beta = \sigma_a^{-2} = (k_B T)^{-1}$. Using Eq. (2.92) and Eq. (2.93), the entropy, the internal energy, and the Helmholtz free energy have the following forms

$$E = \sum_a V_a(\bar{\boldsymbol{q}}) + 3Nk_BT \tag{2.95a}$$

$$F = \sum_a V_a(\bar{\boldsymbol{q}}) + k_BT \log N!(h)^{3N} - 3Nk_BT \log 2\pi k_BT + \frac{3}{2}k_BT \sum_a \log \left[\frac{1}{3}\sum_{i=1}^{3} \bar{\omega}_{ia}^2\right] \tag{2.95b}$$

$$S = 3Nk_B - k_B \log N!(h)^{3N} + 3Nk_B \log 2\pi k_BT - \frac{3}{2}k_B \sum_a \log \left[\frac{1}{3}\sum_{i=1}^{3} \bar{\omega}_{ia}^2\right], \tag{2.95c}$$

where we have assumed $\bar{\boldsymbol{p}} = 0$. We now review the calculations of these thermodynamic quantities based on the canonical ensemble approach of Gibbs. We recall that the partition function and the probability distribution for a system under uniform thermal equilibrium are

$$Z = \langle e^{\beta H} \rangle \tag{2.96a}$$

$$p = Z^{-1} e^{\beta H}, \tag{2.96b}$$

where H is the Hamiltonian

$$H = \frac{1}{2}|\boldsymbol{p}|^2 + V(\boldsymbol{q}). \tag{2.97}$$

As remarked earlier, the ensemble averages using the canonical distribution can be computed analytically only in the case of a quasi-harmonic approximation for the potential energy. The resulting expressions involve the computation of the $3N$ frequencies of the system. Although these results are amiable to theoretical analysis, their numerical implementation poses a severe computational challenge as the size of the system increases. This problem is

invariably circumvented by invoking the *local* quasi-harmonic approximation. Hence, using Eq. (2.85), the expressions for the internal energy, entropy, and free energy are obtained as [41]:

$$E = V(\bar{\boldsymbol{q}}) + 3Nk_BT \tag{2.98a}$$

$$F = V(\bar{\boldsymbol{q}}) + k_BT \log N!(h)^{3N} - 3Nk_BT \log 2\pi k_BT + k_BT \sum_a \log \left[\prod_{i=1}^{3} \bar{\omega}_{ia} \right] \tag{2.98b}$$

$$S = 3Nk_B - k_B \log N!(h)^{3N} + 3Nk_B \log 2\pi k_BT - k_B \sum_a \log \left[\prod_{i=1}^{3} \bar{\omega}_{ia} \right] . \tag{2.98c}$$

On comparing the results furnished by both the methods, we note that the internal energy is identical in both the cases, as it follows directly from the equipartition of energy. The entropy and the free energy are also identical except for the terms involving the frequencies. Specifically, Eq. (2.95b) and Eq. (2.95c), derived from the *max-ent* distribution, involve the trace of the local stiffness matrices, whereas Eq. (2.98b) and Eq. (2.98c), derived from the canonical distribution, involve the determinant of the local stiffness matrices. Nevertheless, under certain conditions the equivalence of the two methods may be established, as shown by the following propositions.

Proposition 2.5.1. *For an infinite perfect and isotropic crystal, subject to uniform temperature,*

$$F_{max-ent} = F_{Gibbs} \tag{2.99}$$

$$S_{max-ent} = S_{Gibbs} \tag{2.100}$$

Proof. Consider an infinite perfect crystal subject to a homogeneous deformation such as thermal expansion under uniform temperature. The local quasi-harmonic approximation assumes each atom as a harmonic oscillator with all neighbors fixed at their current mean

positions. Hence, assuming the crystal to be isotropic, the frequencies of each atom should be equal. That is,

$$\bar{\omega}_{1a} = \bar{\omega}_{2a} = \bar{\omega}_{3a} = \bar{\omega}_a, \ \ \forall \ a \, . \tag{2.101}$$

Consequently,

$$\frac{3}{2} \log \left[\frac{1}{3} \sum_{i=1}^{3} \bar{\omega}_{ia}^2 \right] = 3 \log \bar{\omega}_a = \log \bar{\omega}_a^3 = \log \left[\prod_{i=1}^{3} \bar{\omega}_{ia} \right] . \tag{2.102}$$

By substituting the above simplification in Eq. (2.95b) and Eq. (2.95c), they, respectively, become identical to Eq. (2.98b) and Eq. (2.98c). This proves the equivalence of the free energy and the entropy obtained from the *max-ent* distribution and the canonical distribution. □

Under less stringent conditions on the crystal, one may also prove the following convergence between the two methods.

Proposition 2.5.2. *Consider an infinite perfect crystal subject to uniform temperature. Applying the Mie-Grüneisen approximation locally,*

$$\left(\frac{\partial F}{\partial \boldsymbol{q}_a} \right)_{max-ent} = \left(\frac{\partial F}{\partial \boldsymbol{q}_a} \right)_{Gibbs} \tag{2.103}$$

$$\left(\frac{\partial S}{\partial \boldsymbol{q}_a} \right)_{max-ent} = \left(\frac{\partial S}{\partial \boldsymbol{q}_a} \right)_{Gibbs} \tag{2.104}$$

Proof. As before, consider an infinite perfect crystal subject to a homogeneous deformation such as thermal expansion under uniform temperature. According to the Mie-Gruneisen approximation, the Gruneisen parameter for the crystal depends only on the volume V and not on the temperature explicitly and, hence, is the same for all the modes of an atom. It

is defined as

$$\gamma_a(\bar{\boldsymbol{q}}) = -\left(\frac{\partial \ln \bar{\omega}_{ia}(\bar{\boldsymbol{q}})}{\partial \ln V}\right)_T, \quad i = 1,2,3 \tag{2.105a}$$

$$= -\left(\frac{V}{\bar{\omega}_{ia}}\frac{\partial \bar{\omega}_{ia}}{\partial V}\right)_T. \tag{2.105b}$$

Using Eq. (2.105b) we also note that

$$\frac{\partial \bar{\omega}_{ib}}{\partial \bar{\boldsymbol{q}}_a}(\bar{\boldsymbol{q}}) = \frac{\partial \bar{\omega}_{ib}}{\partial V}\frac{\partial V}{\partial \bar{\boldsymbol{q}}_a} = -\bar{\omega}_{ib}\frac{\gamma_a(\bar{\boldsymbol{q}})}{V}\frac{\partial V}{\partial \bar{\boldsymbol{q}}_a}. \tag{2.106}$$

The classical approach gives the following forces by minimizing the free energy,

$$\frac{\partial F}{\partial \bar{\boldsymbol{q}}_a} = \frac{\partial V}{\partial \bar{\boldsymbol{q}}_a} + k_B T \frac{\partial}{\partial \bar{\boldsymbol{q}}_a}\sum_b \log\left[\prod_{i=1}^{3}\bar{\omega}_{ib}(\bar{\boldsymbol{q}})\right] \tag{2.107a}$$

$$= \frac{\partial V}{\partial \bar{\boldsymbol{q}}_a} + k_B T \sum_b \sum_i \frac{1}{\bar{\omega}_{ib}}\frac{\partial \bar{\omega}_{ib}}{\partial \bar{\boldsymbol{q}}_a} \tag{2.107b}$$

$$= \frac{\partial V}{\partial \bar{\boldsymbol{q}}_a} + k_B T \sum_b \sum_i -\frac{\gamma_a(\bar{\boldsymbol{q}})}{V}\frac{\partial V}{\partial \bar{\boldsymbol{q}}_a} \tag{2.107c}$$

$$= \frac{\partial V}{\partial \bar{\boldsymbol{q}}_a} - 3k_B T \sum_b f_a(\bar{\boldsymbol{q}}), \tag{2.107d}$$

where we have used Eq. (2.106) to go from Eq. (2.107b) to Eq. (2.107c) and where

$$f_a(\bar{\boldsymbol{q}}) = \frac{\gamma_a(\bar{\boldsymbol{q}})}{V}\frac{\partial V}{\partial \bar{\boldsymbol{q}}_a}. \tag{2.108}$$

Similarly, the *max-ent* approach yields the following forces

$$\begin{aligned}
\frac{\partial F}{\partial \bar{\boldsymbol{q}}_a} &= \frac{\partial V}{\partial \bar{\boldsymbol{q}}_a} + \frac{3}{2} k_B T \frac{\partial}{\partial \bar{\boldsymbol{q}}_a} \sum_b \log \left[\frac{1}{3} \sum_{i=1}^{3} \bar{\omega}_{ib}^2(\bar{\boldsymbol{q}}) \right] \\
&= \frac{\partial V}{\partial \bar{\boldsymbol{q}}_a} + 3 k_B T \sum_b \frac{1}{\sum_i \bar{\omega}_{ib}}^2 \sum_i \bar{\omega}_{ib} \frac{\partial \bar{\omega}_{ib}}{\partial \bar{\boldsymbol{q}}_a} \\
&= \frac{\partial V}{\partial \bar{\boldsymbol{q}}_a} + 3 k_B T \sum_b -\frac{\gamma_a(\bar{\boldsymbol{q}})}{V} \frac{\partial V}{\partial \bar{\boldsymbol{q}}_a} \\
&= \frac{\partial V}{\partial \bar{\boldsymbol{q}}_a} - 3 k_B T \sum_b f_a(\bar{\boldsymbol{q}}) \,, \qquad \text{(2.109a)}
\end{aligned}$$

where we have made use of Eq. (2.106) and Eq. (2.108). Thus, comparing Eq. (2.107d) and Eq. (2.109a) shows that the forces obtained from both the methods are equal. Since only the last terms of Eq. (2.98c) and Eq. (2.95c) contribute to the derivative of the entropy with respect to $\bar{\boldsymbol{q}}_a$, the calculations are similar to those obtained above. Consequently, we can prove Eq. (2.104). □

Chapter 3

Non-equilibrium finite temperature quasicontinuum method

The prime accomplishment of Chapter 2 is the development of an approximation scheme to construct a macroscopic temperature-dependent energy functional from the microscopic dynamics. However, we emphasize that although we have eliminated the dependence of the energy, $E(\bar{\boldsymbol{q}}, \{S\}, \{\omega\})$, on the microstate or the instantaneous configuration of the system, it is still a function of variables defined at each atom. In other words, the *max-ent* method described so far essentially achieves a homogenization *in time* of the energy of the system. The macroscopic problem of determining the equilibrium configurations of the system still involves minimization over atomistic degrees of freedom, $\bar{\boldsymbol{q}} \in \mathbb{R}^{3N}$, $\{S\} \in \mathbb{R}^N$, and $\{\omega\} \in \mathbb{R}^N$. This presents a significant computational hindrance as we endeavor to model systems of reasonable size on the continuum scale. In this chapter, we seek to alleviate this problem by coarse-graining the atomistic description *in space*. This is accomplished by formulating a finite temperature version of the quasicontinuum theory using the results furnished by the *max-ent* approach.

The discretization of the domain required for the spatial coarse-graining also provides a means of modelling non-equilibrium processes such as heat conduction by solving the heat equation. In this chapter, we also propose a computational scheme for a non-equilibrium

finite temperature framework for the quasicontinuum method. The development is based on the work of Yang et al. [44] on a variational framework for modelling coupled thermo-mechanical problems for dissipative solids. The basic idea is the construction of a joint potential whose Euler-Lagrange equations yield the equilibrium equations and the heat equation in addition.

The chapter is structured as follows. In section 3.1, we review the static theory of the quasicontinuum for zero temperature. Section 3.2 extends the framework of section 3.1 to equilibrium thermodynamic processes. In section 3.3, we present a convergence analysis of the method for homogeneous deformations such as uniform thermal expansion. In section 3.4, we introduce the variational formulation of coupled thermo-mechanical problems, which forms the basis of our work. Finally, section 3.5 presents the details of the non-equilibrium finite temperature formulation of the quasicontinuum method.

3.1 The quasicontinuum method

The theory of the quasicontinuum furnishes a computational scheme for seamlessly bridging the atomistic and the continuum realms. The chief objective of the method is to systematically coarsen an atomistic description by the judicious introduction of kinematic constraints. Although different versions of the theory have been developed, here we review the three-dimensional version of the static quasicontinuum method developed by Knap and Ortiz [21] for zero temperature conditions, which we shall extend to the finite temperature case.

We consider a crystal with N atoms in reference configuration occupying a subset $\mathscr{L}$ of a simple d-dimensional Bravais lattice. Denoting the basis vectors by $\{\boldsymbol{a}_i\,;\, i = 1, \dots d\}$, the

reference coordinates of the atoms are

$$\boldsymbol{X}(\boldsymbol{l}) = \sum_{i=1}^{d} l^i \boldsymbol{a}_i, \ \boldsymbol{l} \in Z \subset \mathbb{R}^d \,. \tag{3.1}$$

$\boldsymbol{l}$ are the lattice coordinates associated with individual atoms, Z is the set of integers, and d is the dimension of space. We define $\boldsymbol{q} \in X \equiv \mathbb{R}^{Nd}$ as the array of atomic positions in the deformed configuration, where X denotes the configuration space of the crystal. We shall also use $\boldsymbol{q}(\boldsymbol{l}), \boldsymbol{l} \in \mathscr{L}$ to denote the coordinates of an individual atom.

At zero temperature, since the atoms do not exhibit rapid oscillations around their mean positions, the energy of the crystal is a function $E(\boldsymbol{q})$ expressed through the use of interatomic potentials. In the case of applied loads, we assume them to be conservative and to derive from an external potential $\Phi^{ext}(\boldsymbol{q})$. Hence, the total potential energy is

$$\Phi(\boldsymbol{q}) = E(\boldsymbol{q}) + \Phi^{ext}(\boldsymbol{q}) \,. \tag{3.2}$$

In addition, the crystal may be subjected to displacement boundary conditions over parts of its boundary. Then, the problem of determining the metastable equilibrium configurations of the system is a problem of seeking the local minima of the energy functional $\Phi(\boldsymbol{q})$, consistent with the essential boundary conditions. This may be stated as

$$\min_{\boldsymbol{q} \in X} \Phi(\boldsymbol{q}) \,. \tag{3.3}$$

For systems with a very large number of atoms, this minimization problem presents a significant computational burden. The essence of the theory of the quasicontinuum lies in replacing Eq. (3.3) by an approximate minimization problem having the flexibility of pre-

serving atomistic resolution in the regions of interest and treating atoms collectively where deformations are slow varying on the scale of the lattice. There are three key components of the quasicontinuum framework that impart the method its capabilities. We review these below.

Constrained minimization

The main step in the method is to replace Eq. (3.3) by a constrained minimization of $\Phi(\boldsymbol{q})$ over a suitably chosen subspace X_h of X. X_h is constructed by selecting a reduced set $\mathscr{L}_h \subset \mathscr{L}$ of $N_h < N$ representative atoms or nodes. The selection is done based on the local variation in the deformation field. Introducing a triangulation $\mathscr{T}_h$ over $\mathscr{L}_h$, the positions of the remaining atoms are determined by piecewise linear interpolation of the nodal coordinates. By construction, the interpolated position of an atom denoted by $\boldsymbol{q}_h(\boldsymbol{l})$ is

$$\boldsymbol{q}_h(\boldsymbol{l}) = \sum_{\boldsymbol{l}_h \in \mathscr{L}_h} \varphi(\boldsymbol{l}|\boldsymbol{l}_h)\boldsymbol{q}_h(\boldsymbol{l}_h)\,, \tag{3.4}$$

where $\varphi(\boldsymbol{l}|\boldsymbol{l}_h)$ denotes the continuous and piecewise linear shape function associated with the representative atom, $\boldsymbol{l}_h \in \mathscr{L}_h$, evaluated at the point $\boldsymbol{X}(\boldsymbol{l})$. Its domain is restricted to the simplices $K \in \mathscr{T}_h$ incident on $\boldsymbol{l}_h$, and it satisfies

$$\varphi(\boldsymbol{l}'_h|\boldsymbol{l}_h) = \delta(\boldsymbol{l}'_h|\boldsymbol{l}_h) \tag{3.5a}$$

$$\sum_{\boldsymbol{l}_h \in \mathscr{L}_h} \varphi(\boldsymbol{l}|\boldsymbol{l}_h) = 1\,, \tag{3.5b}$$

where δ is the Dirac delta function. Eq. (3.5b) ensures that a constant field is interpolated exactly by the basis functions. The constrained minimization problem may now be stated

as

$$\min_{\boldsymbol{q}_h \in X_h} \Phi(\boldsymbol{q}_h)\,. \tag{3.6}$$

The corresponding reduced equations of equilibrium are

$$\boldsymbol{f}_h(\boldsymbol{l}_h) = \sum_{\boldsymbol{l} \in \mathscr{L}} \boldsymbol{f}(\boldsymbol{l})\, \varphi(\boldsymbol{l}|\boldsymbol{l}_h) = \boldsymbol{0}\,, \tag{3.7}$$

where

$$\boldsymbol{f}(\boldsymbol{l}) = \frac{\partial \Phi}{\partial \boldsymbol{q}(\boldsymbol{l})}(\boldsymbol{q})\,. \tag{3.8}$$

Sampling over clusters

For a large crystal, performing full lattice sums as required in (3.7) is also an expensive computation. In particular, summing over all the atoms in the regions where the deformation field is slow varying beats the purpose of the method. A way to circumvent this difficulty is provided by sampling the behavior of the crystal over clusters of atoms around the representative atoms, as shown in Figure 3.1. This is demonstrated as follows. Let $\mathscr{C}(\boldsymbol{l}_h)$ be a cluster of lattice sites within a sphere of radius $r(\boldsymbol{l}_h)$ centered at the node $\boldsymbol{l}_h$. That is,

$$\mathscr{C}(\boldsymbol{l}_h) = \{\boldsymbol{l} : |\boldsymbol{X}(\boldsymbol{l}) - \boldsymbol{X}(\boldsymbol{l}_h)| \leq r(\boldsymbol{l}_h)\}\ . \tag{3.9}$$

Let $g(\boldsymbol{l})$ be a lattice function whose sum over the lattice is

$$S = \sum_{\boldsymbol{l} \in \mathscr{L}} g(\boldsymbol{l})\,. \tag{3.10}$$

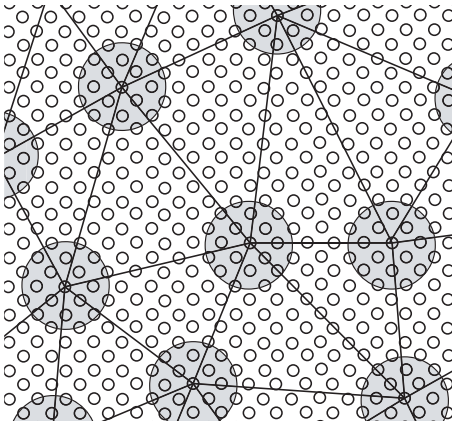

Figure 3.1: Clusters of atoms in the triangulation $\mathscr{T}_h$ of the crystal.

Then, the cluster summation rule approximates S by

$$S \approx S_h = \sum_{\boldsymbol{l}_h \in \mathscr{L}_h} n_h(\boldsymbol{l}_h) S(\boldsymbol{l}_h)\,, \tag{3.11}$$

where $S(\boldsymbol{l}_h)$ denotes the sum over all atoms in the cluster $\mathscr{C}(\boldsymbol{l}_h)$, i.e.,

$$S(\boldsymbol{l}_h) = \sum_{\boldsymbol{l} \in \mathscr{C}(\boldsymbol{l}_h)} g(\boldsymbol{l})\,. \tag{3.12}$$

The cluster weights $n_h(\boldsymbol{l}_h)$ associated with the nodes, $\boldsymbol{l}_h \in \mathscr{L}_h$, are computed by requiring that the cluster summation rule (3.11) be exact for all basis functions. That is,

$$\sum_{\boldsymbol{l} \in \mathscr{L}} \varphi(\boldsymbol{l}|\boldsymbol{l}_h) = \sum_{\boldsymbol{l}'_h \in \mathscr{L}_h} n_h(\boldsymbol{l}'_h) \sum_{\boldsymbol{l} \in \mathscr{C}(\boldsymbol{l}'_h)} \varphi(\boldsymbol{l}|\boldsymbol{l}_h), \;\; \forall\, \boldsymbol{l}_h \in \mathscr{L}_h\,. \tag{3.13}$$

Using the cluster summation rule (3.11), the equations of equilibrium (3.7) are further

reduced to the form

$$\boldsymbol{f}_h(\boldsymbol{l}_h) \approx \sum_{\boldsymbol{l}'_h \in \mathscr{L}_h} n_h(\boldsymbol{l}'_h) \left[\sum_{\boldsymbol{l} \in \mathscr{C}(\boldsymbol{l}'_h)} \frac{\partial F}{\partial \bar{\boldsymbol{q}}(\boldsymbol{l})} \varphi(\boldsymbol{l}|\boldsymbol{l}_h) \right] = \boldsymbol{0}\,. \tag{3.14}$$

Adaptive refinement

The flexibility of the quasicontinuum method is further enhanced by the use of mesh adaption in order to tailor the computational mesh to the structure of the deformation field. Due to the lack of a rigorous theory relating the mesh size to suitable bounds on the energy for discrete systems, empirical adaption indicators based on the displacement field of the crystal are currently used. Specifically, the adaption indicator $\varepsilon(K)$ for simplex K is measured as

$$\varepsilon(K) = \sqrt{|II_E(K)|}h(K)\,, \tag{3.15}$$

where $II_E(K)$ is the second invariant of the Lagrangian strain tensor for simplex K, and $h(K)$ is the size of K. The element K is deemed acceptable if

$$\frac{\varepsilon(K)}{b} < TOL \tag{3.16}$$

for some prescribed tolerance $TOL < 1$ and is targeted for refinement otherwise. b denotes the magnitude of the smallest Burgers vector of the crystal. Thus, the adaption criterion is designed so that full atomistic resolution is attained when the simplex slips by a full Burgers vector. Evidently, the value of TOL involves a compromise between conflicting demands on accuracy and computational efficiency.

This summarizes the static theory of the quasicontinuum method. For further details and study of convergence characteristics, we refer the reader to [21].

3.2 Extension to equilibrium thermodynamics

As a precursor to the development of the full non-equilibrium finite temperature quasicontinuum method, we present here the framework for modelling equilibrium thermodynamic processes using the quasicontinuum method. One of the merits of our approach is that the finite temperature quasicontinuum method is in accord with the philosophy of the static theory and consequently bears all the features of the latter. Simply put, the finite temperature formulation for equilibrium systems possesses the same structure as the zero temperature formulation, with the distinction that the energy functional to be minimized is no longer the potential energy given in Eq. (3.2) but a temperature-dependent energy furnished by the *max-ent* method. Examples of systems in thermal equilibrium include systems undergoing thermal expansion at uniform temperature or subjected to quasistatic processes, such as nanoindentation or void growth under isothermal conditions. For such phenomena, we wish to determine the metastable configurations of the crystal when the crystal is in thermal equilibrium at a uniform temperature T under the applied loads and boundary conditions. Based on the *max-ent* approximation scheme, the minimization problem describing such processes may be enunciated as

$$\min_{\bar{\boldsymbol{q}}\in X}\min_{\{\omega\}\in\mathbb{R}^N}\Phi(\bar{\boldsymbol{q}},T,\{\omega\}) \tag{3.17}$$

with

$$\Phi(\bar{\boldsymbol{q}},T,\{\omega\}) = F(\bar{\boldsymbol{q}},T,\{\omega\}) + \Phi^{ext}(\bar{\boldsymbol{q}})\,, \tag{3.18}$$

where we have assumed, as before, that the external loads are conservative and hence derivable from an external potential, $\Phi^{ext}(\bar{\boldsymbol{q}})$. F is the Helmholtz free energy of the crystal,

derived by substituting the local relation (2.35) in the Legendre transformation of the internal energy given in Eq. (2.36).

Our aim is to determine the solutions of Eq. (3.17) by using the three building blocks of static QC : (i) constrained minimization of the atomistic free energy of the crystal; (ii) cluster summation rules to compute effective equilibrium equations; and (iii) adaptive refinement of the computational mesh to track the displacement field. We note, however, that the third component plays a role only in incremental minimization problems and not in problems with one-step solutions such as uniform thermal expansion. Following the procedure described in section 3.1, we select a reduced set $\mathscr{L}_h$ of $N_h < N$ representative atoms based on the local variation of the displacement field. The positions, temperature, and approximate frequencies of the remaining atoms are interpolated over the nodes using piecewise linear shape functions defined before:

$$\bar{\boldsymbol{q}}_h(\boldsymbol{l}) = \sum_{\boldsymbol{l}_h \in \mathscr{L}_h} \varphi(\boldsymbol{l}|\boldsymbol{l}_h)\bar{\boldsymbol{q}}_h(\boldsymbol{l}_h) \tag{3.19a}$$

$$T_h(\boldsymbol{l}) = \sum_{\boldsymbol{l}_h \in \mathscr{L}_h} \varphi(\boldsymbol{l}|\boldsymbol{l}_h)T_h(\boldsymbol{l}_h) \tag{3.19b}$$

$$\omega_h(\boldsymbol{l}) = \sum_{\boldsymbol{l}_h \in \mathscr{L}_h} \varphi(\boldsymbol{l}|\boldsymbol{l}_h)\omega_h(\boldsymbol{l}_h)\,. \tag{3.19c}$$

We must emphasize that since the mean field parameter $\omega(\boldsymbol{l})$ is an approximation for the average local frequency of that atom, the variation in $\{\omega\}$ follows the displacement field. This is because the frequencies of an atom are computed from the eigenvalues of the local dynamical matrix associated with that atom, which in turn depends on the deformed configuration of the neighborhood of the atom. Therefore, in the regions where the displacement field is uniform, $\{\omega\}$ also varies slowly on the scale of the lattice, since all the

atoms experience very similar environment. This provides a rationale for assuming the frequencies as a continuous field far from the atomistic domain and interpolating it over the representative atoms. The equilibrium equations are obtained by taking variations of the energy functional with respect to the nodal unknowns $(\bar{\boldsymbol{q}}_h(\boldsymbol{l}_h), \omega_h(\boldsymbol{l}_h))$ and enforcing stationarity. The computational cost of solving the equilibrium equations can be further reduced by avoiding full lattice sums. Introducing cluster summation rules, the final form of the equilibrium equations is

$$\sum_{\boldsymbol{l}'_h \in \mathscr{L}_h} n_h(\boldsymbol{l}'_h) \left[\sum_{\boldsymbol{l} \in \mathscr{C}(\boldsymbol{l}'_h)} \frac{\partial \Phi}{\partial \bar{\boldsymbol{q}}(\boldsymbol{l})} \varphi(\boldsymbol{l}|\boldsymbol{l}_h) \right] = \boldsymbol{0} \tag{3.20a}$$

$$\sum_{\boldsymbol{l}'_h \in \mathscr{L}_h} n_h(\boldsymbol{l}'_h) \left[\sum_{\boldsymbol{l} \in \mathscr{C}(\boldsymbol{l}'_h)} \frac{\partial \Phi}{\partial \omega(\boldsymbol{l})} \varphi(\boldsymbol{l}|\boldsymbol{l}_h) \right] = \boldsymbol{0}\,. \tag{3.20b}$$

Using the calculations shown in section 2.4 for different interatomic potentials, the derivatives of the free energy required in the above equations are evaluated as

$$\frac{\partial F}{\partial \bar{\boldsymbol{q}}(\boldsymbol{l})} = \frac{\partial}{\partial \bar{\boldsymbol{q}}(\boldsymbol{l})} \left[E(\bar{\boldsymbol{q}}, \{S\}, \{\omega\}) - \sum_{\boldsymbol{l}} T(\boldsymbol{l}) S(\boldsymbol{l}) \right] \tag{3.21a}$$

$$\frac{\partial F}{\partial \omega(\boldsymbol{l})} = \frac{\partial}{\partial \omega(\boldsymbol{l})} \left[E(\bar{\boldsymbol{q}}, \{S\}, \{\omega\}) - \sum_{\boldsymbol{l}} T(\boldsymbol{l}) S(\boldsymbol{l}) \right], \tag{3.21b}$$

where we have replaced $S(\boldsymbol{l})$ by its local expression given in Eq. (2.35).

Finally, we require an appropriate adaption criterion in order to refine the mesh according to the deformation of the crystal. In problems such as nanoindentation at finite temperature, the entire crystal undergoes thermal expansion in addition to the localized deformation under the indenter. Since we are interested in tracking atomistically the deformation in the vicinity of the indenter, we modify the adaption criterion as follows to eliminate or at least

reduce the remeshing due to thermal expansion. We define $\varepsilon(K)$ as

$$\varepsilon(K) = \sqrt{|II_{E^d}(K)|}h(K)\,, \tag{3.22}$$

where $II_{E^d}(K)$ is the second invariant of the deviatoric part of the Lagrangian strain tensor. However, we found that this may not suffice to inhibit mesh refinement all over the crystal under certain boundary conditions that do not allow the crystal to expand freely. We circumvent this difficulty by allowing the crystal to expand freely prior to indentation and then using the deformed configuration as a reference configuration for computing $II_{E^d}(K)$ during the subsequent load increments.

3.3 Convergence analysis

In this section, we present a convergence analysis of the finite temperature quasicontinuum approach under isothermal conditions. In particular, we seek to understand the effect of coarsening on the energetics of the system by computing the error introduced by the quasicontinuum approximation. To this end, we consider a perfect crystal with periodic boundary conditions subjected to uniform temperature. We show that for a homogeneous deformation, the quasicontinuum approach gives the exact energy of the crystal irrespective of the degree of coarse-graining.

Theorem 3.3.1. *Consider a perfect crystal with N atoms and periodic boundary conditions occupying a subset $\mathscr{L}$ of a simple d-dimensional Bravais lattice. Let $\mathscr{L}_h \subset \mathscr{L}$ be a collection of $N_h < N$ representative atoms of the crystal. Then, for a homogeneous deformation under*

uniform temperature,

$$\sum_{\boldsymbol{l}_h \in \mathscr{L}_h} n_h(\boldsymbol{l}_h) \left[\sum_{\boldsymbol{l} \in \mathscr{C}(\boldsymbol{l}_h)} E(\boldsymbol{l}) \right] = \sum_{\boldsymbol{l} \in \mathscr{L}} E(\boldsymbol{l}) \,. \tag{3.23}$$

Proof. When an infinite perfect crystal or a perfect crystal with periodic boundary conditions is subjected to uniform temperature or, more generally, a homogeneous deformation, every atom sees exactly the same environment and, consequently, has the same energy:

$$E(\boldsymbol{l}) = E_1, \;\; \forall \; \boldsymbol{l} \in \mathscr{L} \,.$$

Thus, the total internal energy of the system furnished by the *max-ent* approach becomes

$$E(\bar{\boldsymbol{q}}, \{S\}, \{\omega\}) = \sum_{\boldsymbol{l} \in \mathscr{L}} E(\boldsymbol{l}) = N E_1 \,. \tag{3.24}$$

The quasicontinuum approximation of the total energy is obtained by using the cluster summation rule:

$$E_h(\boldsymbol{l}_h) = \sum_{\boldsymbol{l}_h \in \mathscr{L}_h} n_h(\boldsymbol{l}_h) \sum_{\boldsymbol{l} \in \mathscr{C}(\boldsymbol{l}_h)} E(\boldsymbol{l}) \tag{3.25a}$$

$$= \sum_{\boldsymbol{l}_h \in \mathscr{L}_h} n_h(\boldsymbol{l}_h) N(\boldsymbol{l}_h) E_1 \,, \tag{3.25b}$$

where $N(\boldsymbol{l}_h)$ is the number of atoms in the cluster around node $\boldsymbol{l}_h$. We recall that the weights used in the cluster summation rules are determined such that the shape functions associated with all the nodes are summed exactly. That is,

$$\sum_{\boldsymbol{l}'_h \in \mathscr{L}_h} n_h(\boldsymbol{l}'_h) \sum_{\boldsymbol{l} \in \mathscr{C}(\boldsymbol{l}'_h)} \varphi(\boldsymbol{l} | \boldsymbol{l}_h) = \sum_{\boldsymbol{l} \in \mathscr{L}} \varphi(\boldsymbol{l} | \boldsymbol{l}_h), \;\; \forall \; \boldsymbol{l}_h \in \mathscr{L}_h \,. \tag{3.26}$$

Summing both sides over $\boldsymbol{l}_h \in \mathscr{L}_h$, rearranging the sums, and using the property

$$\sum_{\boldsymbol{l}_h \in \mathscr{L}_h} \varphi(\boldsymbol{l}|\boldsymbol{l}_h) = 1\,, \tag{3.27}$$

Eq. (3.26) reduces to

$$\sum_{\boldsymbol{l}'_h \in \mathscr{L}_h} n_h(\boldsymbol{l}'_h) N(\boldsymbol{l}_h) = N\,. \tag{3.28}$$

Multiplying Eq. (3.28) by E_1 and comparing the expressions with Eq. (3.24) and Eq. (3.25b), we conclude that

$$E_h = E \tag{3.29}$$

and that this equality of energy is independent of the degree of coarsening. □

As a concluding remark, we note that this result is valid for infinite crystals and that for finite crystals, the surface effects should introduce some error. Nevertheless, the result demonstrates that in the regions within the bulk of the crystal and away from defects, the atoms experience similar environments and deformations and, consequently, the quasicontinuum energy should be a very good approximation.

3.4 Variational formulation for thermo-mechanical problems

We present here a concise review of a variational formulation for coupled thermo-mechanical boundary-value problems for general dissipative solids proposed by Yang et al. in [44]. This work forms the basis for the development of a non-equilibrium finite temperature quasicontinuum method proposed in the next section.

The aim of this work is to characterize variationally the solutions of equilibrium problems for an inelastic deformable solid capable of conducting heat. Specifically, the work shows

the existence of a joint potential function whose Euler-Lagrange equations yield the equilibrium equations, the kinetic relations, and the conservation of energy. A general dissipative solid may be understood as a deformable solid, undergoing large deformations, possessing viscosity and internal processes, and conducting heat. However, in the context of the current work, we shall restrict this review to conducting thermoelastic solids since we do not assume any kinetic relations such as flow and hardening rules or viscosity laws in our work. As we shall see in the next section, the only kinetic relation that we introduce *a priori* is the Fourier's law of heat conduction.

To this end, we consider a body occupying a region $B \subset \mathbb{R}^3$ in reference configuration and undergoing a thermodynamic process. The motion of the body is described by a time-dependent deformation mapping $\varphi : B \times [a, b] \to \mathbb{R}^3$, where $[a, b]$ is the time interval of the motion. The body may be subjected to essential boundary conditions for the displacement and temperature over parts of its boundary. Let $\bar{H}$ be the prescribed outward heat flux on the Neumann boundary $\partial_N B$, and let $\bar{\boldsymbol{T}}$ be the applied traction on the traction boundary $\partial_T B$. We assume that there exists an internal energy density expressed as a function of the local state,

$$E = E(\boldsymbol{F}, S)\,, \tag{3.30}$$

where $\boldsymbol{F} = \operatorname{Grad}\varphi$ is the deformation gradient, and S is the local entropy density per unit undeformed volume. Then, the equilibrium stress is given by

$$\boldsymbol{P}^e \equiv \partial_{\boldsymbol{F}} E(\boldsymbol{F}, S)\,. \tag{3.31}$$

A theorem of Coleman and Noll shows that the local equilibrium temperature is given by

the relation

$$\Theta = \partial_S E = E(\boldsymbol{F}, S) \tag{3.32}$$

and that all processes must satisfy the dissipation inequality. For the variational formulation, it is necessary to differentiate between the equilibrium temperature Θ and an external temperature field T. Although they are equal everywhere at equilibrium, the condition is not imposed *a priori*. We also assume that a Fourier potential $\chi(\boldsymbol{G})$ exists such that

$$\boldsymbol{H} = \partial_{\boldsymbol{G}}\chi(\boldsymbol{G})\,, \tag{3.33}$$

where $\boldsymbol{H}$ is the heat flux, and $\boldsymbol{G} = -T^{-1}\mathrm{Grad}\,T$. χ is assumed to be quadratic and strictly convex in G, which guarantees a unique minimum.

Variational formulation

A rate problem is understood as a problem of finding the rate of change of the state of the body given its current state and appropriate forcing and boundary conditions. For a thermoelastic problem, this means the problem of determining $(T, \dot{S})$ given the current local state $(\boldsymbol{F}, S)$. To this end, we construct a joint potential function of the following form:

$$\begin{aligned}\Phi[T, \dot{S}] = &\int_B [(\Theta - T)\dot{S} - \chi(\boldsymbol{G})]dV \\ &+ \int_B R\,Q \log\frac{T}{T_0}\,dV - \int_{\partial_N B} \bar{H} \log\frac{T}{T_0}\,dS\,,\end{aligned} \tag{3.34}$$

where Q is the distributed heat source per unit mass, and T_0 is a reference temperature. Then, according to [44], the problem of determining solutions for the thermoelastic rate

problem may be stated as a two field variational problem:

$$\inf_{\dot{S}} \sup_{T} \Phi\left[T, \dot{S}\right]. \tag{3.35}$$

Taking variations of this potential with respect to the fields $(T, \dot{S})$ and enforcing stationarity yields the thermoelastic rate problem in strong form:

$$T\,\dot{S} = -\mathrm{Div}\boldsymbol{H} + R\,Q \qquad \text{in } B, \tag{3.36a}$$

$$\boldsymbol{H}\cdot\boldsymbol{N} = \bar{H} \qquad \text{on } \partial_N B, \tag{3.36b}$$

$$T = \bar{T} \qquad \text{on } \partial B \backslash \partial_N B, \tag{3.36c}$$

$$T = \Theta \qquad \text{in } B. \tag{3.36d}$$

Thus, the general rate problem for thermoelastic conducting solids is equivalent to the stationarity principle:

$$\delta\,\Phi = 0\,. \tag{3.37}$$

Incremental formulation

We now present a time-discretized version of the variational problem as established in [44]. The purpose of time-discretization is to reduce the modelling of time-dependent phenomena to a sequence of incremental problems, each characterized by a variational principle. For a rigorous derivation of the variational updates, we refer the reader to [44]. Below, we give an outline of the incremental extremum problem formulated by identifying a convenient joint potential which is consistent with the field equations. To this end, we consider a sequence of times $t_0, \ldots, t_n \ldots$ and seek to characterize the state (φ, T, S) of the solid at

those times. Specifically, we wish to determine approximately the state $(\varphi_{n+1}, T_{n+1}, S_{n+1})$ at t_{n+1} assuming that the state (φ_n, T_n, S_n) is known. We construct a family of incremental potentials based on the backward Euler finite difference scheme:

$$\begin{aligned}
&\Phi_n[\varphi_{n+1}, T_{n+1}, S_{n+1}] = \\
&\int_B [E_{n+1} - E_n - T_{n+1}(S_{n+1} - S_n) - \triangle t\, \chi_{n+1}]\, dV \\
&- \int_B R\, \boldsymbol{B}_{n+1} \cdot (\varphi_{n+1} - \varphi_n)\, dV - \int_{\partial_T B} \bar{\boldsymbol{T}}_{n+1} \cdot (\varphi_{n+1} - \varphi_n)\, dS \\
&+ \int_B \triangle t\, R\, Q_{n+1} \log \frac{T_{n+1}}{T_n}\, dV - \int_{\partial_N B} \triangle t\, \bar{H}_{n+1} \log \frac{T_{n+1}}{T_n}\, dS\,,
\end{aligned} \tag{3.38}$$

with

$$\chi_{n+1} = \chi\left(\boldsymbol{G}_{n+1}\right),\ \boldsymbol{G}_{n+1} = -\text{Grad}\, \log \frac{T_{n+1}}{T_n}\,. \tag{3.39}$$

Then the incremental variational problem becomes

$$\inf_{\varphi_{n+1}} \inf_{S_{n+1}} \sup_{T_{n+1}} \Phi_n\left[\varphi_{n+1}, T_{n+1}, S_{n+1}\right]. \tag{3.40}$$

Taking variations and enforcing stationarity as before yields the equilibrium equation, the heat equation, and the natural boundary conditions:

$$\text{Div}\, \boldsymbol{P}^e_{n+1} + R\, \boldsymbol{B}_{n+1} = O(\triangle t) \qquad \text{in } B, \tag{3.41a}$$

$$\boldsymbol{P}^e_{n+1} \cdot \boldsymbol{N} - \bar{\boldsymbol{T}}_{n+1} = O(\triangle t) \qquad \text{on } \partial_T B, \tag{3.41b}$$

$$\frac{S_{n+1} - S_n}{\triangle t} = -\frac{1}{T_{n+1}} \text{Div}\, \partial_{\boldsymbol{G}_{n+1}} \chi_{n+1} + \frac{1}{T_{n+1}} R\, Q_{n+1} \qquad \text{in } B, \tag{3.41c}$$

$$\partial_{\boldsymbol{G}_{n+1}} \chi_{n+1} \cdot \boldsymbol{N} = \bar{H}_{n+1} \qquad \text{on } \partial_N B, \tag{3.41d}$$

$$\partial_{S_{n+1}} E_{n+1} - T_{n+1} = O(\triangle t) \qquad \text{in } B. \tag{3.41e}$$

All field equations are recovered as $\triangle t \to 0$. Thus, the time-discretized variational formulation for dissipative solids provides a means of reducing the rate problem to an incremental problem with a variational structure. Moreover, the incremental potential Φ_n reflects both the energetics as well as the kinetics of the material. This time-discretization of the rate problem provides a way of incorporating the heat equation into the finite temperature quasicontinuum framework that was presented in section 3.2. We shall elaborate on this development in the following section.

3.5 Quasicontinuum method and heat transport

In this section, we develop a non-equilibrium finite temperature version of the quasicontinuum approach based on the *max-ent* approximation scheme. The work is based on the variational framework for coupled thermo-mechanical behavior of dissipative solids reviewed in the previous section. A joint potential is constructed whose Euler-Lagrange equations are the equilibrium and the energy balance equations. The rate problem is then formulated as an incremental minimization problem. Following the review in the previous section, we construct an incremental potential based on the backward Euler finite difference scheme as

$$\begin{aligned}
&\Phi_n[\bar{\boldsymbol{q}}_{n+1}, \{T_{n+1}\}, \{S_{n+1}\}, \{\omega_{n+1}\}] = \\
&(E_{n+1} - E_n) - \sum_{\boldsymbol{l}\in\mathscr{L}} T_{n+1}(\boldsymbol{l})[S_{n+1}(\boldsymbol{l}) - S_n(\boldsymbol{l})] + \int_B \Delta_{n+1}(\boldsymbol{G}_{n+1}(\boldsymbol{X}))\triangle t\, dV \\
&+ \int_B \triangle t\, R\, Q_{n+1} \log\frac{T_{n+1}}{T_n}\, dV - \int_{\partial_N B} \triangle t\, \bar{H}_{n+1} \log\frac{T_{n+1}}{T_n}\, dS\,,
\end{aligned} \tag{3.42}$$

where $\triangle t$ is the time step, $\boldsymbol{G}_{n+1} = -T_{n+1}^{-1}\mathrm{Grad}T_{n+1}$, and E_{n+1} is the global internal energy of the crystal at $t = (n+1)\triangle t$, furnished by the *max-ent* scheme. $B \subset \mathbb{R}^3$ denotes the region occupied by the crystal in the reference configuration. $\bar{H}$ denotes the outward heat

flux prescribed on the Neumann boundary $\partial_N B$. Q_{n+1} is the local heat generated at time t_{n+1}. In the current work, we neglect any heat sources and hence assume $Q_{n+1} = 0$. For general dissipative solids, Δ may be a kinetic potential which gives the viscosity law, rate sensitivity, and heat conduction. In the context of this work,

$$\Delta = -\chi\,,$$

where χ is a Fourier potential. As before, χ is assumed to be strictly convex and quadratic in $\boldsymbol{G}$. We also assume the Fourier law of heat conduction, which furnishes a linear dependence of the heat flux on the temperature gradient at that point:

$$\partial_{\boldsymbol{G}}\Delta_{n+1} = -\boldsymbol{H}_{n+1} = \kappa\,\mathrm{Grad}\,T_{n+1}(\boldsymbol{l})\,. \tag{3.43}$$

We wish to note that the Fourier law is a phenomenological relation and, therefore, introduces the heat conductivity, κ, as an empirical parameter into the model in addition to the empirical interatomic potential. The incremental variational problem may be enunciated as

$$\inf_{\bar{\boldsymbol{q}}_{n+1}}\inf_{\{S_{n+1}\}}\inf_{\{\omega_{n+1}\}}\sup_{\{T_{n+1}\}}\Phi_n[\bar{\boldsymbol{q}}_{n+1},\{T_{n+1}\},\{S_{n+1}\},\{\omega_{n+1}\}]\,. \tag{3.44}$$

The temperature field and $\{\omega\}$ can take only positive values. Therefore, for the purpose of numerical implementation, we recast the problem in terms of new fields defined as

$$v_{n+1}(\boldsymbol{l}) = \log\frac{T_{n+1}(\boldsymbol{l})}{T_n(\boldsymbol{l})} \tag{3.45a}$$

$$\mu_{n+1}(\boldsymbol{l}) = \log\frac{\omega_{n+1}(\boldsymbol{l})}{\omega_n(\boldsymbol{l})} \tag{3.45b}$$

and which can take values on the entire real line $\mathbb{R}$. We follow the same procedure as presented in sections 3.1 and 3.2 to constrain the extremum problem over representative atoms. To this end, we also introduce the following interpolations over nodal variables using piecewise linear shape functions:

$$\bar{\boldsymbol{q}}_h(\boldsymbol{l}) = \sum_{\boldsymbol{l}_h \in \mathscr{L}_h} \varphi(\boldsymbol{l}|\boldsymbol{l}_h)\bar{\boldsymbol{q}}_h(\boldsymbol{l}_h) \tag{3.46a}$$

$$v^h_{n+1}(\boldsymbol{l}) = \sum_{\boldsymbol{l}_h \in \mathscr{L}_h} \varphi(\boldsymbol{l}|\boldsymbol{l}_h)v^h_{n+1}(\boldsymbol{l}_h) \tag{3.46b}$$

$$\mu^h_{n+1}(\boldsymbol{l}) = \sum_{\boldsymbol{l}_h \in \mathscr{L}_h} \varphi(\boldsymbol{l}|\boldsymbol{l}_h)\mu^h_{n+1}(\boldsymbol{l}_h)\,. \tag{3.46c}$$

Finally, we take variations of the incremental energy functional, Φ_n, with respect to the nodal unknowns. Enforcing stationarity of the incremental potential yields the following equilibrium equations:

$$\sum_{\boldsymbol{l}'_h \in \mathscr{L}_h} n_h(\boldsymbol{l}'_h) \left[\sum_{\boldsymbol{l} \in \mathscr{C}(\boldsymbol{l}'_h)} \frac{\partial E_{n+1}}{\partial \bar{\boldsymbol{q}}_{n+1}(\boldsymbol{l})} \varphi(\boldsymbol{l}|\boldsymbol{l}_h) \right] = 0 \tag{3.47a}$$

$$\sum_{\boldsymbol{l}'_h \in \mathscr{L}_h} n_h(\boldsymbol{l}'_h) \left[\sum_{\boldsymbol{l} \in \mathscr{C}(\boldsymbol{l}'_h)} \left(\frac{\partial E_{n+1}}{\partial S_{n+1}(\boldsymbol{l})} - T_{n+1}(\boldsymbol{l}) \right) \varphi(\boldsymbol{l}|\boldsymbol{l}_h) \right] = 0 \tag{3.47b}$$

$$\sum_{\boldsymbol{l}'_h \in \mathscr{L}_h} n_h(\boldsymbol{l}'_h) \left[\sum_{\boldsymbol{l} \in \mathscr{C}(\boldsymbol{l}'_h)} \frac{\partial E_{n+1}}{\partial \mu_{n+1}(\boldsymbol{l})} \varphi(\boldsymbol{l}|\boldsymbol{l}_h) \right] = 0 \tag{3.47c}$$

and the energy balance equation:

$$\begin{aligned} &- \sum_{\boldsymbol{l}'_h \in \mathscr{L}} n_h(\boldsymbol{l}'_h) \left[\sum_{\boldsymbol{l} \in \mathscr{C}(\boldsymbol{l}'_h)} \left(S_{n+1}(\boldsymbol{l}) - S_n(\boldsymbol{l})\right) T_n(\boldsymbol{l}) \exp[v_{n+1}(\boldsymbol{l})] \varphi(l|l_h) \right] \\ &- \int_B \kappa \triangle t \left[\operatorname{Grad} T_n(\boldsymbol{X}) + T_n(\boldsymbol{X}) \operatorname{Grad} v_{n+1}(\boldsymbol{X}) \right] \exp[v_{n+1}(\boldsymbol{X})] \operatorname{Grad} \varphi(\boldsymbol{X}|l_h)\, dV \\ &- \int_{\partial_N B} \triangle t\, \bar{H}_{n+1}\, \varphi(\boldsymbol{X}|\boldsymbol{l}_h)\, dS = 0\,. \end{aligned} \tag{3.48}$$

If external loads are applied, we assume them to be conservative as before, and the energy functional E in Eq. (3.47a) is replaced by

$$E\left(\bar{\boldsymbol{q}}_{n+1}, \{S_{n+1}\}, \{\omega_{n+1}\}\right) + \Phi^{ext}\left(\bar{\boldsymbol{q}}\right). \tag{3.49}$$

We recall from section 2.2 that enforcing the equipartition of energy and using the relation $\sigma^2(\boldsymbol{l}) = k_B\, T(\boldsymbol{l})$ yields a local equilibrium relation between entropy and temperature:

$$S_{n+1}(\boldsymbol{l}) = 3k_B\, \log \frac{k_B T_{n+1}(\boldsymbol{l})}{\hbar\, \omega_{n+1}(\boldsymbol{l})} + 4k_B - k_B\, \log N\,, \tag{3.50}$$

and we use it to substitute for $S_{n+1}(\boldsymbol{l})$ in the equations above. Consequently, we do not have to solve Eq. (3.47b). Nevertheless, we do evaluate the right-hand side of Eq. (3.47b) in all our numerical tests and confirm that Eq. (3.47b) is satisfied automatically. Furthermore, using Eq. (3.50), the change in the local entropy has the following form:

$$S_{n+1}(\boldsymbol{l}) - S_n(\boldsymbol{l}) = 3k_B\left[v_{n+1}(\boldsymbol{l}) - \mu_{n+1}(\boldsymbol{l})\right]\,. \tag{3.51}$$

We observe from Eq. (3.48) that the rate term of the heat equation is computed using the cluster summation rule of the quasicontinuum method, whereas the diffusion term in the heat equation is an integral and is computed using the triangulation $\mathscr{T}_h$, as in the finite element framework [14]. We review the details of the calculations below. Let us define

$$g(\boldsymbol{X}) = \kappa\, \triangle t\big[\operatorname{Grad} T_n(\boldsymbol{X}) + T_n(\boldsymbol{X})\operatorname{Grad} v_{n+1}(\boldsymbol{X})\big]\, \exp[v_{n+1}(\boldsymbol{X})] \operatorname{Grad} \varphi(\boldsymbol{X}|l_h)\,. \tag{3.52}$$

The volume integral in the diffusion term of Eq. (3.48) may be computed over the elements as

$$\int_B g\left(\boldsymbol{X}\right) dV = \sum_{e_\alpha} \int_{|e_\alpha|} g\left(\boldsymbol{X}\right) dV \,. \tag{3.53}$$

In the case of isoparametric elements, these integrals over elements are further simplified by evaluating on a standard computational domain. Denoting the integral over an element by I, we have

$$I = \int_{|\hat{e}|} g(\theta)\, J_\alpha(\theta)\, d\theta \,, \tag{3.54}$$

where

$$J_\alpha(\theta) = \det\left(D\, f_\alpha(\theta)\right) \tag{3.55}$$

denotes the Jacobian of the isoparametric mapping from the element e_α to the computational domain. Finally, the integral on the computational domain is computed using numerical quadrature as

$$I \approx \sum_{q=1}^{r} g\left(\theta_q\right) J_\alpha(\theta_q)\, W_q \,. \tag{3.56}$$

In our calculations presented in Chapter 5, we have used the 5-point formula for tetrahedral elements tabulated in [14]. This completes the formulation of the non-equilibrium finite temperature quasicontinuum theory for general anharmonic potentials and with heat conduction.

3.6 Quasi-harmonic approximation

We recall that by assuming a quasi-harmonic approximation for the potential energy in the *max-ent* approach, all the thermodynamic potentials can be obtained in closed form. Moreover, for a perfect crystal with local quasi-harmonic approximation, these expressions

become identical to those derived from the canonical ensemble approach. Hence, keeping in view the ease of implementation and computational efficiency, we also present a formulation of non-equilibrium finite temperature QC based on the quasi-harmonic approximation. It also serves to establish a connection between the *max-ent* scheme and the formal asymptotics method described in the next chapter. As mentioned earlier, we start with an incremental joint potential given in Eq. (3.42). Since the mean field parameter $\omega(\boldsymbol{l})$ associated with each atom is computed as the arithmetic average of the atom's frequencies,

$$\omega^2(\boldsymbol{l}) = \frac{1}{3}\,\mathrm{Tr}\,\mathrm{K}(\boldsymbol{l})\,, \tag{3.57}$$

the incremental variational problem in eq. (3.44) reduces to

$$\inf_{\bar{\boldsymbol{q}}_{n+1}} \inf_{\{S_{n+1}\}} \sup_{\{T_{n+1}\}} \Phi_n[\{\bar{\boldsymbol{q}}_{n+1}\}, \{T_{n+1}\}, \{S_{n+1}\}]\,. \tag{3.58}$$

Since Φ_n does not involve any gradients of entropy, the minimization with respect to S_{n+1} can be effected atom by atom to yield

$$S_{n+1}(\boldsymbol{l}) = 3k_B - \frac{1}{N}k_B \log N! + 3k_B \log \frac{2\pi}{h} + 3k_B \log k_B T_{n+1}(\boldsymbol{l}) - \frac{3}{2}k_B \log\left[\frac{1}{3}\,\mathrm{Tr}\,\mathrm{K}_{n+1}(\boldsymbol{l})\right]. \tag{3.59}$$

We note that the local stiffness matrix, $\mathrm{K}_{n+1}(\boldsymbol{l})$, is computed on the deformed configuration and hence depends on the local deformation,

$$\mathrm{K}_{n+1}(\boldsymbol{l}) = \mathrm{K}\left(\bar{\boldsymbol{q}}_{n+1}, \boldsymbol{l}\right).$$

However, we shall omit the explicit dependence on $\bar{\boldsymbol{q}}$ for economy of notation. As before, we introduce a new variable, v_{n+1}, defined in Eq. (3.45a). Finally, we take variations with respect to the nodal variables, $\bar{\boldsymbol{q}}_{n+1}(\boldsymbol{l}_h)$ and $v_{n+1}(\boldsymbol{l}_h)$, and enforce stationarity of the incremental potential. This yields the equilibrium equations and the energy balance equation

$$\sum_{\boldsymbol{l}'_h \in \mathscr{L}_h} n_h(\boldsymbol{l}'_h) \left[\sum_{\boldsymbol{l} \in \mathscr{C}(\boldsymbol{l}'_h)} \boldsymbol{f}(\boldsymbol{l}) \varphi(\boldsymbol{l}|\boldsymbol{l}_h) \right] = 0 \tag{3.60a}$$

$$\begin{aligned} &- \sum_{\boldsymbol{l}'_h \in \mathscr{L}} n_h(\boldsymbol{l}'_h) \left[\sum_{\boldsymbol{l} \in \mathscr{C}(\boldsymbol{l}'_h)} 3k_B \left(v_{n+1}(\boldsymbol{l}) - \frac{1}{2} \log \frac{\mathrm{TrK}_{n+1}(\boldsymbol{l})}{\mathrm{TrK}_n(\boldsymbol{l})} \right) T_n(\boldsymbol{l}) \exp[v_{n+1}(\boldsymbol{l})] \, \varphi(l|l_h) \right] \\ &- \int_B \kappa \, \triangle t \big[\mathrm{Grad} T_n(\boldsymbol{X}) + T_n(\boldsymbol{X}) \mathrm{Grad} v_{n+1}(\boldsymbol{X}) \big] \exp[v_{n+1}(\boldsymbol{X})] \mathrm{Grad} \varphi(\boldsymbol{X}|l_h) \boldsymbol{d}V = 0 \,, \end{aligned} \tag{3.60b}$$

where

$$\boldsymbol{f}(\boldsymbol{l}) = \frac{\partial V_{n+1}}{\partial \bar{\boldsymbol{q}}_{n+1}(\boldsymbol{l})} + \frac{3}{2} k_B \sum_{\boldsymbol{l}'} \left[\frac{T_{n+1}(\boldsymbol{l}')}{\mathrm{TrK}_{n+1}(\boldsymbol{l}')} \frac{\partial}{\partial \bar{\boldsymbol{q}}_{n+1}(\boldsymbol{l})} \mathrm{TrK}_{n+1}(\boldsymbol{l}') \right] . \tag{3.61}$$

The summation is performed over all the atoms, denoted by $\boldsymbol{l}'$, in the neighborhood of the atom $\boldsymbol{l}$. The detailed calculation of these derivatives for some interatomic potentials are presented in Appendices A.1, A.2, and A.3. Using Eq. (3.59) for the local entropy, the change in entropy required in Eq. (3.60b) is simplified to

$$S_{n+1}(\boldsymbol{l}) - S_n(\boldsymbol{l}) = 3k_B \left[\log \frac{T_{n+1}(\boldsymbol{l})}{T_n(\boldsymbol{l})} - \frac{1}{2} \log \frac{\mathrm{TrK}_{n+1}(\boldsymbol{l})}{\mathrm{TrK}_n(\boldsymbol{l})} \right] . \tag{3.62}$$

Under adiabatic conditions, i.e., when $\triangle t \to 0$, the diffusion term in eq. (3.60b) vanishes. As a result, the heat equation can be solved analytically in the atomistic region and yields

$$T_{n+1}(\boldsymbol{l}) = T_n(\boldsymbol{l})\sqrt{\frac{\mathrm{TrK}_{n+1}(\boldsymbol{l})}{\mathrm{TrK}_n(\boldsymbol{l})}}\,. \tag{3.63}$$

It bears emphasis that this expression for the evolution of temperature in the region with full atomistic resolution is identical to that derived using the formal asymptotics approach. This method shall be discussed in detail in Chapter 4. The connection may be made clear by rewriting Eq. (3.63) as

$$\frac{k_B T_{n+1}(\boldsymbol{l})}{\sqrt{\mathrm{TrK}_{n+1}(\boldsymbol{l})}} = \frac{k_B T_n(\boldsymbol{l})}{\sqrt{\mathrm{TrK}_n(\boldsymbol{l})}} = \frac{k_B T_0(\boldsymbol{l})}{\sqrt{\mathrm{TrK}_0(\boldsymbol{l})}}\,, \tag{3.64}$$

where the subscript 0 denotes the undeformed configuration of the crystal and the initial temperature profile. This implies

$$T_{n+1}(\boldsymbol{l}) = T_0(\boldsymbol{l})\sqrt{\frac{\mathrm{TrK}_{n+1}(\boldsymbol{l})}{\mathrm{TrK}_0(\boldsymbol{l})}}\,, \tag{3.65}$$

which is the same as Eq. (4.68). Finally, substituting Eq. (3.65) in Eq. (3.61), we obtain

$$\boldsymbol{f}(\boldsymbol{l}) = \frac{\partial V_{n+1}}{\partial \bar{\boldsymbol{q}}_{n+1}(\boldsymbol{l})} + \frac{3\,k_B}{2}\sum_{\boldsymbol{l}'\in\mathscr{L}}\left[\frac{T_0(\boldsymbol{l})}{\sqrt{\mathrm{TrK}_{n+1}(\boldsymbol{l})\mathrm{TrK}_0(\boldsymbol{l})}}\frac{\partial}{\partial \bar{\boldsymbol{q}}_{n+1}(\boldsymbol{l})}\mathrm{TrK}_{n+1}(\boldsymbol{l}')\right]. \tag{3.66}$$

Comparing this with Eq. (4.67) from Chapter 4, we realize that the expression for the forces also become identical for the two methods. Therefore, we establish that under adiabatic conditions the formal asymptotics approach and the *max-ent* approach with the local quasi-harmonic approximation become identical when full atomistic resolution is achieved.

Chapter 4

Coarse-graining by formal asymptotics

As described in Chapter 1, the problem of ascertaining the thermodynamic behavior of materials as an averaged effect of the micro-scale fluctuations at finite temperature involves multiple scales in time. In this chapter, we propose another method for averaging out these thermal degrees of freedom in order to obtain a temperature-dependent potential on the continuum scale. It is based on the assumption that there exists a strict separation of scales between the time scale of the atomic fluctuations and that of the thermodynamic processes such as thermal expansion and heat conduction. The basic idea is to consider the macroscopic deformation of the system as quasistatic and regard the thermal oscillations of the atoms as perturbations about this slow trajectory. Treating these rapid oscillations with perturbation theory yields the desired thermodynamic potential. The problem of determining the stable equilibrium configurations of the system can then be stated as a problem of finding the *local* minima of this effective macroscopic energy.

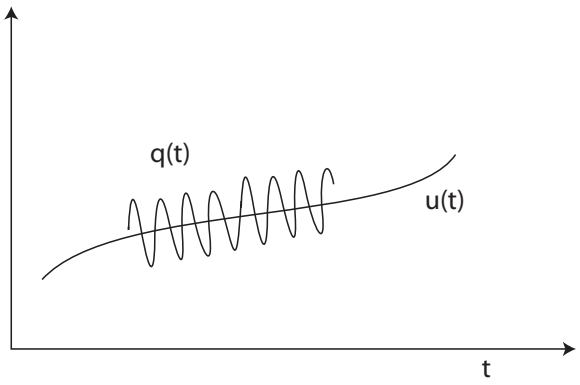

Figure 4.1: A schematic representation of the microscopic and the macroscopic degrees of freedom.

4.1 Variational formulation

We consider a system with configuration space Y × X. The states $(\boldsymbol{q}, \boldsymbol{u}) \in$ Y × X of the system consist of macroscopic variables $\boldsymbol{u}$ and microscopic variables $\boldsymbol{q}$. We assume that the time scales of the variables are well-separated, as illustrated in Figure 4.1. That is,

$$\frac{\tau_u}{\tau_q} \gg 1\,, \tag{4.1}$$

where τ_u and τ_q are the average time-periods of $\boldsymbol{u}$ and $\boldsymbol{q}$, respectively. For the sake of illustration, we consider a crystal at finite temperature with N atoms arranged in a Bravais lattice, $\mathscr{L}$. Without loss of generality, we shall consider a monatomic crystal. Using the notation from Chapter 3, we denote the lattice coordinates of individual atoms by $\boldsymbol{l} \in \mathscr{L} \subset Z^d$, d being the dimension of space. As in Chapter 2, we normalize $\boldsymbol{u}$ and $\boldsymbol{q}$ with the mass of each atom:

$$\boldsymbol{q}(\boldsymbol{l}) \to \frac{1}{\sqrt{m}}\,\boldsymbol{q}(\boldsymbol{l})\;,\;\; \boldsymbol{u}(\boldsymbol{l}) \to \frac{1}{\sqrt{m}}\,\boldsymbol{u}(\boldsymbol{l})\,. \tag{4.2}$$

For notational convenience, $\boldsymbol{u}$ or $\boldsymbol{q}$ shall represent arrays of all the atomic displacements whereas $\boldsymbol{u}(\boldsymbol{l})$ or $\boldsymbol{q}(\boldsymbol{l})$ shall refer to the corresponding displacement of atom $\boldsymbol{l}$. The separation of scales then allows decomposition of the displacement of each atom into two components,

$$\boldsymbol{u}(\boldsymbol{l}) + \boldsymbol{q}(\boldsymbol{l})\,, \tag{4.3}$$

where $\boldsymbol{u}(\boldsymbol{l})$ follows the macroscopic deformation of the crystal, and $\boldsymbol{q}(\boldsymbol{l})$ is the thermal oscillation of the atom. In this case,

$$\mathrm{X} \equiv \mathrm{Y} \equiv \mathbb{R}^{Nd}\,. \tag{4.4}$$

Our aim is to derive an effective energy of the system, $E(\boldsymbol{u})$, accounting for the effect of the micro-scale fluctuations. To this end, we consider the Hamiltonian of the system,

$$H(\boldsymbol{p}, \boldsymbol{q}, \boldsymbol{u}) = \frac{1}{2} \sum_{\boldsymbol{l} \in \mathscr{L}} |\boldsymbol{p}(\boldsymbol{l})|^2 + V(\boldsymbol{u}, \boldsymbol{q})\,, \tag{4.5}$$

where $\boldsymbol{p}(\boldsymbol{l}) = \dot{\boldsymbol{q}}(\boldsymbol{l})$ is the momentum associated with $\boldsymbol{q}(\boldsymbol{l})$ in the mass-reduced coordinates, and $V(\boldsymbol{u}, \boldsymbol{q})$ is the potential energy of the system expressible through the use of empirical interatomic potentials. We note that the inertial term due to $\boldsymbol{u}$ is neglected since $\boldsymbol{u}$ is quasistatic. According to statistical thermodynamics, the internal energy of the system is defined as the phase average of the Hamiltonian [41]. Since we are interested in studying the system in the thermodynamic limit (i.e., as $N \to \infty$), we shall assume ergodicity to express the internal energy as a time average:

$$E(\boldsymbol{u}) = \lim_{T \to \infty} \frac{1}{T} \int_0^T H\big(\boldsymbol{p}(t), \boldsymbol{q}(t), \boldsymbol{u}(t)\big)\, dt\,. \tag{4.6}$$

The energy is expressed as a function $E(\boldsymbol{u})$ based on the *ansatz* that the fluctuations satisfy, and hence can be determined from, their Euler-Lagrange equations:

$$\ddot{\boldsymbol{q}} + \frac{\partial V}{\partial \boldsymbol{q}}\big(\boldsymbol{q}, \boldsymbol{u}\big) = 0\,. \tag{4.7}$$

We now wish to obtain closed-form, albeit approximate, solutions for $\boldsymbol{q}$ in terms of $\boldsymbol{u}$ by the use of perturbation theory. Before treating the problem with perturbation analysis, we make the inherent separation of temporal scales explicit by introducing a sequence $(\boldsymbol{u}_\epsilon) \in \mathrm{X}$:

$$\boldsymbol{u}_\epsilon(t) = \boldsymbol{u}(\epsilon t)\ ;\ \ \epsilon \to 0\,. \tag{4.8}$$

For fixed $\boldsymbol{u}$, we consider a sequence of functionals

$$E_\epsilon(\boldsymbol{u}) = \frac{\epsilon}{b}\int_0^{b/\epsilon} H\big(\boldsymbol{p}_\epsilon(t), \boldsymbol{q}_\epsilon(t), \boldsymbol{u}_\epsilon(t)\big)dt \tag{4.9a}$$

$$\text{with}\quad \ddot{\boldsymbol{q}}_\epsilon + \frac{\partial V}{\partial \boldsymbol{q}}\big(\boldsymbol{q}_\epsilon, \boldsymbol{u}_\epsilon\big) = 0\,, \tag{4.9b}$$

where we have replaced the time interval $[0, T]$ by $[0, \frac{b}{\epsilon}]$ with $\epsilon \to 0$ for the sake of simplicity. We wish to ascertain the behavior of the system as $\epsilon \to 0$. To this end, we first obtain the solution to Eq. (4.9b) by using perturbation theory, as described in the following section. Substituting this approximate solution in Eq. (4.9a) and taking the limit $\epsilon \to 0$ yields the pointwise limit that we seek:

$$E(\boldsymbol{u}) = \lim_{\epsilon \to 0} E_\epsilon(\boldsymbol{u})\,. \tag{4.10}$$

4.1.1 The WKB method

The WKB method, which we shall employ to solve Eq. (4.9b), is a singular perturbation method for obtaining approximate global solutions to *linear* differential equations whose highest derivative is multiplied by a small parameter, ϵ. To reduce Eq. (4.9b) to such form, we apply the following change of variables:

$$\tau = \epsilon t \,. \tag{4.11}$$

Since ϵ is a small parameter, τ denotes a long time scale with respect to t. This yields

$$\epsilon^2 \frac{\partial^2 \boldsymbol{q}_\epsilon}{\partial \tau^2}(\tau) + \frac{\partial V}{\partial \boldsymbol{q}}(\boldsymbol{q}_\epsilon(\tau), \boldsymbol{u}(\tau)) = 0 \,. \tag{4.12}$$

One of the limitations of the WKB approach is that it can be applied only to systems of linear ODEs. This requires linearization of the equations of motion for $\boldsymbol{q}$. Hence, we assume in addition that V possesses sufficient smoothness, i.e., $V \in C^2$. Regarding $\boldsymbol{q}$ as perturbations about the macroscopic equilibrium configuration, the second order Taylor expansion of the potential energy about $\boldsymbol{u}$ yields the quasi-harmonic approximation

$$V(\boldsymbol{q}_\epsilon, \boldsymbol{u}) \approx V(\boldsymbol{u}) + \frac{1}{2} \boldsymbol{q}_\epsilon^{\mathrm{T}} \mathrm{K}(\boldsymbol{u}) \boldsymbol{q}_\epsilon \,, \tag{4.13}$$

where

$$\mathrm{K}(\boldsymbol{u}) = \left. \frac{\partial^2 V}{\partial \boldsymbol{q}^2} \right|_{\boldsymbol{q}=0} \tag{4.14}$$

is the $Nd \times Nd$ stiffness matrix of the system. The superscript T denotes a transpose. The first order term in the Taylor series expansion is zero since the system is in equilibrium. We

also remark that the quasi-harmonic approximation differs from a strict harmonic approximation in that the latter is derived by expanding the energy about the undeformed equilibrium configuration and, consequently, the dynamical matrix, K, is a constant. Substituting Eq. (4.13) in Eq. (4.9b) would give us a system of Nd linear ordinary differential equations. However, we seek to reduce the ensuing eigenvalue problem of order Nd and thereby improve the computational efficiency of the method by appealing to the *local* quasi-harmonic approximation described in section 2.5.2. This yields

$$\frac{1}{2}\boldsymbol{q}_\epsilon^{\mathrm{T}}\,\mathrm{K}(\boldsymbol{u})\,\boldsymbol{q}_\epsilon \approx \frac{1}{2}\sum_{\boldsymbol{l}\in\mathscr{L}}\boldsymbol{q}_\epsilon^{\mathrm{T}}(\boldsymbol{l})\,\mathrm{K}(\boldsymbol{u},\boldsymbol{l})\,\boldsymbol{q}_\epsilon(\boldsymbol{l})\,, \tag{4.15}$$

where $\mathrm{K}(\boldsymbol{u},\boldsymbol{l})$ is the $d\times d$ dynamical matrix associated with the atom $\boldsymbol{l}$. We note that although we neglect the coupling of vibrations of different atoms, the coupling of the macroscopic behavior of atoms is retained through the nonlinear dependence of the local stiffness matrices on the entire macroscopic displacement array, $\boldsymbol{u}$. The local quasi-harmonic model has been proposed in the work of LeSar and coworkers [23], in which it is proven to be reasonably accurate to at least half the melting temperature for moderately strained crystals. Substituting Eq. (4.15) in Eq. (4.9b) yields a system of linear differential equations for each atom as follows:

$$\epsilon^2(\boldsymbol{l})\boldsymbol{q}_\epsilon''(\boldsymbol{l}) + \mathrm{K}(\boldsymbol{u},\boldsymbol{l})\,\boldsymbol{q}_\epsilon(\boldsymbol{l}) = 0\,;\ \ \forall\,\boldsymbol{l}\in\mathscr{L}\,, \tag{4.16}$$

where $'$ denotes differentiation with respect to τ. Since $\mathrm{K}(\boldsymbol{u},\boldsymbol{l})$ is real, positive-definite, and symmetric, there exist d real eigenvalues, which we represent by $\omega_i^2(\boldsymbol{l})$ and corresponding eigenvectors, which we denote by $\boldsymbol{v}_i(\boldsymbol{l})$. The uncoupled modal equations have the form

$$\epsilon^2 Q_i''(\boldsymbol{l}) + \omega_i^2(\boldsymbol{u},\boldsymbol{l})\,Q_i(\boldsymbol{l}) = 0\,;\ \ i=1,\ldots,d\,. \tag{4.17}$$

Q_i are the coordinates in the principal directions associated with the atom $\boldsymbol{l}$ and defined as

$$\boldsymbol{q}_\epsilon(\boldsymbol{l}) = \sum_{i=1}^{d} \boldsymbol{v}_i(\boldsymbol{l})\, Q_i(\boldsymbol{l})\,. \tag{4.18}$$

The frequencies and the normalized mode shapes satisfy,

$$\boldsymbol{v}_i^{\mathrm{T}}\, \mathrm{K}(\boldsymbol{u},\boldsymbol{l})\, \boldsymbol{v}_i = \omega_i^2(\boldsymbol{u},\boldsymbol{l})\,, \quad \boldsymbol{v}_i^{\mathrm{T}}\, \boldsymbol{v}_j = \delta_{ij}\,, \quad i,j = 1,\ldots,d\,, \tag{4.19}$$

δ_{ij} being the Kronecker delta function. To each of these resulting equations (4.17), we apply the WKB method, as described in Appendix C, and solve for $Q_i(\boldsymbol{l})$. Using Eq. (4.18), we obtain the desired approximate expression for $\boldsymbol{q}_\epsilon(\boldsymbol{l})$ and the corresponding velocities:

$$\boldsymbol{q}_\epsilon(\boldsymbol{l},\tau) = \sum_j \frac{1}{\sqrt{\omega_j(\boldsymbol{u})}} \boldsymbol{v}_j(\boldsymbol{u}) \left\{ A_j \sin\left(\frac{1}{\epsilon}\int^\tau \omega_j(s)ds\right) + B_j \cos\left(\frac{1}{\epsilon}\int^\tau \omega_j(s)ds\right)\right\} \tag{4.20a}$$

$$\frac{d\boldsymbol{q}_\epsilon}{d\tau}(\boldsymbol{l},\tau) = \frac{1}{\epsilon}\sum_j \sqrt{\omega_j(\boldsymbol{u})} v_j(\boldsymbol{u}) \left\{ A_j \cos\left(\frac{1}{\epsilon}\int^\tau \omega_j(s)ds\right) - B_j \sin\left(\frac{1}{\epsilon}\int^\tau \omega_j(s)ds\right)\right\}. \tag{4.20b}$$

A_i and B_i are constants of integration that can be evaluated from initial conditions.

4.1.2 Effective temperature-dependent energy

We now derive the effective energy of the system. We recall the family of energy functionals defined in Eq. (4.9a) and introduce the change of time variable from t to $\tau = \epsilon t$:

$$E_\epsilon(\boldsymbol{u}) = \frac{1}{b}\int_0^b H\big(\boldsymbol{p}_\epsilon(\tau), \boldsymbol{q}_\epsilon(\tau), \boldsymbol{u}(\tau)\big) d\tau\,. \tag{4.21}$$

Under the quasi-harmonic approximation, the Hamiltonian in Eq. (4.5) has the form

$$H = \frac{1}{2}\sum_{\boldsymbol{l}\in\mathscr{L}} |\boldsymbol{p}_\epsilon(\boldsymbol{l})|^2 + V(\boldsymbol{u}(\tau)) + \frac{1}{2}\sum_{\boldsymbol{l}\in\mathscr{L}} \boldsymbol{q}_\epsilon^{\mathrm{T}}(\boldsymbol{l})\,\mathrm{K}(\boldsymbol{u},\boldsymbol{l})\,\boldsymbol{q}_\epsilon(\boldsymbol{l})\,. \tag{4.22}$$

Using the relation

$$\boldsymbol{p}_\epsilon(\boldsymbol{l}) = \dot{\boldsymbol{q}}_\epsilon(\boldsymbol{l}) = \epsilon\,\boldsymbol{q}'_\epsilon(\boldsymbol{l}),\ \ \forall\ \boldsymbol{l}\in\mathscr{L} \tag{4.23}$$

and substituting the solutions given in equations (4.20a-4.20b) in the expression (4.22) simplifies the Hamiltonian to

$$H = V(\boldsymbol{u}) + \frac{1}{2}\sum_{\boldsymbol{l}\in\mathscr{L}}\sum_{i=1}^{d} \omega_i(\boldsymbol{u},\boldsymbol{l}) D_i^2(\boldsymbol{l}) \tag{4.24}$$

with

$$D_i^2(\boldsymbol{l}) = A_i^2(\boldsymbol{l}) + B_i^2(\boldsymbol{l})\,. \tag{4.25}$$

Finally, using Eq. (4.24) in the expression (4.21) for the energy, we have

$$E_\epsilon(\boldsymbol{u}) = \frac{1}{b-a}\int_a^b \left[V(\boldsymbol{u}) + \frac{1}{2}\sum_{\boldsymbol{l}\in\mathscr{L}}\sum_{i=1}^{d} \omega_i(\boldsymbol{u},\boldsymbol{l}) D_i^2(\boldsymbol{l})\right] d\tau\,. \tag{4.26}$$

We observe that $E_\epsilon(\boldsymbol{u})$ is independent of ϵ. This implies that the right hand side of Eq. (4.26) is indeed the limit $E(\boldsymbol{u})$, and we have

$$E_\epsilon = E$$

for every $\boldsymbol{u}\in\mathrm{X}$ and for $\epsilon\to 0$. Furthermore, we emphasize that since $\boldsymbol{u}$ is a quasistatic deformation, τ simply serves as an index for a continuous sequence of states at uniform

thermodynamic equilibrium. Interpreted as time, τ represents an arbitrary slow process on the macroscopic time scale. Hence, we can rewrite the internal energy as

$$E(\boldsymbol{u}) = V(\boldsymbol{u}) + \frac{1}{2}\sum_{\boldsymbol{l}\in\mathscr{L}}\sum_{i=1}^{d}\omega_i(\boldsymbol{u},\boldsymbol{l})D_i^2(\boldsymbol{l})\,. \tag{4.27}$$

Determination of $D_i(\boldsymbol{l})$

In molecular dynamics, the equilibrium temperature is prescribed and maintained through the atomic velocities. This is based on the equipartition of energy described earlier, which states that for a system in thermodynamic equilibrium, every quadratic term in the Hamiltonian contributes $k_BT/2$ to the internal energy, T being the equilibrium temperature. We follow the same procedure in order to express the dependence of $E(\boldsymbol{u})$ on the local temperature through the $D_i(\boldsymbol{l})$. To this end, we introduce a local temperature, $T(\boldsymbol{l})$, associated with each atom. We also denote by $\boldsymbol{q}_0(\boldsymbol{l})$ and $\mathbf{v}_0(\boldsymbol{l})$ the initial positions and the initial velocities, respectively, of the atom $\boldsymbol{l}$. We let the initial configuration of the system be an equilibrium state at zero temperature.

$$\boldsymbol{u}(\boldsymbol{l})|_{\tau=0} = \boldsymbol{u}_0(\boldsymbol{l}) \tag{4.28a}$$

$$\boldsymbol{q}_\epsilon(\boldsymbol{l})|_{\tau=0} = \boldsymbol{q}_0(\boldsymbol{l}) \tag{4.28b}$$

$$\dot{\boldsymbol{q}}_\epsilon(\boldsymbol{l})|_{\tau=0} = \epsilon\,\boldsymbol{q}'_\epsilon(\boldsymbol{l})|_{\tau=0} = \mathbf{v}_0(\boldsymbol{l}) \tag{4.28c}$$

To determine $A_i(\boldsymbol{l})$ and $B_i(\boldsymbol{l})$, we substitute the above in equations (4.20a - 4.20b) at $\tau = 0$.

Taking the dot product of both the equations with the vector $M\boldsymbol{v}_i(\boldsymbol{l})$ yields

$$B_i(\boldsymbol{l}) = \sqrt{\omega_i(\boldsymbol{u}_0,\boldsymbol{l})}\ \left[\boldsymbol{v}_i^{\mathrm{T}}(\boldsymbol{u}_0,\boldsymbol{l})\,\boldsymbol{q}_0(\boldsymbol{l})\right]\ ,\ \ i=1,\dots d \tag{4.29a}$$

$$A_i(\boldsymbol{l}) = \frac{1}{\sqrt{\omega_i(\boldsymbol{u}_0,\boldsymbol{l})}}\ \left[\boldsymbol{v}_i^{\mathrm{T}}(\boldsymbol{u}_0,\boldsymbol{l})\,\mathbf{v}_0(\boldsymbol{l})\right]\ ,\ \ i=1,\dots d\,, \tag{4.29b}$$

where we have exploited the orthogonality of the eigenvectors $\boldsymbol{v}(\boldsymbol{l})$. Writing $\boldsymbol{v}_0(\boldsymbol{l})$ and $\boldsymbol{q}_0(\boldsymbol{l})$ in the principal coordinates,

$$\mathbf{v}_0(\boldsymbol{l}) = \sum_{i=1}^{d} \boldsymbol{v}_i(\boldsymbol{u}_0,\boldsymbol{l})V_i(\boldsymbol{l})\,,\ \ \boldsymbol{q}_0(\boldsymbol{l}) = \sum_{i=1}^{d} \boldsymbol{v}_i(\boldsymbol{u}_0,\boldsymbol{l})Q_i(\boldsymbol{l})\,, \tag{4.30}$$

we have

$$D_i^2(\boldsymbol{l}) = \frac{1}{\omega_i(\boldsymbol{u}_0,\boldsymbol{l})}[V_i^2(\boldsymbol{l}) + \omega_i^2(\boldsymbol{u}_0,\boldsymbol{l})Q_i^2(\boldsymbol{l})]\,. \tag{4.31}$$

Assuming local equilibrium, we appeal again to the equipartition theorem to yield

$$\frac{1}{2}[V_i^2(\boldsymbol{l}) + \omega_i^2(\boldsymbol{u}_0,\boldsymbol{l})Q_i^2(\boldsymbol{l})] = k_B T_0(\boldsymbol{l})\,,\ i=1,\dots d\,, \tag{4.32}$$

which in turn gives

$$D_i^2(\boldsymbol{l}) = 2\frac{k_B T_0(\boldsymbol{l})}{\omega_i(\boldsymbol{u}_0,\boldsymbol{l})}\,. \tag{4.33}$$

$T_0(\boldsymbol{l})$ is the initial prescribed temperature. Thus, the internal energy of the system, given in (4.27), becomes

$$E(\boldsymbol{u}) = V(\boldsymbol{u}) + \sum_{\boldsymbol{l}\in\mathscr{L}} k_B T_0(\boldsymbol{l}) \sum_{i=1}^{d} \frac{\omega_i(\boldsymbol{u},\boldsymbol{l})}{\omega_i(\boldsymbol{u}_0,\boldsymbol{l})}\,. \tag{4.34}$$

An important remark in place here is that $E(\boldsymbol{u})$ is the internal energy of a system which need not be in thermal equilibrium. In other words, the system may have different temperatures

in different regions and should only satisfy the local thermal equilibrium hypothesis which enables us to define a local temperature, $T(\boldsymbol{l})$.

4.2 Adiabatic invariance

In this section, we seek to understand some properties of the effective energy derived in the previous section based on its structure as given in Eq. (4.34). However, before we proceed, it is instructive to understand our results by comparing with those obtained by other similar studies. For this purpose, we recall that the effective Hamiltonian obtained by formal asymptotics without the *local* quasi-harmonic approximation (i.e., by using the $Nd \times Nd$ global stiffness matrix of the system) is

$$H(\boldsymbol{u}) = V(\boldsymbol{u}) + \frac{1}{2}\sum_{i=1}^{Nd} D_i^2 \omega_i(\boldsymbol{u})\,. \tag{4.35}$$

This result is identical to the effective potential derived in the work of Bornemann [3] on the homogenization in time of singularly perturbed mechanical systems. A model problem used in this study is a conservative dynamical system, with the displacement having a very fast and a slow component and a constraining potential having a quadratic form. Unlike our approach, this work uses the method of weak convergence in order to determine a homogenized potential energy for the limiting mechanical system on the continuum scale. For details of the analysis, we refer the reader to Chapters 1 and 2 of [3].

We now show that the internal energy given by Eq. (4.34) describes a system undergoing an adiabatic process and, hence, the problem of finding metastable equilibrium configurations

of the system can be enunciated as a minimization problem:

$$\inf_{\boldsymbol{u}\in \mathrm{X}} E(\boldsymbol{u})\,. \tag{4.36}$$

We refer to the work of Bornemann [3] and present some physical arguments in support of our claim. We first observe that the internal energy in Eq. (4.34) is a function of only one state variable, which is the deformation of the system. Thus, the only two ways of changing the total energy of the system are by either prescribing a different initial temperature or by deforming it. This implies that the model based on the internal energy of the system does not allow for heat transport between atoms and their ambience during a process. Hence, we can conclude that the minimization problem stated in Eq. (4.36) describes a system subjected to mechanical deformation under adiabatic conditions. This is in agreement with classical thermodynamics in that the isentropic processes are modelled by minimizing the internal energy. In the absence of entropy sources or sinks within the system, adiabatic and isentropic conditions are equivalent.

This is also verified by the following calculations relating the current and the initial temperature distribution within the system. For any system, the internal energy calculated using the harmonic approximation comprises of the interatomic potential $V(\boldsymbol{u})$, which may be anharmonic, and the energy contained in the thermal oscillations of the atoms, which is harmonic by assumption. If the system is in local thermal equilibrium,

$$E(\boldsymbol{u}) = V(\boldsymbol{u}) + \sum_{\boldsymbol{l}\in\mathscr{L}} d\, k_B T(\boldsymbol{l})\,, \tag{4.37}$$

$T(\boldsymbol{l})$ being the current local temperature. Comparing Eq. (4.37) and Eq. (4.34), we have

$$d\,T(\boldsymbol{l}) = T_0(\boldsymbol{l}) \sum_{i=1}^{d} \frac{\omega_i(\boldsymbol{u}, \boldsymbol{l})}{\omega_i(\boldsymbol{u}_0, \boldsymbol{l})}\,. \tag{4.38}$$

Since the equipartition of energy implies equal distribution of the energy among all modes, we get

$$T(\boldsymbol{l}) = T_0(\boldsymbol{l}) \frac{\omega_i(\boldsymbol{u}, \boldsymbol{l})}{\omega_i(\boldsymbol{u}_0, \boldsymbol{l})}\,,\ \forall i = 1, \ldots, d\,. \tag{4.39}$$

It is evident that the temperature of the system changes only when there is a change in the mechanical configuration of the system. Therefore, Eq. (4.39) describes the evolution of local temperature during an adiabatic process. This relation can also be derived rigorously based on the adiabatic invariance of the normal action proved in [3]. For a dynamical system whose effective potential is given by Eq. (4.35), the normal action is defined as the energy-frequency ratio,

$$\theta_\epsilon^i = \frac{E_\epsilon^i}{\omega_i(\boldsymbol{u})}\,. \tag{4.40}$$

E_ϵ^i is the energy of the i^{th} mode. By way of weak convergence, it is shown that

$$\theta_\epsilon^i \rightharpoonup \theta_0^i = \text{const}\,. \tag{4.41}$$

This is known as the adiabatic invariance of the normal action. Applying this to our problem, we obtain the local relation

$$\frac{k_B T(\boldsymbol{l})}{\omega_i(\boldsymbol{u}, \boldsymbol{l})} = \text{const}\,, \tag{4.42}$$

which is the same as Eq. (4.39).

4.3 Mie-Grüneisen approximation

Eq. (4.34) requires the computation of frequencies associated with each atom, which is an eigenvalue problem of order d ($d = 1, 2, 3$) with $\boldsymbol{u}$ fixed at the current macroscopic configuration. Although the eigenvalue problem is not computationally expensive, the computational burden increases for systems in 3 dimensions with a very large number of atoms. Moreover, we are interested in the solutions of the minimization problem

$$\inf_{\boldsymbol{u}\in \mathrm{X}} E(\boldsymbol{u})\,, \tag{4.43}$$

where $E(\boldsymbol{u})$ is furnished by (4.34). We observe that the computation of forces involves derivatives of the frequencies with respect to $\boldsymbol{u}$, which can be achieved only by numerical differentiation. We circumvent this requirement in two ways. One way is by stating the following claim based on the Mie-Grüneisen approximation.

Claim 4.3.1. *Consider a system in local thermal equilibrium with $\omega_i(\boldsymbol{u}, \boldsymbol{l})$ being the phonon frequencies associated with atom $\boldsymbol{l}$. Then, under the Mie-Grüneisen approximation applied locally,*

$$\frac{\omega_i(\boldsymbol{u}, \boldsymbol{l})}{\omega_i(\boldsymbol{u}_0, \boldsymbol{l})} = const,\ i = 1, \ldots, d\,. \tag{4.44}$$

Proof. The Mie-Grüneisen approximation states that, for a system in thermal equilibrium, the Grüneisen parameter, defined as

$$\gamma(V) = -\left(\frac{\partial \ln \omega_i}{\partial \ln V}\right)_T\,,\ i = 1, \ldots, Nd\,, \tag{4.45}$$

is the same for all modes. The implication of this approximation is that the phonon frequencies are not functions of the equilibrium temperature explicitly but depend on it through

the volume V. As we noted earlier, the system under consideration needs only to be in local thermal equilibrium. Hence, we apply the Mie-Grüneisen approximation locally, the Grüneisen parameter for each atom,

$$\gamma(\boldsymbol{l}) = -\left(\frac{\partial \ln \omega_i(\boldsymbol{u},\boldsymbol{l})}{\partial \ln V}\right)_{\boldsymbol{T}} \;,\; i = 1,\ldots,d\,, \tag{4.46}$$

being the same for the d modes of the atom. $\boldsymbol{T}$ represents an array of temperatures of all atoms. Thus, we do not impose γ to be the same for all the atoms, although it may be same for atoms experiencing identical environments. Eq. (4.46) can be simplified to

$$\gamma(\boldsymbol{l}) = -\left(\frac{V}{\omega_i(\boldsymbol{u},\boldsymbol{l})}\frac{\partial \omega_i(\boldsymbol{u},\boldsymbol{l})}{\partial \boldsymbol{u}}\cdot\frac{\partial \boldsymbol{u}}{\partial V}\right)_{\boldsymbol{T}}\,. \tag{4.47}$$

By defining a new function $g_1(\boldsymbol{u},\boldsymbol{l})$, we rewrite the above equation as

$$\frac{\partial \omega_i(\boldsymbol{u},\boldsymbol{l})}{\partial \boldsymbol{u}} = -\frac{\gamma(\boldsymbol{l})}{V}\frac{\partial V}{\partial \boldsymbol{u}}\,\omega_i(\boldsymbol{u},\boldsymbol{l}) = g_1(\boldsymbol{u},\boldsymbol{l})\,\omega_i(\boldsymbol{u},\boldsymbol{l})\,. \tag{4.48}$$

At the initial equilibrium configuration, i.e., when $\boldsymbol{u} = \boldsymbol{u}_0$,

$$\gamma_0(\boldsymbol{l}) = -\left.\frac{V_0}{\omega_i(\boldsymbol{u}_0,\boldsymbol{l})}\frac{\partial \boldsymbol{u}}{\partial V}\frac{\partial \omega_i(\boldsymbol{u},\boldsymbol{l})}{\partial \boldsymbol{u}}\right|_0\,. \tag{4.49}$$

or

$$\left.\frac{\partial \omega_i(\boldsymbol{u},\boldsymbol{l})}{\partial \boldsymbol{u}}\right|_0 = g_1(\boldsymbol{u}_0,\boldsymbol{l})\,\omega_i(\boldsymbol{u}_0,\boldsymbol{l}) \tag{4.50}$$

Assuming sufficient smoothness of the function $g_1(\boldsymbol{u},\boldsymbol{l})$, we compute the higher derivatives

of the frequencies as follows:

$$\frac{\partial^2 \omega_i(\boldsymbol{u},\boldsymbol{l})}{\partial \boldsymbol{u}^2} = g_1'(\boldsymbol{u},\boldsymbol{l})\,\omega_i(\boldsymbol{u},\boldsymbol{l}) + g_1(\boldsymbol{u},\boldsymbol{l})\,\omega_i'(\boldsymbol{u},\boldsymbol{l}) \tag{4.51a}$$

$$= (g_1'(\boldsymbol{u},\boldsymbol{l}) + g_1^2(\boldsymbol{u},\boldsymbol{l}))\,\omega_i(\boldsymbol{u},\boldsymbol{l}) = g_2(\boldsymbol{u},\boldsymbol{l})\,\omega_i(\boldsymbol{u},\boldsymbol{l})\,, \tag{4.51b}$$

where the prime denotes differentiation w.r.t $\boldsymbol{u}$. Eq. (4.51b) is obtained by substituting Eq. (4.48) in Eq. (4.51a). By similar calculations, we obtain a recursive expression for the n^{th} derivative of $\omega_i(\boldsymbol{u},\boldsymbol{l})$,

$$\frac{\partial^n \omega_i(\boldsymbol{u},\boldsymbol{l})}{\partial \boldsymbol{u}^n} = g_n(\boldsymbol{u},\boldsymbol{l})\,\omega_i(\boldsymbol{u},\boldsymbol{l})\,, \tag{4.52}$$

with

$$g_n(\boldsymbol{u},\boldsymbol{l}) = g_{n-1}'(\boldsymbol{u},\boldsymbol{l}) + g_1(\boldsymbol{u},\boldsymbol{l})\,g_{n-1}(\boldsymbol{u},\boldsymbol{l})\ ,\ n \geq 2\,. \tag{4.53}$$

At the initial equilibrium configuration,

$$\left.\frac{\partial^n \omega_i(\boldsymbol{u},\boldsymbol{l})}{\partial \boldsymbol{u}^n}\right|_0 = g_n(\boldsymbol{u}_0,\boldsymbol{l})\,\omega_i(\boldsymbol{u}_0,\boldsymbol{l})\ ,\ n \geq 1\,. \tag{4.54}$$

From Eq. (4.52) we observe that all derivatives of $\omega_i(\boldsymbol{u},\boldsymbol{l})$ are linear in $\omega_i(\boldsymbol{u},\boldsymbol{l})$. Assuming sufficient smoothness of $\omega_i(\boldsymbol{u},\boldsymbol{l})$, the n^{th} order Taylor series expansion for $\omega_i(\boldsymbol{u},\boldsymbol{l})$ about the initial equilibrium state is

$$\omega_i(\boldsymbol{u},\boldsymbol{l}) = \omega_i(\boldsymbol{u}_0,\boldsymbol{l}) + \left.\frac{\partial \omega_i(\boldsymbol{u},\boldsymbol{l})}{\partial \boldsymbol{u}}\right|_0 \cdot[\boldsymbol{u}-\boldsymbol{u}_0] + \frac{1}{2}\left.\frac{\partial^2 \omega_i(\boldsymbol{u},\boldsymbol{l})}{\partial \boldsymbol{u}^2}\right|_0 [\boldsymbol{u}-\boldsymbol{u}_0]^2 + \cdots + \frac{1}{n!}\left.\frac{\partial^n \omega_i(\boldsymbol{u},\boldsymbol{l})}{\partial \boldsymbol{u}^n}\right|_0 [\boldsymbol{u}-\boldsymbol{u}_0]^n\,. \tag{4.55}$$

Dividing throughout by $\omega_i(0)$ and using the expressions for the derivatives given in (4.54),

$$\frac{\omega_i(\boldsymbol{u},\boldsymbol{l})}{\omega_i(\boldsymbol{u}_0,\boldsymbol{l})} = 1 + g_1(\boldsymbol{u}_0,\boldsymbol{l})\boldsymbol{u} + \frac{1}{2}g_2(\boldsymbol{u}_0,\boldsymbol{l})\boldsymbol{u}^2 + \cdots + \frac{1}{n!}g_n(\boldsymbol{u}_0,\boldsymbol{l})\boldsymbol{u}^n\,. \tag{4.56}$$

Since the right hand side is independent of i, Eq. (4.56) shows that under the Mie-Grüneisen approximation, all frequencies of an atom change in the same ratio. □

Another way to arrive at Eq. (4.44) is by using (4.39), derived in the previous section based on the equi-partitioning of energy. Thus, we may write

$$\frac{\omega_i(\boldsymbol{u},\boldsymbol{l})}{\omega_i(\boldsymbol{u}_0,\boldsymbol{l})} = \frac{a}{b}\,,\ \forall i = 1,\ldots,d\,, \tag{4.57}$$

where a/b is some constant. Further, using the algebraic identity

$$\frac{a}{b} = \frac{c}{d} = \frac{a+c}{b+d}\,, \tag{4.58}$$

we can write

$$\frac{\omega_i^2(\boldsymbol{u},\boldsymbol{l})}{\omega_i^2(\boldsymbol{u}_0,\boldsymbol{l})} = \frac{\sum_{i=1}^{d}\omega_i^2(\boldsymbol{u},\boldsymbol{l})}{\sum_{i=1}^{d}\omega_i^2(\boldsymbol{u}_0,\boldsymbol{l})} = \frac{\mathrm{TrK}(\boldsymbol{u},\boldsymbol{l})}{\mathrm{TrK}(\boldsymbol{u}_0,\boldsymbol{l})}\,. \tag{4.59}$$

Consequently,

$$\sum_{i=1}^{d}\frac{\omega_i(\boldsymbol{u},\boldsymbol{l})}{\omega_i(\boldsymbol{u}_0,\boldsymbol{l})} = d\frac{a}{b} = d\sqrt{\frac{\mathrm{TrK}(\boldsymbol{u},\boldsymbol{l})}{\mathrm{TrK}(\boldsymbol{u}_0,\boldsymbol{l})}}\,. \tag{4.60}$$

Thus, the internal energy attains the following form:

$$E(\boldsymbol{u}) = V(\boldsymbol{u}) + \sum_{\boldsymbol{l}\in\mathscr{L}} dk_B T_0(\boldsymbol{l})\sqrt{\frac{\mathrm{TrK}(\boldsymbol{u},\boldsymbol{l})}{\mathrm{TrK}(\boldsymbol{u}_0,\boldsymbol{l})}}\,. \tag{4.61}$$

We use this expression for the internal energy in our subsequent calculations. An advantage of using Eq. (4.61) is that we can derive analytical expressions for the trace of the stiffness matrices and hence their derivatives with respect to $\boldsymbol{u}$. The expressions for the energy, forces, local stiffness matrices, and their derivatives are derived in Appendices A.1 and A.2.

4.4 Application to the quasicontinuum method

In this final section, we review the formulation of the quasicontinuum method for finite temperature on the basis of the results of the WKB method. The basis structure of the computational scheme remains the same, as described in detail in sections 3.1 and 3.2. A major difference is that the energy functional to be minimized is defined as

$$\Phi(\boldsymbol{u}) = E(\boldsymbol{u}) + \Phi^{ext}(\boldsymbol{u})\,, \tag{4.62}$$

where the internal energy $E(\boldsymbol{u})$ is furnished by Eq. (4.61). Then, the problem of finding the set of minimizers of this energy functional may be stated as

$$\min_{\boldsymbol{u}\in X} \Phi(\boldsymbol{u})\,. \tag{4.63}$$

Proceeding according to section 3.1, we introduce the following interpolation for the macroscopic displacement field $\boldsymbol{u}$ over a carefully selected set $\mathscr{L}_h$ of $N_h < N$ representative atoms:

$$\boldsymbol{u}_h(\boldsymbol{l}) = \sum_{\boldsymbol{l}_h\in\mathscr{L}_h} \varphi(\boldsymbol{l}|\boldsymbol{l}_h)\boldsymbol{u}_h(\boldsymbol{l}_h)\,. \tag{4.64}$$

Using Eq. (4.64) in the expression for $\Phi(\boldsymbol{u})$, taking variations with respect to the nodal variables $\boldsymbol{u}_h(\boldsymbol{l}_h)$, and enforcing stationarity yields the equilibrium equations. Introducing cluster summation rules, the effective equilibrium equations are obtained as

$$\sum_{\boldsymbol{l}'_h\in\mathscr{L}_h} n_h(\boldsymbol{l}'_h)\left[\sum_{\boldsymbol{l}\in\mathscr{C}(\boldsymbol{l}'_h)} \boldsymbol{f}(\boldsymbol{l})\varphi(\boldsymbol{l}|\boldsymbol{l}_h)\right] = \boldsymbol{0}\,. \tag{4.65}$$

The force at each site $\boldsymbol{l}$ is evaluated as

$$\boldsymbol{f}(\boldsymbol{l}) = \frac{\partial \Phi}{\partial \boldsymbol{u}(\boldsymbol{l})} \tag{4.66a}$$

$$= \frac{\partial E}{\partial \boldsymbol{u}(\boldsymbol{l})} + \frac{\partial \Phi^{ext}}{\partial \boldsymbol{u}(\boldsymbol{l})} \tag{4.66b}$$

with

$$\frac{\partial E}{\partial \boldsymbol{u}(\boldsymbol{l})} = \frac{\partial V}{\partial \boldsymbol{u}(\boldsymbol{l})} + \frac{d\, k_B}{2} \sum_{\boldsymbol{l}' \in \mathscr{L}} \left[\frac{T_0(\boldsymbol{l})}{\sqrt{\mathrm{TrK}(\boldsymbol{u}_0, \boldsymbol{l}) \mathrm{TrK}(\boldsymbol{u}, \boldsymbol{l})}} \frac{\partial}{\partial \boldsymbol{u}(\boldsymbol{l})} \mathrm{TrK}(\boldsymbol{u}, \boldsymbol{l}') \right], \tag{4.67}$$

where $\boldsymbol{l}'$ denotes all the atoms in the neighborhood of atom $\boldsymbol{l}$ with a specified cutoff radius. As described in section 4.2, the solutions to Eq. (4.63) yield the equilibrium configurations of the crystal under adiabatic conditions. Furthermore, in the absence of entropy sources within the body, this is equivalent to isentropic conditions. Consequently, if the entropy of the system remains constant during a process, the temperature of the system must change, as entropy and temperature are conjugate state variables. Therefore, after determining the new equilibrium state of the crystal by solving Eq. (4.65), the new temperature distribution is obtained by evaluating the relation (4.39) at the nodes. Using the Mie–Grüneisen approximation, this relation becomes

$$T_h(\boldsymbol{l}_h) = T_0(\boldsymbol{l}_h) \sqrt{\frac{\mathrm{TrK}(\boldsymbol{u}, \boldsymbol{l}_h)}{\mathrm{TrK}(\boldsymbol{u}_0, \boldsymbol{l}_h)}}\,. \tag{4.68}$$

This concludes our discussion on the formal asymptotics approach for coarse-graining an atomistic description at finite temperature. We recall that under adiabatic conditions, this method becomes equivalent to the *max-ent* method with the quasi-harmonic approximation. For a detailed discussion, we refer to section 3.6. In the next chapter, we shall

validate this method by modelling some thermodynamic bulk properties and comparing with experimental data and molecular dynamics results. We shall also present the results for a nanoindentation test simulated under adiabatic conditions using the quasicontinuum method based on this approach.

Chapter 5

Results and validation

Chapters 2 and 4 developed a theoretical framework based on two approaches, namely the *max-ent* method and formal asymptotics, to derive averaged macroscopic energy functionals from the microscopic dynamics. In Chapter 3, we incorporated these into the quasicontinuum framework to accomplish our goal of coarse-graining an atomistic description at finite temperature. Here, we present a suit of numerical simulations that were performed using these methods followed by a discussion of the results. The purpose of the tests is two-fold. First, they serve to validate the proposed methods by comparing their results with classical theory, experimental data, and molecular dynamics results. These include simulations performed to determine some bulk properties such as the specific heat and the coefficient of thermal expansion for some materials. Second, they serve as illustrative examples that demonstrate the ability of the proposed methods to capture thermo-mechanical coupled phenomena. These include examples of adiabatic tension, heat conduction, and nanoindentation. The results presented for these tests are qualitative and open possible directions for further investigations.

The samples used in our simulations are face-centered cubic (fcc) crystals with the crystallographic orientation as shown in Figure 5.1. The tests were performed with two materials, solid argon and copper, both existing in fcc structure. It bears emphasis that the choice of

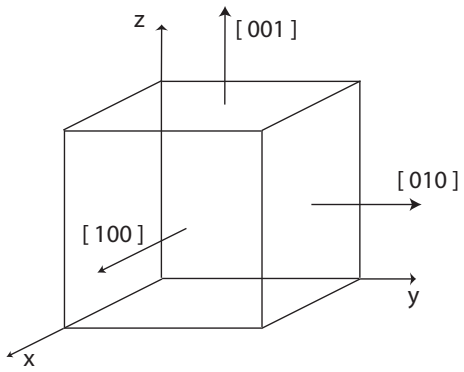

Figure 5.1: Crystallographic orientation of the test sample used in the simulations.

materials is dictated by our choice of empirical interaction potentials for fcc crystals. The proposed methods are general enough to be applied to any crystal structure and interatomic potentials.

5.1 Bulk Properties

In this section, we present the results for the specific heat and the thermal expansion coefficient for solid Ar and Cu. The Lennard-Jones pair potential is appropriate for solid Ar, whereas the potentials used for Cu involve many-body interactions. We use two such potentials for modelling copper, namely, the EAM-Johnson potential [18] and the Sutton-Chen potential [37], both of which are based on the embedded-atom method [7].

The sample used for these tests is a cube of an fcc crystal consisting of 108 atoms. Since our aim is to study bulk properties, periodic boundary conditions are applied in all directions in order to simulate an infinite crystal. As in molecular dynamics simulations [30], the periodic boundary conditions are implemented by repeating images of the original cell of 108 atoms in the three directions. Then, the neighborhood of each atom consists of either neighbors within the cell or images of atoms in the cell. This ensures that even surface atoms have

all their neighbors and that, for a perfect crystal undergoing a homogeneous deformation, every atom experiences exactly the same environment. Furthermore, since we assume the crystal to be perfect and isotropic, its physical properties should be the same everywhere and in all directions. This implies that the thermal expansion of the crystal should also be uniform when it is subjected to a uniform temperature. Simply put, the crystal should maintain its structure as a Bravais lattice even after undergoing thermal expansion. For this reason, choosing the change in lattice parameter as the only mechanical degree of freedom for the whole system should suffice. This reduces the energy minimization problem to

$$\min_{a} \Phi \,, \tag{5.1}$$

where Φ is an appropriate energy functional furnished by the *max-ent* method or the WKB method, and a is the lattice parameter in the deformed configuration. For an fcc crystal in three dimensional space, the lattice vectors $\boldsymbol{a}_i$ may be chosen as

$$\boldsymbol{a}_1 = \frac{a}{2}\begin{pmatrix} 1 \\ 0 \\ 0 \end{pmatrix}, \quad \boldsymbol{a}_2 = \frac{a}{2}\begin{pmatrix} 0 \\ 1 \\ 0 \end{pmatrix}, \text{and } \boldsymbol{a}_3 = \frac{a}{2}\begin{pmatrix} 0 \\ 0 \\ 1 \end{pmatrix}. \tag{5.2}$$

In the following sections we present our results for the thermal expansion coefficient and specific heat for the Lennard-Jones potential and the EAM-type potentials.

5.1.1 Thermal expansion

The numerical test for thermal expansion is conducted as follows. The sample is prescribed a uniform temperature T_0 and is equilibrated by solving the variational problem (5.1). The

non-linear version of the conjugate gradient method is employed to do the minimization. For the *max-ent* approach, the test is performed under isothermal conditions and hence the appropriate energy functional is the free energy, $F(\bar{q}, T_0, \{\omega\})$. Then, Eq. (5.1) may be stated as

$$\min_{a\in\mathbb{R}} \min_{\omega\in\mathbb{R}} F(a, T_0, \omega)\,, \tag{5.3}$$

where we have incorporated the fact that

$$\omega_a = \omega,\ \forall\, a = 1, \ldots, N$$

because every atom has the same environment, even in the deformed configuration. Since the approach based on formal asymptotics assumes adiabatic conditions, the minimization problem may be stated as

$$\min_{a\in\mathbb{R}} E(a, T_0)\,, \tag{5.4}$$

where $E(a, T_0)$ is the internal energy of the system. As elaborated in section 4.2, the temperature of a system undergoing an adiabatic process must change during the process. The uniform temperature of the system in the deformed configuration is evaluated as

$$T = T_0 \sqrt{\frac{\mathrm{TrK}(a, b)}{\mathrm{TrK}(a_0, b)}}\,, \tag{5.5}$$

where a and a_0 denote the current and initial lattice constants, and b denotes an atom in the crystal. This computation is performed after the system achieves equilibrium at the prescribed temperature, and this value of T is used in plotting the thermal expansion versus temperature. The coefficient of linear thermal expansion is then given by the instantaneous

slope of this curve:

$$\alpha(T) = \frac{\partial \varepsilon}{\partial T} \quad \text{where} \quad \varepsilon = \frac{a}{a_0} - 1\,. \tag{5.6}$$

We now present a discussion of our results for the thermal expansion of solid Ar and Cu. The parameters for the potentials for solid Ar and Cu are given in appendices A.1, A.2, and A.3, and all reduced units and corresponding normalization constants are specified in appendix D.

Lennard-Jones potential

The plot of thermal expansion of solid Ar against temperature is shown in Figure 5.2 and Figure 5.3. For the sake of clarity, Figure 5.2 shows only the results for methods based on the quasi-harmonic approximation. These include (i) the *max-ent* method with the quasi-harmonic approximation derived in Equations (2.95a)-(2.95c), (ii) the method based on the WKB theory, and (iii) the canonical ensemble approach from classical statistical mechanics derived in Equations (2.98a)-(2.98c). Figure 5.3 shows the thermal expansion of solid argon with temperature obtained with the *max-ent* approach using different quadrature rules. The results are compared with those of the classical theory, molecular dynamics simulations [42], as well as experimental data [29]. We enlist our observations as follows.

- Figure 5.2 ratifies the analytical prediction of section 2.5.3 that the *max-ent* distribution and the canonical distribution of Gibbs are identical under the local quasi-harmonic approximation for an isotropic perfect crystal undergoing uniform thermal expansion.

- It is instructive to note that the results of the WKB approach obtained for adiabatic conditions are also identical to the classical results which are obtained for isothermal

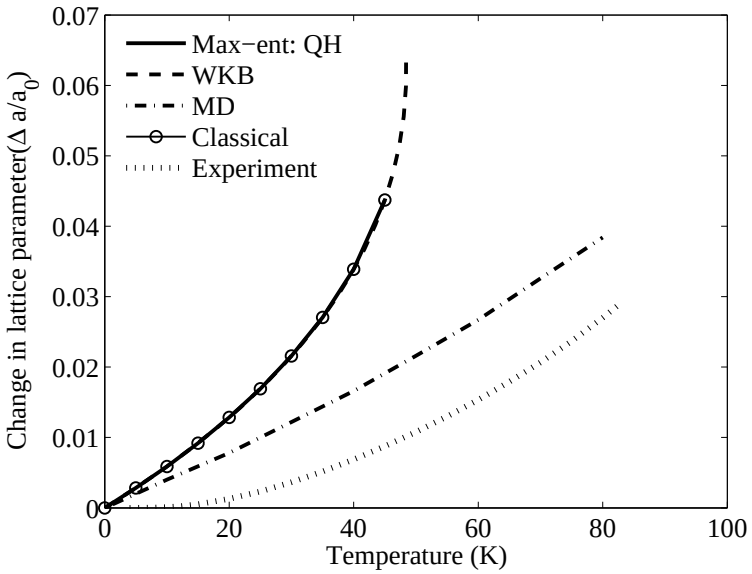

Figure 5.2: Thermal expansion of a perfect Lennard-Jones crystal using a) the *max-ent* method with the local quasi-harmonic approximation, b) the WKB method, and c) the classical canonical distribution. The material used is solid Argon.

conditions. This demonstrates the equivalence of the ensembles in the thermodynamic limit [45], i.e., when the number of particles in the system is very large, the microcanonical and the canonical ensemble yield the same thermodynamic functions. We recall that under adiabatic conditions, the *max-ent* method with the local quasi-harmonic approximation is equivalent to the WKB method. We also recall that the thermodynamic functions obtained using the former are equivalent to those derived from the Gibbs canonical ensemble for a perfect infinite crystal at uniform temperature. This explains the equivalence of the methods that we observe numerically.

- Since all these methods including MD are based on classical theory, they cannot capture the low temperature behavior as observed in the experiments. This is expected because the contribution of the quantum effects to the energy of the lattice vibrations becomes dominant at low temperatures as seen from the Boltzmann distribution.

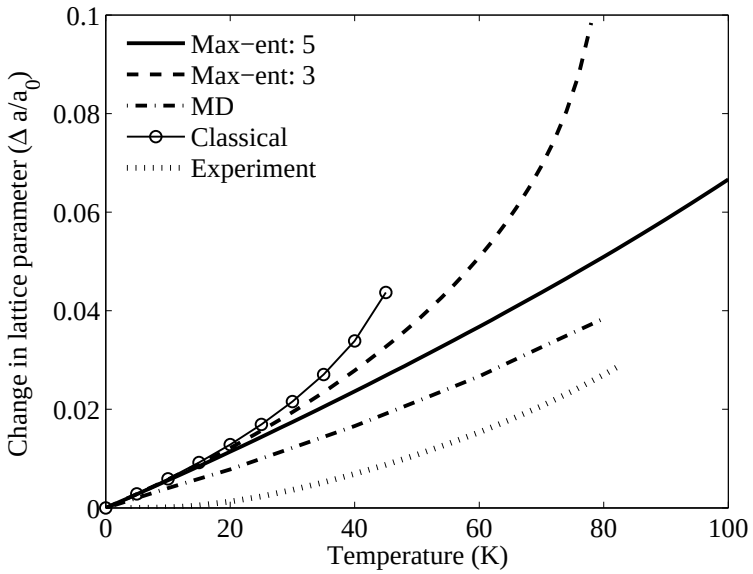

Figure 5.3: Thermal expansion of a perfect Lennard-Jones crystal based on the *max-ent* method using 3^{rd} and 5^{th} degree quadrature rules. The material used is solid Argon.

- Classical theory also predicts a linear dependence of the thermal expansion on temperature as demonstrated by the molecular dynamics results. However, Figure 5.2 shows that the results based on the quasi-harmonic potentials deviate significantly from linearity, beyond about 25 K which is less than half the melting point of solid Ar (83 K). This indicates the failure of the local quasi-harmonic approximation at high temperatures, when the lattice vibrations are large enough for the anharmonic terms to become important.

- Figure 5.2 also shows that even in the linear regime, the thermal expansion coefficient is much higher than that obtained from MD simulations. At 10 K, the value of α is about 31 % higher than the molecular dynamics result.

- In contrast, Figure 5.3 indicates that, with an anharmonic potential, the *max-ent* approach provides a significant improvement over the quasi-harmonic approximation.

This is certainly due to the accounting of anharmonicity of the interaction potentials which becomes dominant at high temperatures.

- The curve for the 5^{th} degree quadrature is linear in temperature as expected. However, the curve for the 3^{rd} degree quadrature is linear only up to about 50 K and consequently, the deviation in thermal expansion also becomes significant beyond 50 K. Thus, the range of validity is larger than that observed in the quasi-harmonic case. This is intuitive since it implies that the error in the results decreases with increase in the degree of quadrature rule.

- Finally, even with the 5^{th} degree quadrature rule, the value of the thermal expansion coefficient is higher as compared with MD. The value of α predicted by the *max-ent* distribution with 5^{th} degree quadrature rule at 40 K is close to 50 % higher than the experimental value and 33 % higher than that predicted by MD. However, at 80 K our result is within 10 % of the experimental value, which is $6.72 \times 10^{-4}\, K^{-1}$. Some potential sources of error could be the numerical quadrature, the mean field approximation, which leads to the Gaussian form of the local probability distribution, and the choice of interatomic potentials. We shall elaborate on the last point when we analyze the results obtained by using EAM-type potentials.

EAM-type potentials

As mentioned earlier, we study the thermal properties of copper using two interaction potentials, namely, an analytical form of the embedded-atom method (EAM) proposed by Johnson [18] and another EAM-type many-body potential proposed by Sutton and Chen [37]. The choice of the latter was dictated by the availability of molecular dynamics results in the work of Çağin and coworkers [4] and due to the lack of MD results for thermal

expansion based the EAM-Johnson potential. We recall from section 2.4 that for many-body interactions we are limited to the use of 3^{rd} degree quadrature due to the high dimension of the configurational phase space.

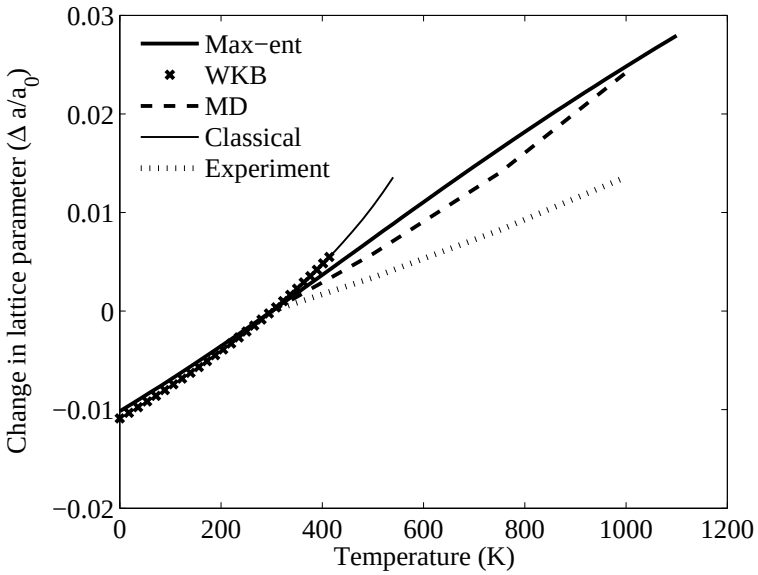

Figure 5.4: Thermal expansion of a perfect crystal of Cu based on a) *max-ent* method with 3^{rd} degree quadrature, b) WKB method, and c) classical canonical distribution. The results are based on the Sutton-Chen potential.

Figure 5.4 shows the thermal expansion of Cu versus temperature based on the Sutton-Chen potential. The methods used include (i) the *max-ent* method with 3^{rd} degree quadrature formula, (ii) the method based on WKB technique, and (iii) the canonical ensemble approach from classical statistical mechanics. In this figure, ε represents the expansion with respect to the lattice parameter at $T = 300$. That is,

$$\varepsilon = \frac{a(T)}{a(300)} - 1\,.$$

We use $T = 300$ as the reference because the MD and experimental data are presented in [4] in this form and this is the range in which the experimental data shows a linear dependence

on temperature [28]. Based on Figure 5.4, we draw the following conclusions:

- As observed in the case of Lennard-Jones potential, the thermal expansion curve for the formal asymptotics approach lies exactly on the curve for the classical theory. Furthermore, both give a higher estimate of the thermal expansion coefficient due to the quasi-harmonic approximation and fail to converge beyond 540 K.

- We observe that the thermal expansion coefficient computed with the *max-ent* method is in reasonable agreement with the molecular dynamics results, although it is based on the 3^{rd} degree quadrature. The thermal expansion has a linear dependence on temperature as expected. Quantitatively, at 300 K, the *max-ent* result for α is about 38 % higher than the MD value. However, at 1000 K, it is 18 % lower than the MD value. Furthermore, compared to the classical results for the local quasi-harmonic approximation, the *max-ent* approach reduces the error significantly at high temperatures.

- Finally, we observe that the results for the *max-ent* method as well as the molecular dynamics simulations are not in a close agreement with the experimental data. This is indicative of a limitation of the Sutton-Chen potential to model thermal properties rather than that of the proposed methods since these potentials are parameterized based on the bulk properties at 0 K and may not be suitable for finite temperature calculations. This is also confirmed by the results for the EAM-Johnson potential.

Figure(5.5) shows the thermal expansion of Cu versus temperature based on the EAM-Johnson potential. As before, the methods used include (i) the *max-ent* method with 3^{rd} degree quadrature formula, (ii) the method based on WKB technique, and (iii) the canonical ensemble approach from classical statistical mechanics. A significant difference

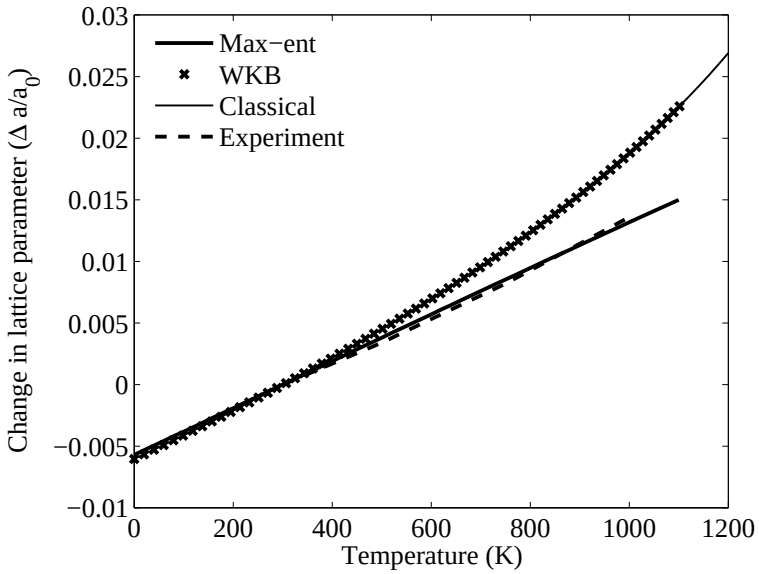

Figure 5.5: Thermal expansion of a perfect crystal of Cu based on a) *max-ent* method with 3^{rd} degree quadrature, b) WKB method and c) classical canonical distribution. The results are based on the EAM-Johnson potential.

may be observed between the results of the Sutton-Chen potential and the EAM-Johnson potential, the latter being able to capture the thermal expansion very well. Based on these numerical results, we conclude the following:

- The *max-ent* method is in excellent agreement with the experimental observations for the range of temperatures for which classical theory is valid.

- The results based on the WKB method and the classical canonical distribution also show considerable improvement as compared to their counterparts based on the Sutton-Chen potential. At 300 K, the value of α is equal to that obtained from experiments. However, they still give higher estimates for the thermal expansion coefficients as expected at high temperatures. This is in agreement with the conclusions of LeSar et al. [23] regarding the local quasi-harmonic approximation. At 1000 K, the value of α becomes almost 35 % higher than the experimental.

- Although we do not have MD results based on this potential, we may conjecture, based on the results for Lennard-Jones and Sutton-Chen potentials, that the thermal expansion obtained from MD should also be in very good agreement with experiments.

- We make a final note that unlike in the case of the Lennard-Jones potential, the 3$^{\text{rd}}$ degree quadrature works very well for the EAM-type potentials and hence suffices for the purpose of these calculations. This could, probably, be an effect of considering many-body interactions in the latter as opposed to pairwise interactions in the former. The same possibility also emerges from the study of the specific heats of copper and solid argon given below.

5.1.2 Specific heat

The specific heat of a system in thermal equilibrium at uniform temperature T at constant volume and at constant pressure are defined in thermodynamics as [40, 41]

$$C_v = \frac{1}{N}\left.\frac{\partial E}{\partial T}\right|_V , \;\; C_p = \frac{1}{N}\left.\frac{\partial H}{\partial T}\right|_p , \tag{5.7}$$

where N is the number of atoms in the crystal, and $H = E + pV$ is the enthalpy of the system. Hence, for processes at zero pressure, H is equal to E. The specific heats in Eq. (5.7) are expressed per atom. Recalling the expression (2.95a) for the internal energy furnished by the canonical distribution and differentiating with respect to temperature yields

$$C_v = 3k_B \, . \tag{5.8}$$

This is known as the law of Dulong and Petit and is based on classical statistical thermodynamics [1]. Real systems are found to be in agreement with this law only at reasonably

high temperatures when quantum effects may be neglected. However, since the anharmonic effects dominate at high temperatures, the specific heat is still found to be slightly lower than $3k_B$. We note that all our methods based on the quasi-harmonic approximation have the internal energy of the form

$$E(\bar{\boldsymbol{q}}) = V(\bar{\boldsymbol{q}}) + 3Nk_BT\,. \tag{5.9}$$

These methods include the *max-ent* approach with the quasi-harmonic approximation and the method based on formal asymptotics. Consequently, they yield the Dulong and Petit model for the specific heat at constant configuration. The details of the tests for computing the specific heats using the *max-ent* approach with anharmonic potentials are as follows. The test sample and boundary conditions are as described earlier. Since the thermal expansion tests are performed at zero pressure, C_p may be evaluated as the instantaneous slope of the internal energy versus temperature obtained from these tests. C_v is obtained by fixing the configuration at the initial state and equilibrating the system at the prescribed temperature T_0. The minimization problem becomes

$$\min_{\omega\in\mathbb{R}} F(a_0, T_0, \omega)\,. \tag{5.10}$$

We now present our results for C_v and C_p for the Lennard-Jones and the EAM-type potentials.

Lennard-Jones potential

Figure 5.6 and Figure 5.7 show the variation of the internal energy per atom with temperature under conditions of constant volume and temperature (NVT) and constant pressure

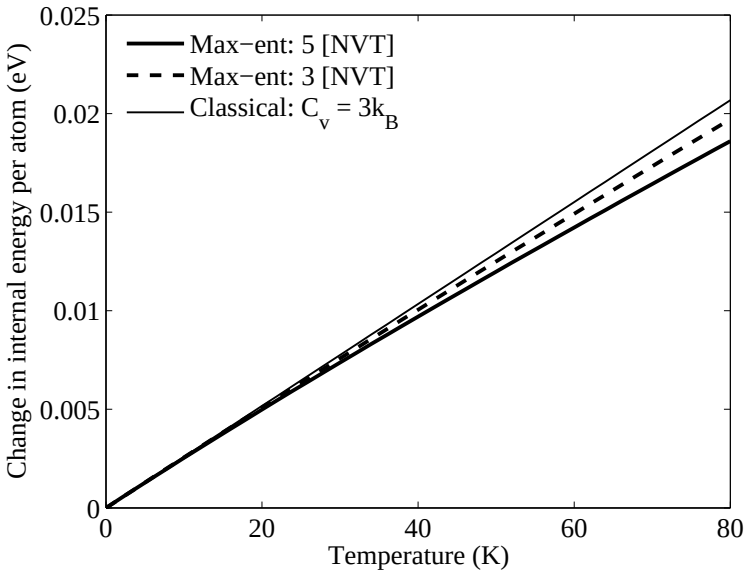

Figure 5.6: Comparison of the change in internal energy of a perfect Lennard-Jones crystal under NVT conditions using the *max-ent* method with the Dulong and Petit model. The material used is solid Argon.

and temperature (NPT), respectively. The energy is plotted for 3^{rd} and 5^{th} degree quadrature rules. We enlist our observations as follows:

- Figure 5.6 shows that the change in internal energy with temperature obtained by using both quadrature rules is in very good agreement with the classical law of Dulong and Petit. As the temperature becomes very high compared to the melting temperature of 83 K, and anharmonic terms dominate, the slopes begin to deviate from $3k_B$ as expected. Even at 80 K, the C_v obtained from the 3^{rd} and 5^{th} degree quadrature rules are almost equal and differ from $3k_B$ by about 1.0 %. However, this value differs from the experimentally observed value of 2.49×10^{-4} eV per atom [9] at the same temperature by 2.7 % .

- Based on Figure 5.7, we can draw a qualitative conclusion that the *max-ent* approach satisfies the inequality $C_p > C_v$. However, the result for the 3^{rd} degree quadrature

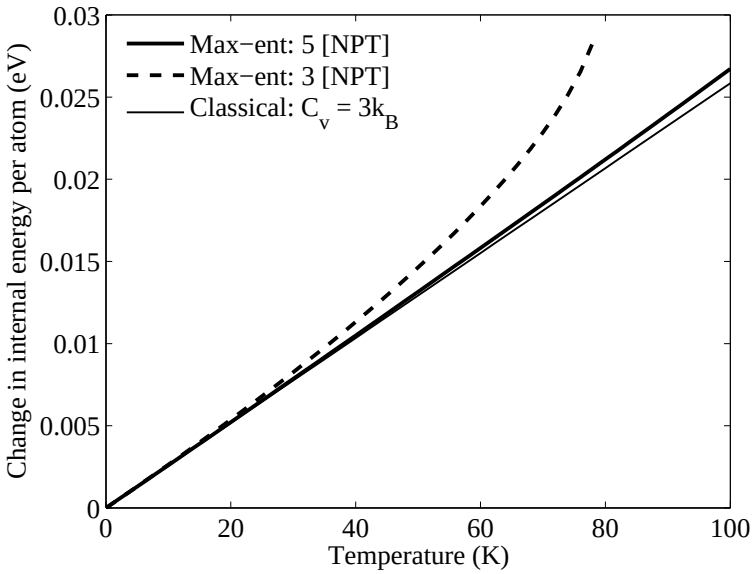

Figure 5.7: Change in internal energy of a perfect Lennard-Jones crystal under NPT conditions using the *max-ent* method with 3rd degree and 5th degree quadrature rules. The material used is solid Argon.

rule overestimates the value of C_p. This is consistent with its behavior for thermal expansion as shown in Figure 5.3.

- Finally, we note that these results are consistent in the sense that the 3^{rd} degree quadrature rule always predicts higher energy than the 5^{th} degree quadrature since it is closer to the quasi-harmonic case.

EAM-type potentials

Figure 5.8 and Figure 5.9 show the variation of the internal energy per atom with temperature under NVT and NPT conditions for the Sutton-Chen and EAM-Johnson potentials, respectively. As in the case of thermal expansion, these results are in better agreement than those for the Lennard-Jones pair potential. We observe that the C_v is in very close agreement with the classical value of $3k_B$ for both the potentials. However, the C_v decreases slightly at high temperatures due to anharmonic effects as expected. Again, as expected,

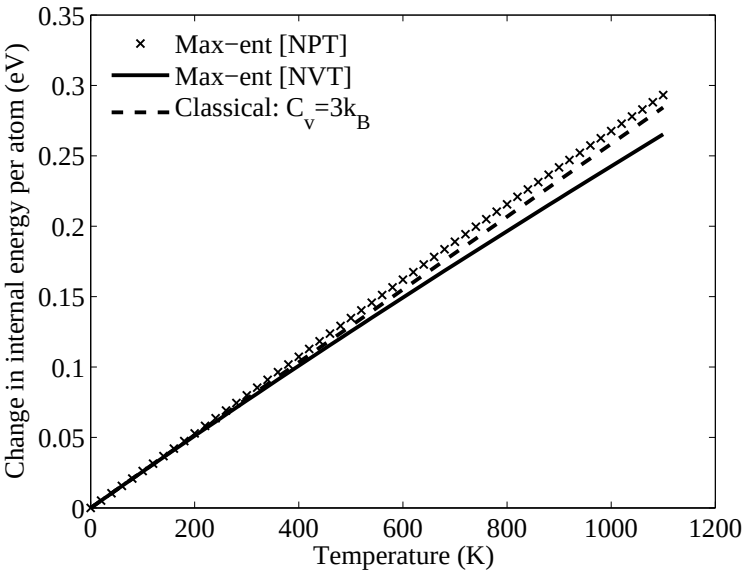

Figure 5.8: Comparison of the change in internal energy of a perfect crystal of Cu under NPT and NVT conditions using the *max-ent* method with the Dulong and Petit model. The results are based on the Sutton-Chen potential.

the *max-ent* approach satisfies the identity that $C_p > C_v$. We note again that the 3^{rd} degree quadrature gives very reasonable results for C_v and C_p, unlike in the case of the Lennard-Jones potential, and probably shows the sensitivity of the method towards whether the quadrature rule is applied to the phase space for many-body or pairwise interactions.

We conclude this section by summarizing the highlights of the results presented so far. The numerical tests confirm that by accounting for the anharmonic terms in the interaction potential, the *max-ent* approximation scheme leads to a substantial improvement over the traditional local quasi-harmonic approximation in modelling the thermal properties numerically. It also works for a much larger temperature range. At about half the melting temperature, it reduces the error by almost 50 % for the Lennard-Jones and the Sutton-Chen potential, whereas for the EAM-Johnson potential, it almost eliminates the error. We also note that the results indicate a possible dependence of the quadrature rule on the interatomic potentials, and hence a study to determine the optimal quadrature rule

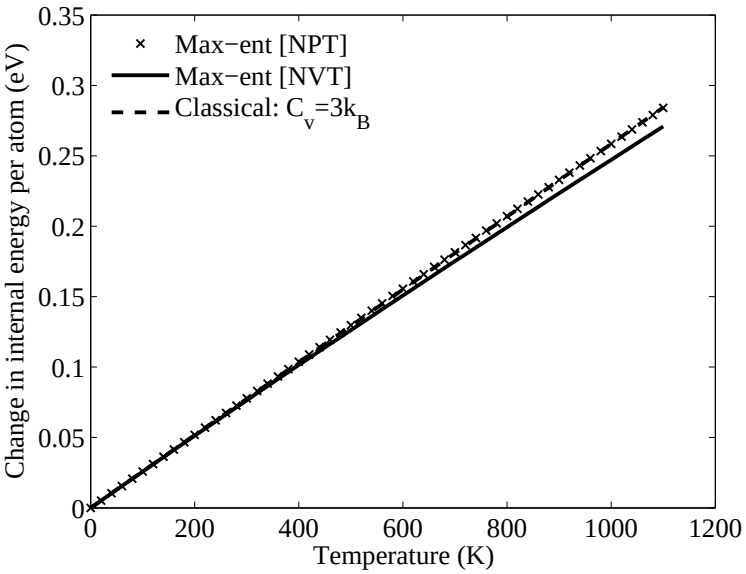

Figure 5.9: Comparison of the change in internal energy of a perfect crystal of Cu under NPT and NVT conditions using the *max-ent* method with the Dulong and Petit model. The results are based on the EAM-Johnson potential.

for different types of interactions (pairwise, many-body) should be worthwhile. It also bears emphasis that, like molecular dynamics, our approaches are also limited by the choice of the interaction potential. This is due to the fact that the potential is the soul source of empiricism in the model. It is usually parameterized using bulk properties at zero temperature and hence may not be suitable for capturing the thermal behavior of materials that we are interested in. The contrast between the results of the Sutton-Chen and the EAM-Johnson potential for the same material serves to illustrate the point. Thus, in other words, we can only do as good as the empirical potential. Furthermore, this also highlights the importance of comparing the proposed methods with molecular dynamics simulations for the same potential and test sample rather than with experiments only.

5.2 An adiabatic tension test

This is an illustrative example by way of which we wish to verify the capability of the proposed methods to simulate the thermo-mechanical coupling via thermoelastic effects. A way to model thermoelastic effects is to perform a tension or compression test under adiabatic conditions which should reflect the effect of the local mechanical deformation on the local temperature. A description of the test and a discussion of the results are presented below.

Test problem definition

The sample used in the simulations is an fcc Lennard-Jones crystal with $4 \times 4 \times 12$ unit cells in the three directions comprising of 1013 atoms. The applied boundary conditions are as follows. To treat the cube as lying on a rigid surface, only the z-displacement of the atoms on the bottom surface is restricted. Using the symmetry of the problem, the atom at the center of the node is fixed completely in order to avoid rigid motion. A uniform initial temperature of 42 K ($0.5\,T_m$) is prescribed on the cube, while all the surfaces are thermally insulated.

The test is performed using the WKB approach and the *max-ent* approach as it enables us to observe the impact of the anharmonic terms. First, the sample is allowed to equilibrate at the prescribed temperature adiabatically, which leads to a decrease in temperature. This is achieved in the *max-ent* method by minimizing the internal energy at constant entropy or simply by using $\triangle t = 0$. The relaxed sample is then subjected to the tension test, which is implemented by applying displacement boundary conditions on the atoms of the top surface. We use an increment of $0.05[\sigma]$, which is about 0.3 % of the length of the sample.

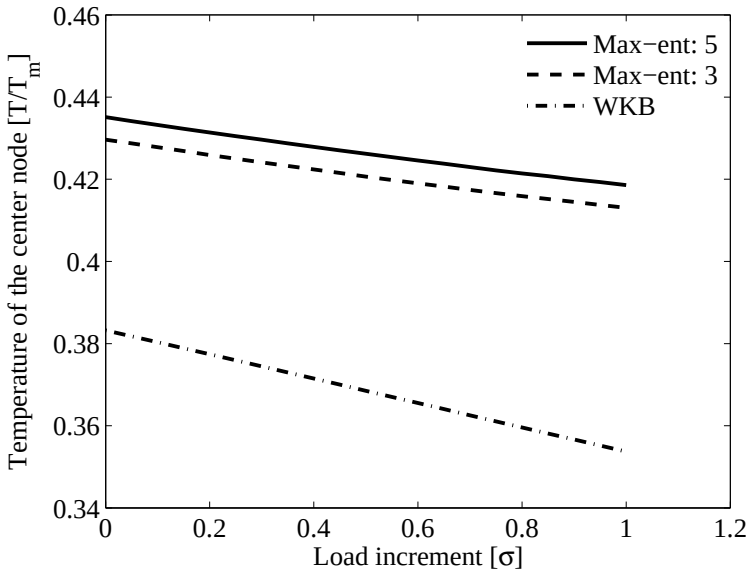

Figure 5.10: Evolution of the temperature of the atom in the center of the sample versus load increment during the adiabatic tension test. The temperature at zero load correspond to the value after initial thermal expansion.

Discussion

Figures 5.10 and 5.11 show the change in temperature and the displacement of the node at the center of the sample. In both the plots, the temperature and displacement at zero load are the values obtained after the initial relaxation. Figure 5.12 shows some snapshots of the sample at different load increments during the simulation. The contours represent the temperature. These results enable us to make the following qualitative deductions.

- It may be observed that the temperature of the body decreases as the sample is pulled, which is in accord with the expected behavior. As the sample is pulled, the interatomic spacing increases which leads to a decrease in the frequencies of the atoms. This implies a corresponding decrease in the energy in the lattice vibrations and, hence, the temperature.

- We also note from Figure 5.12 that the surface effects lead to a larger decrease in

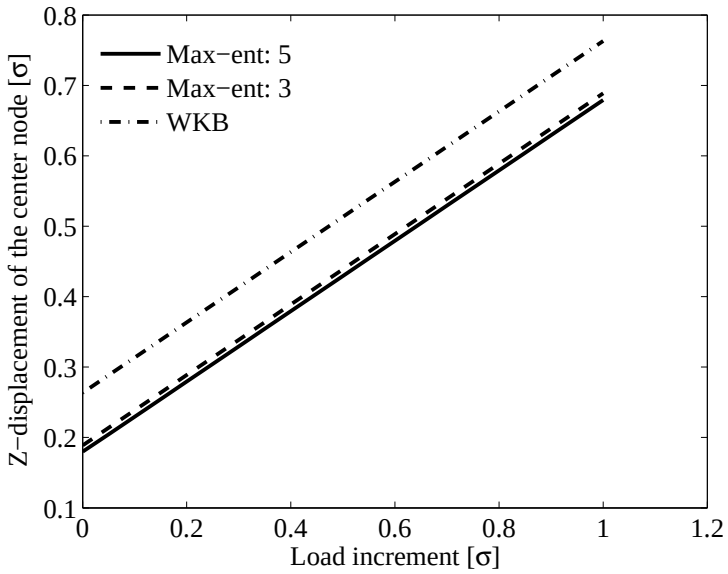

Figure 5.11: z-displacement of the atom in the center of the sample versus load increment during the adiabatic tension test. The displacement at zero load corresponds to the initial thermal expansion.

temperature on the surfaces and edges of the sample.

- Finally, on comparing the three methods, it is interesting to note that the only significant difference in the temperature and extension of the sample occurs during the initial relaxation.

5.3 A heat conduction example

In Chapter 3 we proposed a variational formulation for modelling non-equilibrium phenomena such as heat conduction by appending to the equilibrium equations, the equation of energy balance. Here, we seek to demonstrate the ability of the proposed QC framework to simulate thermo-mechanical coupled behavior and the dissipation of heat through a crystal by way of a numerical test subjecting a crystal to an initial non-uniform temperature profile.

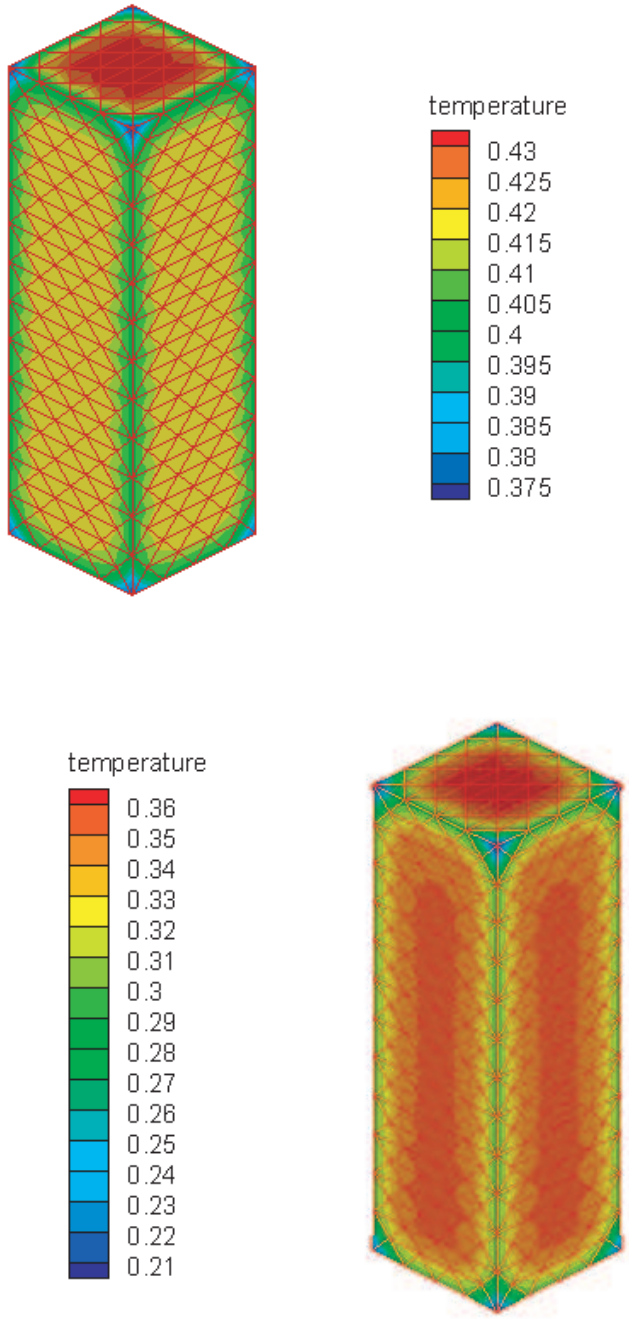

Figure 5.12: Temperature profile at $\delta = -0.5[\sigma]$ showing surface effects during the adiabatic tension test based on the WKB method (bottom) and the *max-ent* method with 5^{th} degree quadrature (top).

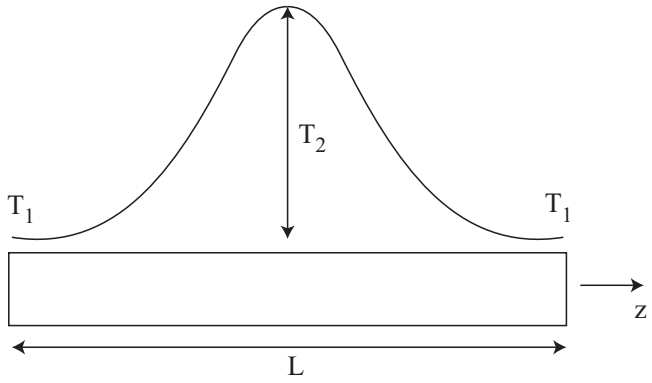

Figure 5.13: The initial temperature profile in the form of a Gaussian function for the heat conduction example. The temperature T_1 on the two ends is fixed.

Test problem definition

The sample used in the simulations is an fcc Lennard-Jones crystal with $4 \times 4 \times 12$ unit cells in the three directions comprising of 1013 atoms. The crystallographic orientation is as shown before (Figure 5.1). Only first nearest neighbor interactions are considered. The displacement boundary conditions are as follows. Atoms in the bottom surface are fixed at their initial positions, whereas in all side surfaces the atoms are constrained to move only in the z-direction. No displacement constraints are introduced on the top surface. Since we shall prescribe non-uniform temperature along the z-direction, these boundary conditions enable us to use the length of the cube in the z-direction as a measurement of thermal expansion.

The initial temperature distribution is shown in Figure 5.13. The temperature at the two ends is fixed at a value T_1, and the initial temperature of the rest of the atoms is prescribed to have a Gaussian profile along the z-direction. That is,

$$T(z) = T_2 \exp\left[-\frac{(z - L/2)^2}{\lambda^2}\right] + T_1\,, \tag{5.11}$$

where L is the length of the crystal in the z-direction. Thus, all atoms lying in the same

cross-section normal to the z-direction have the same initial temperature. We have used the following parameters for the simulations in order to avoid a very sharp peak due to the small size of the sample:

$$T_1 = 0.29\ T_m,\ \ T_2 = 0.29\ T_m,\ \ \lambda^2 = 10\,,$$

where the melting temperature T_m for solid Ar is 83 K. Intuitively, if we allow the crystal to relax, the heat pulse should diffuse through the crystal, and at equilibrium, the sample should have a uniform temperature T_1 and the corresponding thermal expansion.

As discussed in Chapter 3, we treat this rate problem as an incremental extremum problem stated in Eq. (3.44). The test is performed based on the *max-ent* approach with 3^{rd} as well as 5^{th} degree quadrature. We use the conjugate gradient method to perform the minimizations. However, since the conjugate gradient method cannot be used to determine saddle points, we separate the above problem into two nested loops of conjugate gradient method. The outer loop minimizes over $\bar{\boldsymbol{q}}$ and $\{\omega\}$. At every line search of this conjugate gradient loop, the nested conjugate gradient loop is called to maximize Φ_n with respect to the temperature corresponding to the current values of $\bar{\boldsymbol{q}}$ and $\{\omega\}$. The time step in the heat equation is chosen to be 0.35 ps. The conductivity of solid Ar is $0.7\,W\,m^{-1}K^{-1}$, which is normalized to unity and absorbed in the reduced unit for time. The details are presented in appendix D.

Discussion

Figure 5.14 and Figure 5.15 show the evolution of the temperature and the z-displacement of the node in the center of the crystal. We choose this node because the cross-section in the center experiences the highest temperature initially. Figure 5.16 shows the temperature

profile along the sample at different time intervals during the simulation. For the purpose of comparison, the same test is also performed on a rigid conductor. We use the same initial and boundary conditions and the same test sample. Since the cube is rigid, the interaction potential becomes irrelevant. We also know that the governing equation for heat conduction in a rigid bar is the parabolic partial differential equation:

$$C_v\dot{T} = \kappa\Delta T, \tag{5.12}$$

where we use the classical value for the specific heat, i.e., $C_v = 3k_B$. As discussed in Chapter 3, we discretize the equation in time based on the backward Euler finite difference scheme and obtain the evolution of temperature by treating the problem as an incremental variational problem. The result is shown in Figure 5.14. The exponential decay of the Gaussian peak with time is in agreement with the analytical solution of Eq. (5.12). Based on these results, we make the following observations:

- Both quadrature rules yield almost identical solutions for the evolution of temperature, as shown in Figure 5.14. Furthermore, the temperature evolution predicted by the *max-ent* method is also exponential and in fact decays faster than in the case of the rigid conductor. This behavior may be explained on the basis of physical understanding of the thermo-mechanical coupled problem. Since in this case some of the energy contained in the lattice vibrations is used in the thermal relaxation of the crystal, it accelerates the decay of the temperature pulse.

- From Figure 5.15 we observe that using the 3^{rd} degree quadrature shows a higher z-displacement as the crystal relaxes under the initial temperature profile. This discrepancy in results for the 3^{rd} and 5^{th} degree quadrature rule are consistent with the

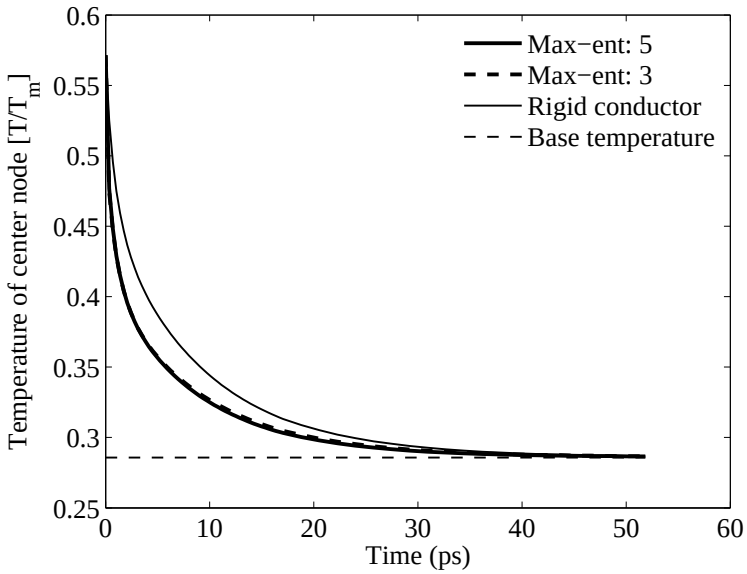

Figure 5.14: Evolution of the temperature of the center atom of a Lennard-Jones solid with a prescribed initial temperature profile having a Gaussian form. The temperature is normalized with the melting temperature of solid Argon, $T_m = 83K$.

thermal expansion results discussed in the previous section.

- Nevertheless, after the first jump in the z-displacement of the center node, the subsequent change in displacement is very similar for both the quadrature rules as it follows the exponential decay of the temperature.

- It is also verified that the *max-ent* solution for the thermal expansion converges to the value obtained when the same sample is allowed to expand under isothermal conditions at a uniform temperature T_1. This is in agreement with our expectation since this is the equilibrium solution for the heat equation consistent with the essential boundary conditions.

- Finally, we wish to emphasize that the short time-step used in this test is selected in order to capture the initial phase comprising of the rapid evolution of temperature and deformation. To get an idea, the critical time step can be estimated as a function

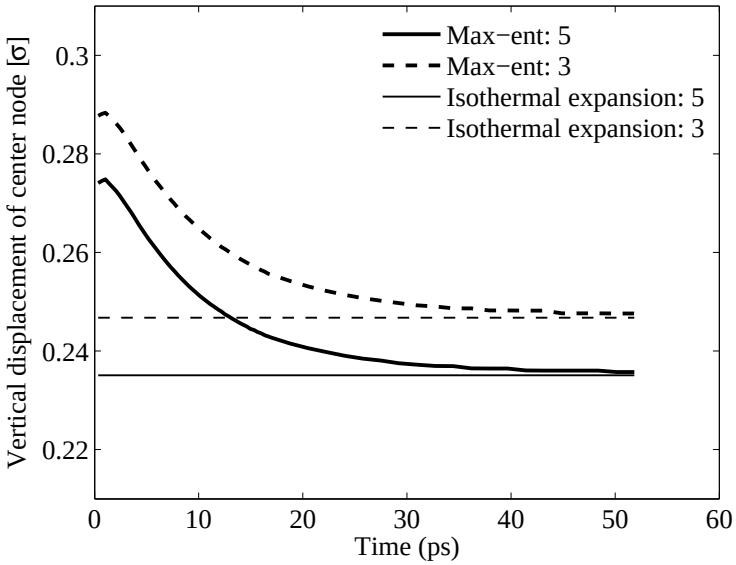

Figure 5.15: z-displacement of the center node of a Lennard-Jones bar during the dissipation of the prescribed initial temperature profile having a Gaussian form.

of the mesh size as

$$\Delta t_c \approx \frac{h^2}{D}\,, \tag{5.13}$$

where D is the diffusion constant for the material. Since the sample used is atomistic, h is the lattice spacing. Then, for solid argon,

$$h = \sqrt{2} \times 3.4 \times 10^{-10}\ m, \quad D = \frac{\kappa}{\rho C_v} = 8.346 \times 10^{-7}\ m^2/s\,. \tag{5.14}$$

This gives

$$\Delta t_c = 0.277\ ps\,.$$

In case of a coarse-grained mesh, the critical time step would increase as the square of the element size. Furthermore, the time-discretization of the variational problem is based on the backward Euler finite difference scheme, which is unconditionally stable.

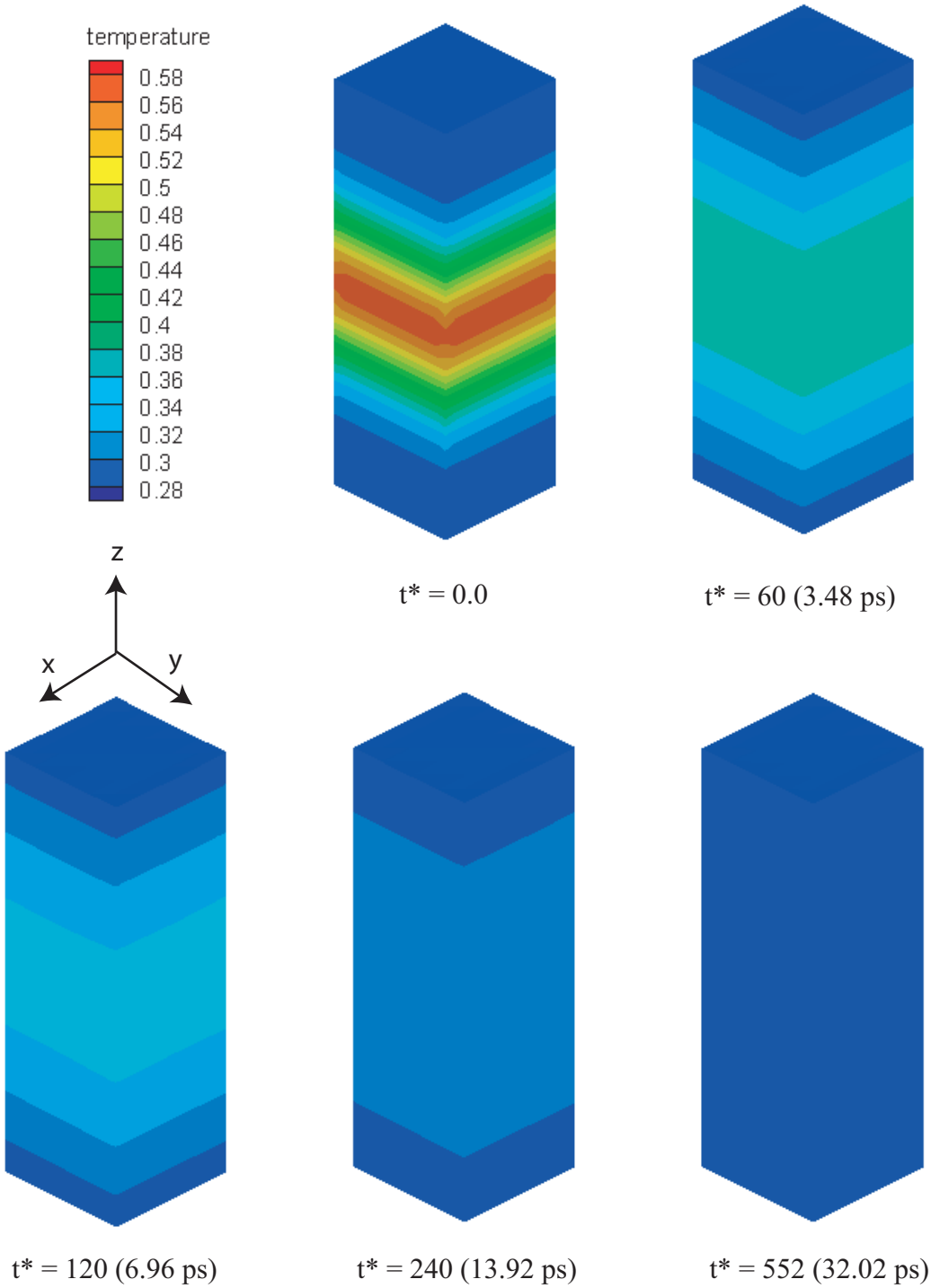

Figure 5.16: Snapshots at various time intervals during the heat conduction simulation showing the dissipation of a prescribed initial temperature profile having a Gaussian form. The test is performed using the *max-ent* approach with 3^{rd} degree quadrature rule.

Thus, no limitation is imposed on the time step by the method. This is one of the chief advantages of the *max-ent* approximation, that it allows for larger time steps and hence can simulate very slow processes as well. This is unlike MD, which is limited by a time step of about 10^{-14} seconds, which is on the order of the time-period of the thermal oscillations of the atoms.

5.4 Nanoindentation examples

The final overarching application of the finite temperature quasicontinuum framework that is pursued in this work is the nanoindentation problem. Nanoindentation is a conventional experimental tool to study complex material behavior such as microstructure evolution via defect nucleation. Since thermal effects may play a significant role in such microscopic phenomena, we use nanoindentation examples to demonstrate the capabilities of the proposed methods and open directions for future applications.

Nanoindentation with a spherical indenter

One of the nanoindentation tests that we simulate is with a spherical indenter. The test is performed using the WKB method and, hence, under adiabatic conditions.

Test problem definition

The test sample is an fcc nearest-neighbor Lennard-Jones crystal with $32 \times 32 \times 32$ unit cells, or a total of 137,313 atoms. The surfaces of the sample are aligned with the cube directions (Figure 5.1). The imposed boundary conditions are the same as in the adiabatic test in order to allow stress-free initial thermal expansion of the crystal. The indenter is applied on this relaxed sample. An initial temperature of $0.5T_m$ is prescribed, and all the surfaces are thermally insulated. The initial mesh is tailored to the nanoindentation geometry with

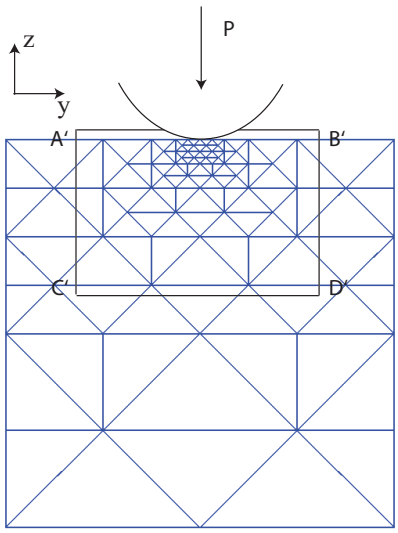

Figure 5.17: Geometry of the nanoindentation setup for a spherical indenter and the initial mesh. A'B'C'D' is the region shown in the snapshots of the temperature evolution.

atomistic resolution just under the indenter and an increasingly coarser triangulation away from this region. Figure 5.17 shows the triangulation of a cross-section through the center of the cube with $y = \text{const}$. The initial number of nodes is 757 which is a significant reduction from the total number of atoms.

For the spherical indenter, we use a model proposed by Kelchner et al. [20] and used in the analysis of the quasicontinuum method presented in [21]. The indenter is implemented as an external potential interacting with atoms on the top surface of the cube. The potential is of the form

$$\Phi^{ext}(r) = A\, H(R-r)\,(R-r)^3\,, \tag{5.15}$$

where R is the radius of the indenter, r is the distance between a site and the center of the indenter, A is a force constant and $H(r)$ is the step function. In our calculations, the parameters have the following values:

$$R = 25\,[\sigma], \quad A = 2000\,[4\epsilon/\sigma^3]\,. \tag{5.16}$$

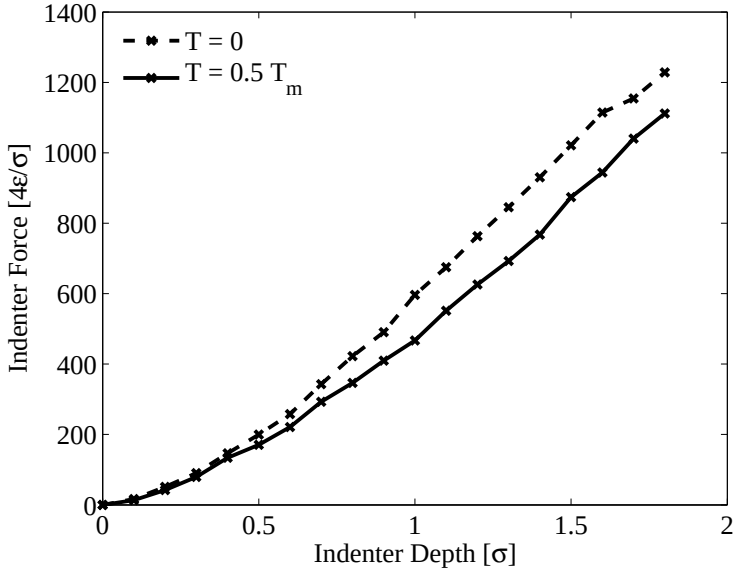

Figure 5.18: Force versus indenter depth plot for the nanoindentation test with a spherical indenter using the WKB method.

Discussion

Figures 5.19 and 5.20 show the snapshots of the temperature profile in the vicinity of the indenter at various indenter depths during the simulation. The images are of the region A'B'C'D' of the cross-section under the indenter, shown schematically in Figure 5.17. Figure 5.18 also shows a comparison of the force versus indenter depth curves obtained at finite temperature and zero temperature. These results enable us to make the following qualitative interpretations:

- Figures 5.19 and 5.20 show a significant change in temperature during the nanoindentation simulation. This is true even as the crystal deforms elastically before the nucleation of defects. Although the prescribed temperature is $0.5\,T_m$, the temperature at the start of indentation is about $0.32\,T_m$ since the initial thermal expansion is adiabatic. The maximum temperature reached when $\delta = -1.8\,[\sigma]$ is about $0.58\,T_m$, which is a 80% rise. Based on the analysis of the results for bulk properties and the

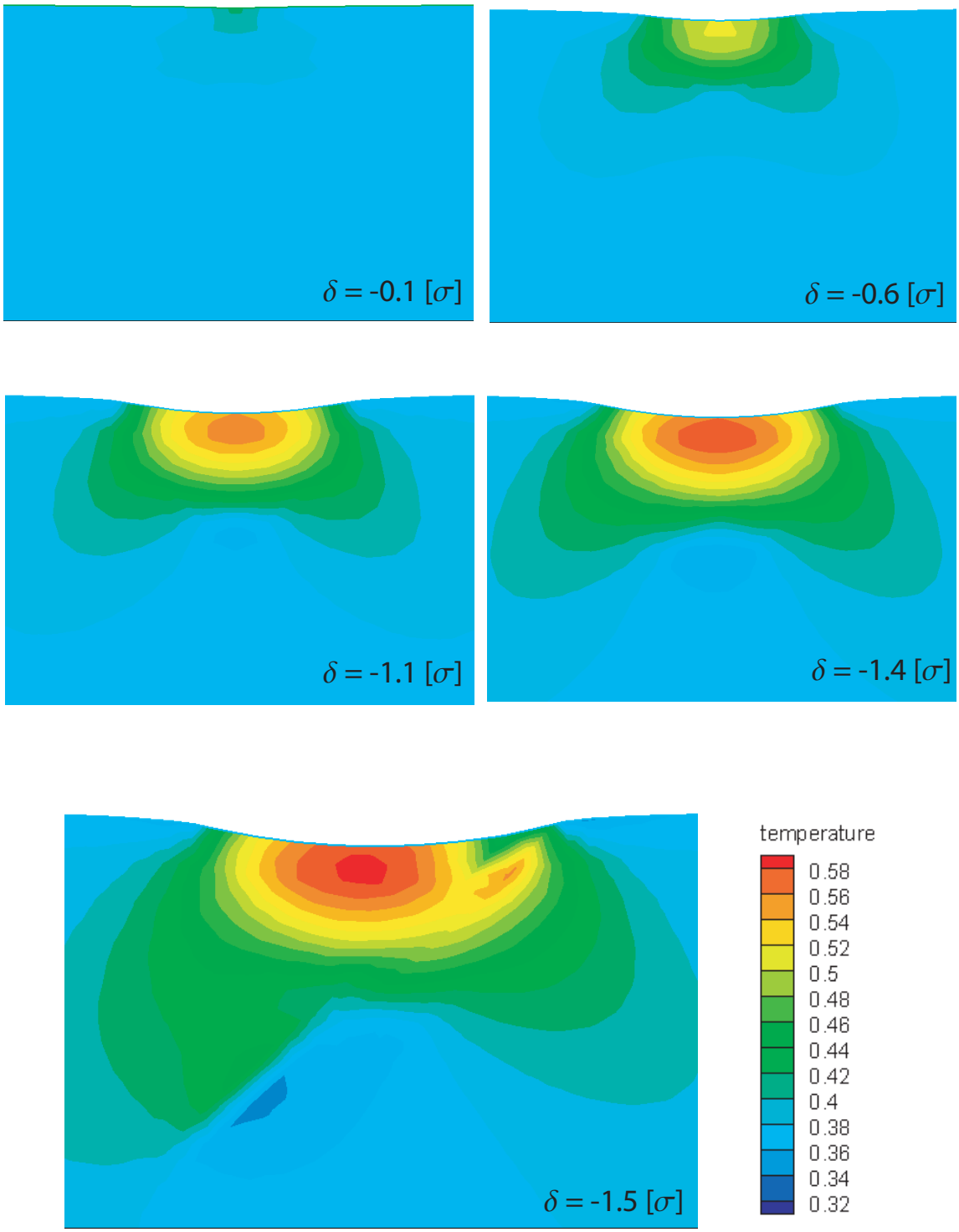

Figure 5.19: Snapshots showing the temperature profile of a section under the indenter at different indentation depths during the simulation. The test is performed using the WKB approach under adiabatic conditions.

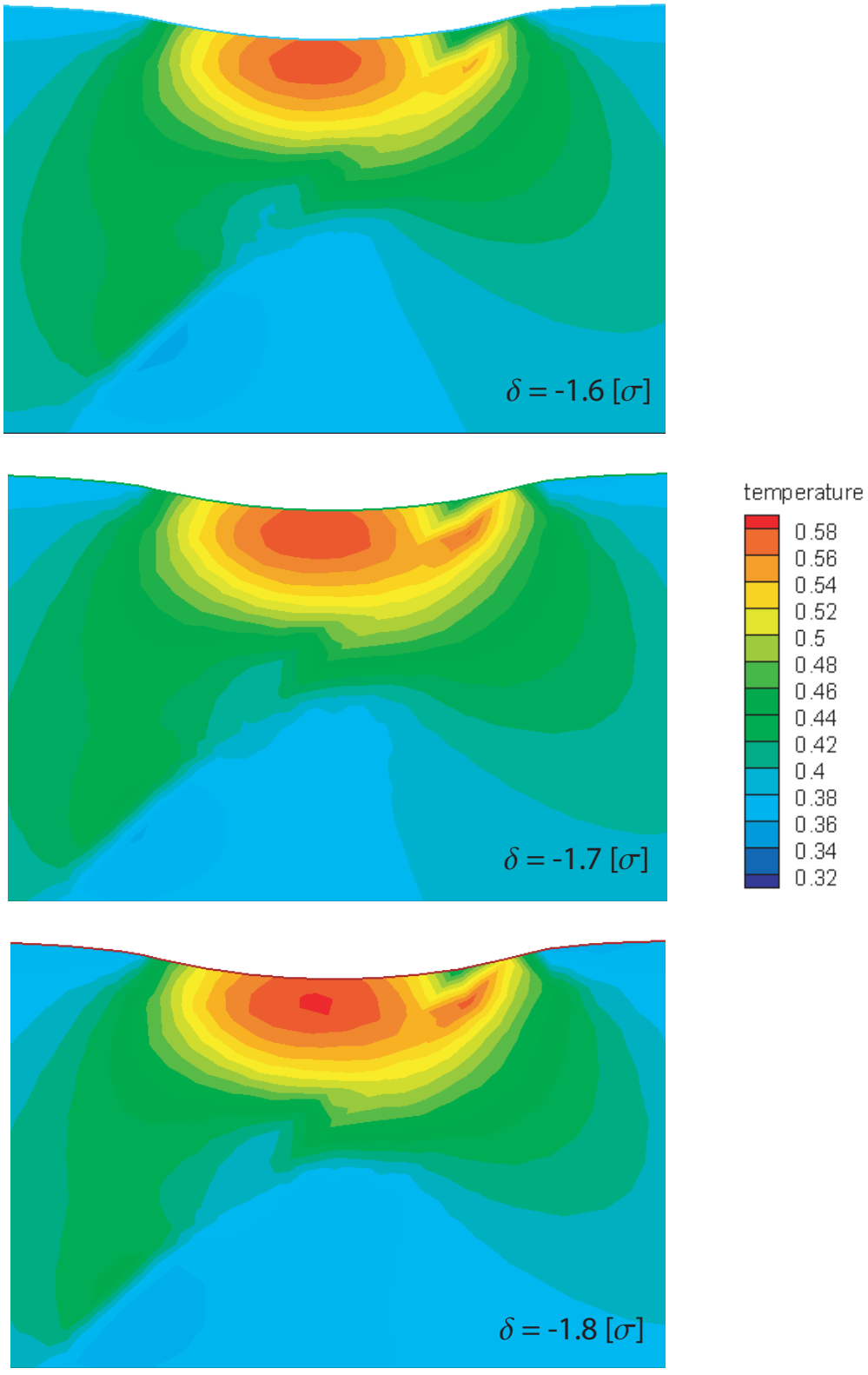

Figure 5.20: Snapshots at subsequent load increments showing the temperature profile under the indenter after a dislocation has nucleated. The test is performed using the WKB approach under adiabatic conditions.

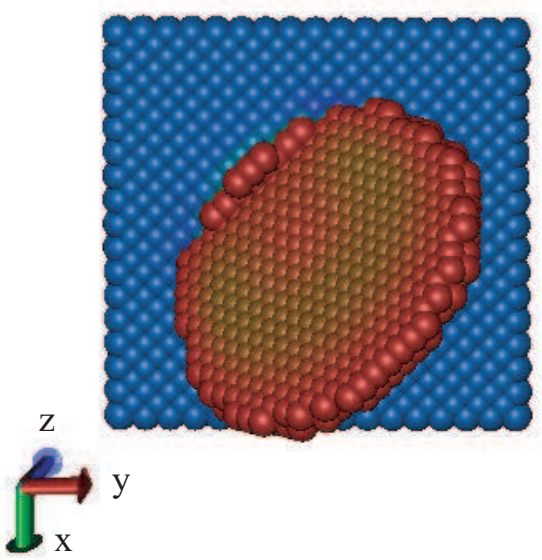

Figure 5.21: Dislocation structure under a spherical indenter predicted by the quasicontinuum method at indentation depth $\delta = 1.7[\sigma]$ under adiabatic conditions based on the WKB approach. The figure displays the energetic atoms (red) under the top surface of the crystal (blue).

adiabatic tests, we note that this may be an implication of the quasi-harmonic approximation, which is found to give higher estimates for thermal expansion. Consequently, it should also predict greater change in the local temperatures, which depend on the local deformation through Eq. (4.68). This rationale needs further investigation by comparing with molecular dynamics studies.

- Another manifestation of the quasi-harmonic approximation is the significant thermal softening observed in Figure 5.18 on comparison with the force versus indenter depth curve for zero temperature. Although softening is expected based on our understanding of behavior of solids on the continuum scale, the predictions may be overestimates due to the aforementioned reason.

- We also note from Figure 5.19 that at non-zero temperature the first dislocation is nucleated at the indenter depth of $1.5\,[\sigma]$, and the corresponding force is about 4282.3

pN. This is also indicated by a slight reduction in the slope of the force-indenter depth curve, although it is not very sharp. In the zero temperature case, the first dislocation is observed at $\delta = -1.6\,[\sigma]$, and the corresponding indenter force is 5462.5 pN. This confirms that defects are nucleated earlier, that is, at lesser force as well as lesser indenter depth, at finite temperature. This is in qualitative agreement with the observation of Dupuy et al. [10] and the experimental study by Schuh et al. [32].

- The difference in the images at $\delta = -1.4\,[\sigma]$ and $\delta = -1.5\,[\sigma]$ shows that the dislocation leads to an increase in temperature under the indenter along the (111) slip plane. On continuing the loading (Figure 5.20), the dislocation is observed to move towards the free surface while the hot region under the indenter along the slip plane continues to spread.

- Figure 5.21 shows the dislocation structure under a spherical indenter predicted by our method. The defect structures are extracted using the centrosymmetry parameter as described in [20]. The result is in agreement with defect structures observed in fcc crystals [15]. We observe that a partial dislocation loop is emanated under the indenter along the (111) plane. Moreover, since the nearest-neighbor Lennard-Jones potential has zero stacking fault energy, we observe that the stacking fault grows in area as the indentation continues.

Nanoindentation with a rectangular indenter

Here we describe a nanoindentation test with a rectangular indenter based on the *max-ent* approach with 3^{rd} degree quadrature rule. Nanoindentation using this indenter has been studied in [34] as a plain strain problem. We choose to use the 3^{rd} degree quadrature based on the fact that the results for the tension test using the 3^{rd} and the 5^{th} degree

quadrature rules were almost alike and that the simulations in the former case are faster due to fewer quadrature points. Since the *max-ent* scheme allows for heat conduction, we perform the tests at two different indentation velocities. The first test is performed under locally adiabatic conditions, while the second is performed at a finite indentation velocity. The description of the tests and the results are provided below.

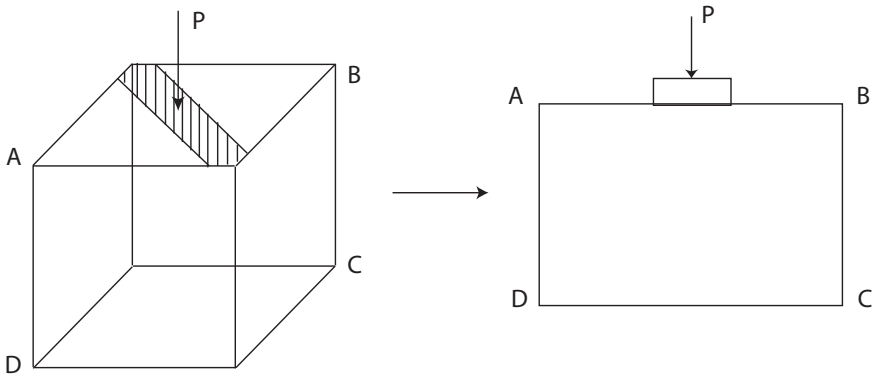

Figure 5.22: Geometry of the nanoindentation setup for a rectangular indenter.

Test problem definition

The sample is the same as used in the previous nanoindentation example, consisting of 137,313 atoms. The indenter is a rigid flat punch and is applied along one of the diagonals of the top surface of the cube, as shown in Figure 5.22. Since the [111] planes are the preferred slip planes, the dislocations may be observed conveniently in the [110] plane, denoted by ABCD in Figure 5.22. The initial mesh comprises of atomistic region only in the vicinity of the indenter and has 3506 representative atoms. A cross-section of the initial triangulation is shown in Figure 5.23. The boundary conditions imposed on the lateral and bottom surfaces are the same as before. The indenter is applied as displacement boundary conditions on a strip of atoms on the top surface corresponding to the width of the punch.

In our calculations, we used the following parameters for the punch:

$$W = 9\,[\sigma],\ \ \delta = -0.1\,[\sigma]\,.$$

Before the indentation process, the cube is allowed to equilibrate isothermally at a uniform temperature of $T = 0.5T_m$. On this sample, the adiabatic test is performed by specifying $\triangle t = 0$, which is corresponds to high speed indentation. The second test is performed at $\triangle t = 50\,[\kappa\sigma/k_B]$, which is equivalent to a time step of 17.4 ps. This allows the heat to diffuse through the cube. The indenter velocity may be calculated as

$$V = \frac{\delta}{\triangle t} = 1.95 \text{ m/s}\,. \tag{5.17}$$

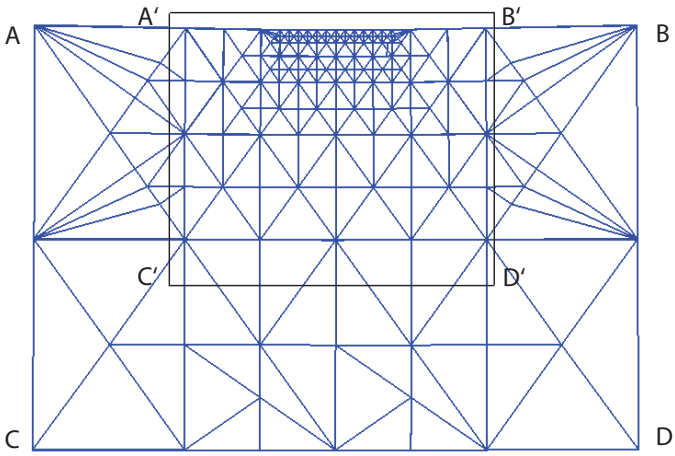

Figure 5.23: Initial mesh for the nanoindentation test with rectangular indenter. A'B'C'D' is the region shown in the snapshots of the temperature evolution.

Discussion

Figures 5.25 and 5.26 show the snapshots of the temperature profile under the indenter for the adiabatic test, whereas Figure 5.27 shows images of the temperature in the test with heat conduction, i.e., with a non-zero time step. Figure 5.24 presents a comparison of the

force versus indenter depth curves for the two cases. A qualitative discussion of the results is as follows.

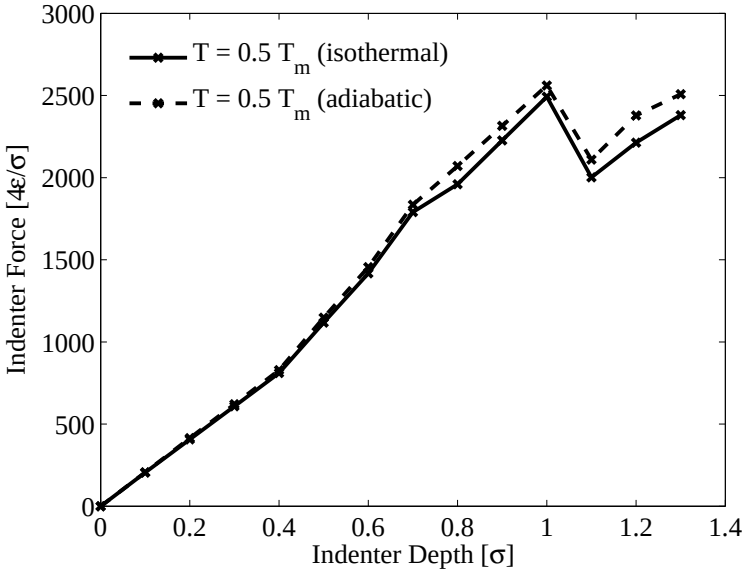

Figure 5.24: Force versus indenter depth plot for a rectangular indenter using the *max-ent* approach under adiabatic and isothermal conditions.

- Based on Figures 5.25 and 5.26, we observe the evolution of temperature as the indentation proceeds in the adiabatic case. In the last image in Figures 5.26, when the indenter depth is $-0.12\,[\sigma]$, the temperature under the edges of the punch is $0.6\,T_m$, which is a 20 % rise from the prescribed temperature. This is significantly less than that observed with the WKB method, but is expected. Since the anharmonicity of the potential is accounted for here, these results should be more accurate. It would be insightful to compare the results of this study based on molecular dynamics simulations.

- The heating under the edges of the indenter is expected. In addition, we note that this hot region spreads out along the (111) plane as the dislocation propagates. However, the significant temperature difference at the dislocation core needs further investiga-

tion. It is probable that the temperature difference is mediated by the deformation field above and below the slip plane. Furthermore, since the test is adiabatic, the system is unable to diffuse the heat generated. However, we also observe that the slip plane ends where the coarse-grained region begins, which may be a potential source of numerical error. This limitation may be rectified by lowering the refinement tolerance and by allowing the system to equilibrate and remesh at the same load.

- Figure 5.24 indicates a negligible variation in the force indenter curve for the adiabatic and isothermal cases. We also note that the dislocation nucleation occurs at the same indenter depth for both speeds. Furthermore, unlike in the case of spherical indenter, the drop in the force is much more pronounced due to higher stress concentration caused by the sharp edges.

- Figure 5.27 shows the temperature profile under the indenter when heat can diffuse through the crystal. The negligible change in temperature implies that the indentation speed is slow enough to allow dissipation of the heat generated locally. In other words, the time step used in the test is such that the indenter velocity is less than the critical velocity for the material, thereby making the process isothermal. We use the diffusivity, D, of solid Ar and the lattice constant specified in 5.14 to evaluate the critical velocity as

$$V_c = \frac{D}{a} = 17.3 \text{ m/s}\,, \tag{5.18}$$

  which confirms that the indentation velocity used is in the isothermal range since $V < V_c$.

- Finally, we note that the time step of 17.4 ps is about 1800 times larger than a typical time step used molecular dynamics simulations. This demonstrates that the

proposed method for modelling non-equilibrium phenomena using the quasicontinuum framework does not impose any limitations on the time step. Thereby, it facilitates the simulation of the entire spectrum of thermodynamic processes, ranging from very slow or isothermal processes to processes that are fast but may still be modelled by neglecting the inertial or dynamic effects.

- Figure 5.28 shows the dislocation structure under a rectangular indenter. As expected, we observe that the first partial dislocation is emitted along the (111) plane followed by a stacking fault ribbon. Since the nearest-neighbor Lennard-Jones potential has zero stacking fault energy, we do not observe a second partial dislocation. Moreover, the stacking fault grows in size as the indentation proceeds. As observed in Figures 5.26 and 5.27, the slip creates a step at the top surface of the crystal.

This concludes the presentation of our results that serve to validate the methods developed in this work as well as demonstrate their applicability. The results for the nanoindentation tests described here are illustrative and preliminary, and we intend to investigate them further using the non-equilibrium finite temperature QC developed here.

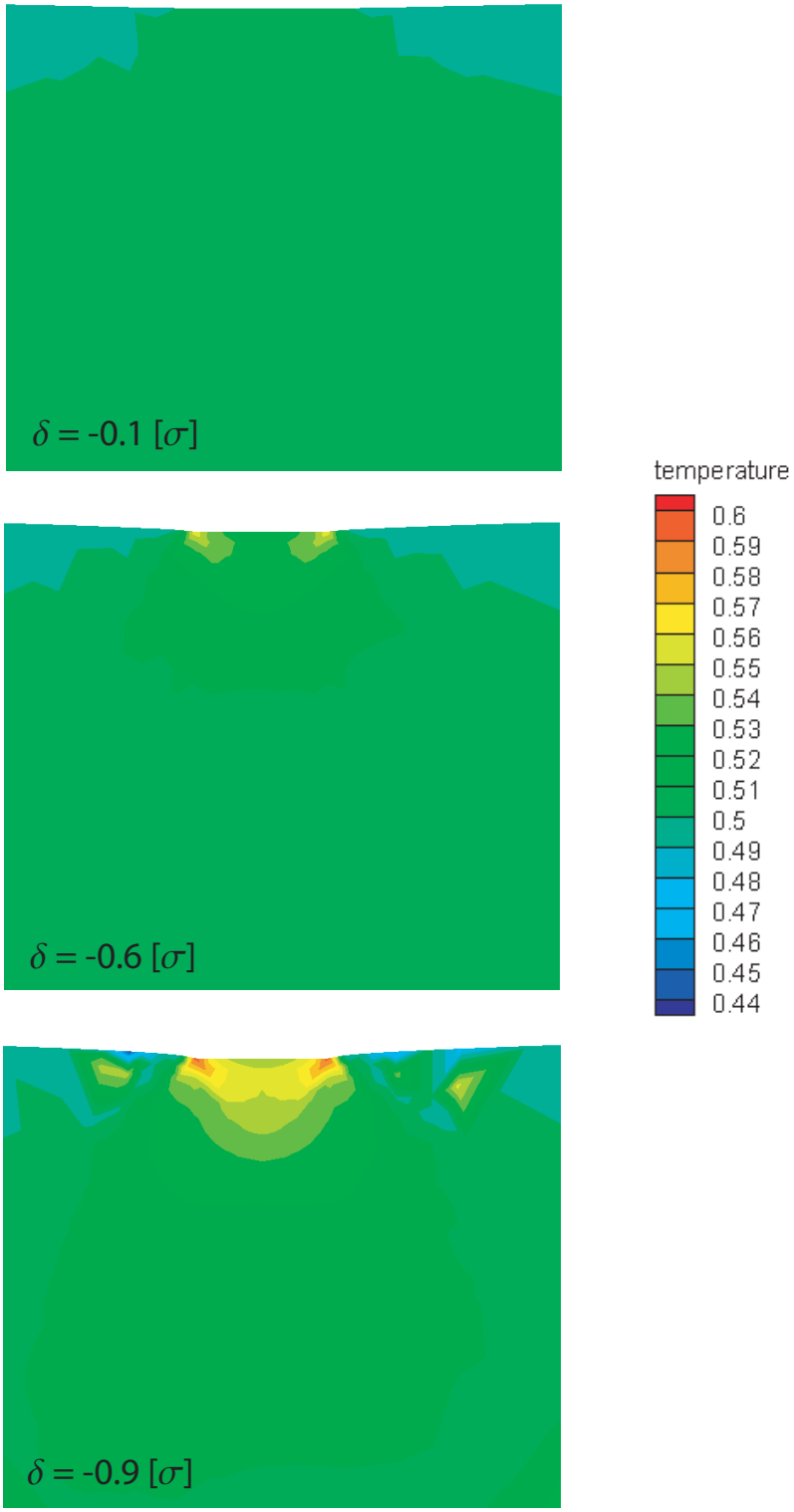

Figure 5.25: Snapshots showing the temperature profile of a section under the indenter at different indentation depths during the simulation. The test is performed using the *max-ent* approach under adiabatic conditions.

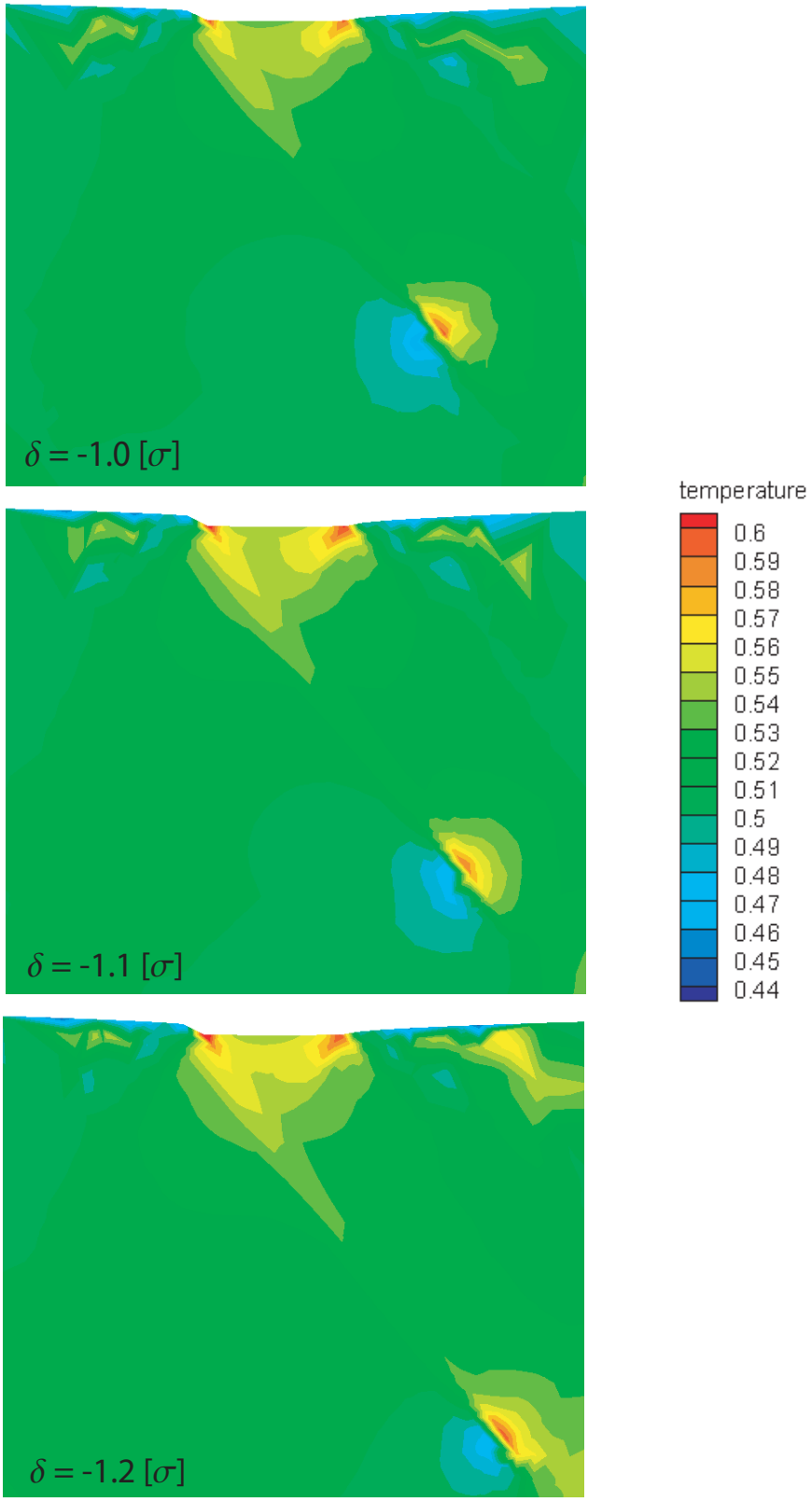

Figure 5.26: Snapshots at subsequent load increments showing the temperature profile under the indenter after a dislocation has nucleated. The test is performed using the *max-ent* approach under adiabatic conditions.

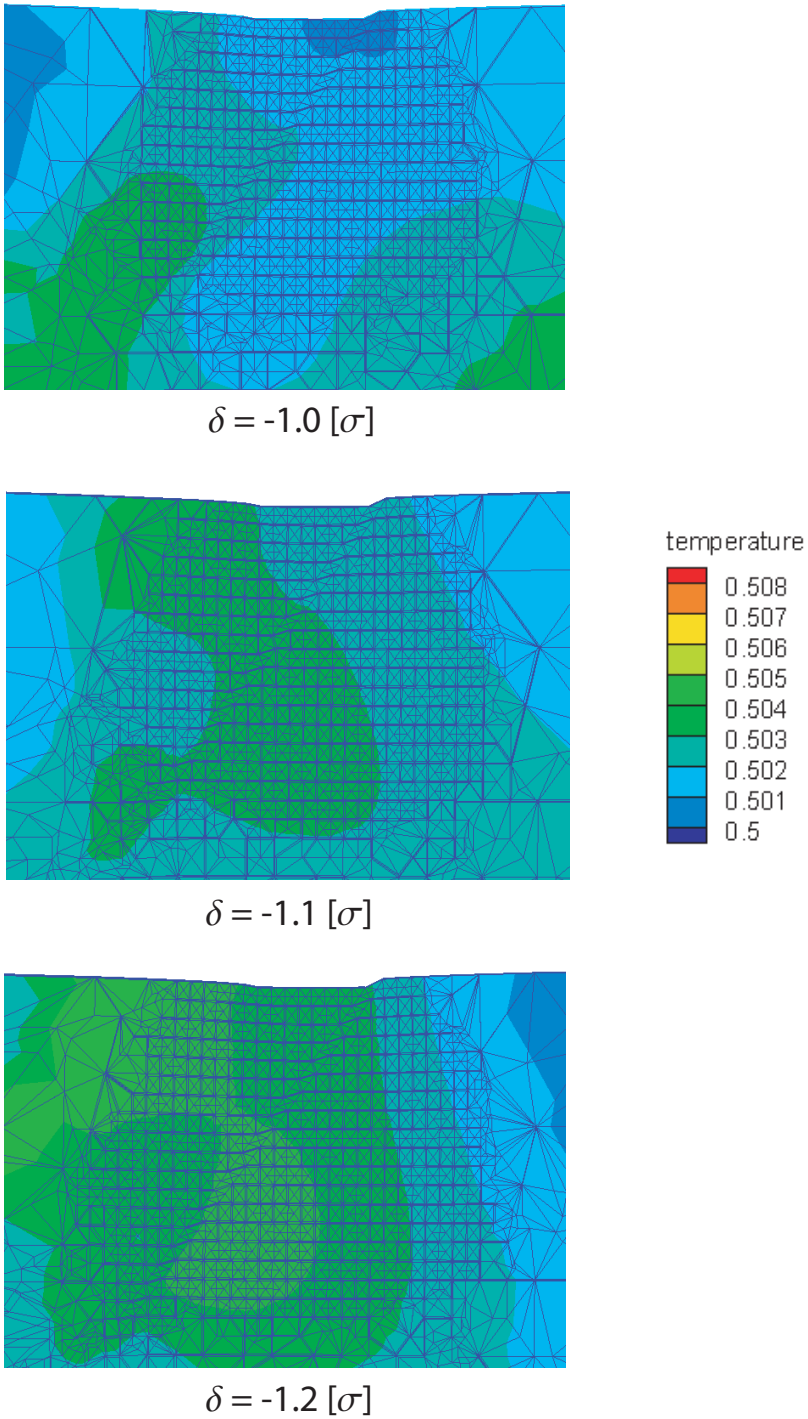

Figure 5.27: Snapshots at subsequent load increments showing the temperature profile under the indenter after a dislocation has nucleated. The test is performed using the *max-ent* approach with heat conduction. The negligible variation in temperature shows that the conditions are isothermal.

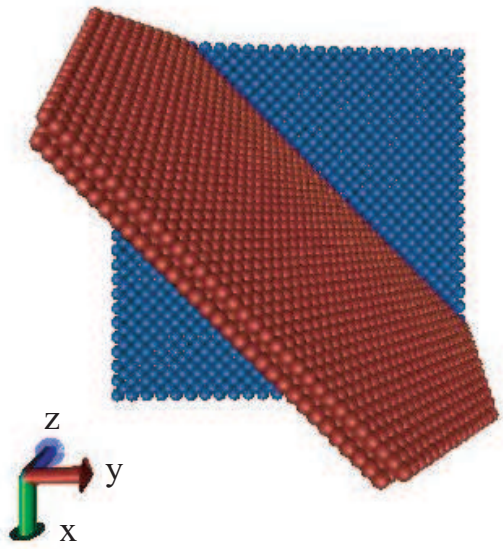

Figure 5.28: Dislocation structure under a rectangular indenter predicted by the quasicontinuum method at indentation depth $\delta = 1.2[\sigma]$ under adiabatic conditions. The figure displays the energetic atoms (red) under the top surface of the crystal (blue).

Chapter 6

Concluding remarks and future directions

Before closing, we summarize the primary accomplishments of this thesis and discuss some of the limitations and potential directions for future investigations.

This work proposes two computational methods for deriving thermodynamic potentials by systematically averaging over the atomistic dynamics, or the thermal motion of atoms. These approximation schemes essentially achieve a homogenization on the temporal scale, thereby facilitating the simulation of quasistatic processes and systems in thermodynamic equilibrium. The main advantage of the methods over atomistic models such as molecular dynamics lies in the elimination of the need to keep track of all the degrees of freedom in the system. Nevertheless, in the spirit of the quasicontinuum theory, all input regarding the behavior of the atoms is purely atomistic. Furthermore, both methods are very general and may be applied to any material and crystal structure given an appropriate interaction potential. We recall that the *max-ent* approach furnishes a Gaussian probability distribution function, which can account for the anharmonicity of the interatomic potential in the macroscopic energy of the system up to 5^{th} order for pairwise interactions, and 3^{rd} order for many-body interactions. Our results predict that this leads to a significant improvement over many methods based on the canonical distribution from statistical mechanics, which

require the local quasi-harmonic approximation for numerical implementation especially for very large systems. Thus, the *max-ent* method is capable of modelling material behavior at high temperatures, even close to the melting point of the material, where the harmonic approximation fails.

The macroscopic energy functionals, derived in Chapters 2 and 4, provide a natural way of formulating a finite temperature version of the quasicontinuum theory. We recall that the energy functionals obtained after the *max-ent* or the WKB treatment are functions of the state variables only. For instance, the free energy is a function of the mean atomic positions, the temperature, and the mean field parameters, in the case of the *max-ent* approach. Then, for quasistatic processes such as thermal expansion, or isothermal nanoindentation, the problem of determining the metastable equilibrium configurations of the system is equivalent to the minimization of the free energy over appropriate state variables. The solution to this minimization problem is effectively achieved by using the quasicontinuum framework, which facilitates a spatial coarse-graining of the atomistic description. In Chapter 3, we also propose an extension of the finite temperature quasicontinuum theory, based on the work of Yang et al. [44], to model non-equilibrium thermodynamic processes such as heat conduction through the system. The variational formulation is developed by constructing a joint incremental energy functional whose Euler-Lagrange equations yield the equilibrium equations as well as the time-discretized heat equation. This version, in conjunction with the existing features of the quasicontinuum method, possesses several capabilities desired in a computational tool for material modelling. The most notable is the ability to simulate microstructural evolution along with the associated thermo-mechanical coupled behavior of the material. Another advantageous feature is the flexibility regarding the choice of a time-step. Since the rate problem is treated as an incremental minimization problem on

the macro-scale with the energy of the phonons already accounted for, the time step is not restricted by the scale of the atomic oscillations. Moreover, we use the backward Euler finite difference scheme for the time-discretization, which is unconditionally stable. This provides the *max-ent* method the flexibility to simulate thermodynamic processes that may be very slow or isothermal and, hence, beyond the reach of atomistic models such as molecular dynamics. These features are demonstrated qualitatively by the nanoindentation tests presented in Chapter 5. Furthermore, being a seamless multiscale method, the quasicontinuum method does not involve an interface separating the fine and the coarse-grained regions, unlike many other multiscale methods which require additional artifacts or special treatment of the boundary at finite temperature.

Apart from the above features, it is vital to bear in mind the limitations born out of the approximations made in the work. Many of them also make challenging problems for future research. Due to the use of the quasi-harmonic approximation, the method based on formal asymptotics is restricted to reasonably low temperatures where the anharmonic effects as well as the quantum effects may be negligible. Furthermore, it is suitable only for locally adiabatic conditions, that is, for processes that are so fast that there is not sufficient time for the atoms to exchange heat with their environment. Consequently, this method does not support heat transport through the system. The *max-ent* method uses Gauss quadrature to compute phase averages of the atomistic system approximately, which is a source of numerical error. Hence, as suggested by the results for bulk properties, it is important to perform a convergence study in order to determine the optimal degree of quadrature rule depending on whether the interatomic potential involves only pairwise terms or many-body interaction terms. The results in Chapter 5 indicate that the 3^{rd} degree quadrature rule suffices for the embedded-atom method which involves many-body interactions whereas,

the Lennard-Jones pair potential requires the 5^{th} degree formula at high temperatures. The entire work is based on the local thermal equilibrium assumption in addition to the quasistatic assumption for macroscopic processes. Thus, it assumes the existence of two relaxation times – the relaxation time for the establishment of statistical equilibrium in the whole system and another, much shorter, for establishing equilibrium within a small cell in the domain. Furthermore, in many problems, it may be insightful or sometimes essential to model the actual dynamics of the atoms in the localized regions of high activity. For instance, in order to model adiabatic or very fast processes, it is important to take the inertial effects into account. However, the quasicontinuum theory described in this work can model only quasistatic processes. Thus, coupling of atomistic models such as molecular dynamics with finite temperature QC presents a worthwhile direction for future research. Such a problem would involve the modelling of the conversion between phonons in the atomistic region and heat in the coarse-grained region. A possible way of achieving this is provided by the *max-ent* method, which introduces the mean atomic momenta as additional variables. The equilibrium equations can then be replaced by the Hamilton's equations in order to model a dynamic problem. One of the remaining challenges in using the QC framework for dynamic processes, which is essentially a numerical one, is the problem of spurious reflections of the high frequency waves at the fine-coarse interface as they cannot propagate into the coarse regions.

Among the short term goals, we wish to pursue the validations tests further, especially for the heat conduction and the nanoindentation tests. We wish to investigate the effect of surfaces on the heat conductivity of nanowires and compare with experimental observations. We intend to continue the nanoindentation test for a range of temperatures and a range of indenter velocities in order to quantitatively study their effect on dislocation nucleation

and heat diffusion through the crystal. We also aim to simulate these tests for materials with more complex interaction potentials such as the embedded-atom method for pure metals. The tests demonstrated here also serve to indicate other interesting applications such as failure of a nanowire with a geometric defect under tension and void growth at finite temperature.

As noted earlier, the interatomic potential introduces empiricism into the model. The Fourier law of heat conduction, which is appended to the equilibrium equations, is also a phenomenological relation. Thus, the method depends significantly on these empirical factors for accurately predicting material response at finite temperature. Since phonon-phonon interactions, accounted for by the anharmonicity of the interaction potential, is understood to facilitate heat or energy transport, the possibility of deriving heat conduction directly from the atomistic dynamics by considering the anharmonic terms using the *max-ent* approach is a problem worth exploring. Finally, the idea of appending additional empirical models through the energy functional opens a possible avenue for incorporating additional physics such as mass diffusion and electrical-thermo-mechanical coupling into the theory of the quasicontinuum.

Appendix A

Calculations for some interaction potentials

The following sections describe the details of the calculations for the two empirical interatomic potentials used in this work, namely, the Lennard-Jones pair potential and the Sutton-Chen form of many-body potentials. The analytical expressions for the interaction potentials, the corresponding energy of the crystal, the force on each atom, the dynamical matrix of each atom based on the local quasi-harmonic approximation, and the derivative of its trace are presented.

A.1 Lennard-Jones potential

The Lennard-Jones pair potential has the form

$$\phi(r) = 4\varepsilon \left[\left(\frac{\sigma}{r}\right)^{12} - 2\left(\frac{\sigma}{r}\right)^{6} \right], \tag{A.1}$$

where r is the interatomic distance, σ is the first nearest neighbor distance at equilibrium at zero temperature, and -4ε is the corresponding energy of the bond in that state. For

solid Argon, the parameters have the following values:

$$\sigma = 0.34\ nm,\ \ 4\epsilon = 0.0104\ eV\,. \tag{A.2}$$

The total potential energy of the crystal is

$$V = \sum_{a=1}^{N} \frac{1}{2} \sum_{b} \phi(r_{ab})\,. \tag{A.3}$$

The summation over b excludes the case where $a = b$. The force experienced by atom a is given by

$$\frac{\partial V}{\partial \boldsymbol{q}_a} = \sum_{b} \phi'(r_{ab}) \frac{\boldsymbol{r}_{ab}}{r_{ab}}\,, \tag{A.4}$$

where

$$\frac{\partial r_{ab}}{\partial \boldsymbol{q}_a} = \frac{1}{2r_{ab}} \frac{\partial}{\partial \boldsymbol{q}_a}\, \boldsymbol{r}_{ab} \cdot \boldsymbol{r}_{ab} = \frac{1}{r_{ab}} \boldsymbol{r}_{ab} \tag{A.5}$$

with

$$\boldsymbol{r}_{ab} = \boldsymbol{q}_a - \boldsymbol{q}_b\,.$$

Differentiating A.4 again with respect to $\boldsymbol{q}_a$ gives the 3×3 dynamical matrix, K_a, associated with the atom a as

$$\frac{\partial^2}{\partial \boldsymbol{q}_a \partial \boldsymbol{q}_a} V = \sum_{b} \left[\frac{\phi'(r_{ab})}{r_{ab}} \delta + \left(\phi''(r_{ab}) - \frac{\phi'(r_{ab})}{r_{ab}} \right) \frac{1}{r_{ab}^2} \boldsymbol{r}_{ab} \otimes \boldsymbol{r}_{ab} \right]\,, \tag{A.6}$$

δ being the 3×3 identity tensor. Consequently, the trace of the stiffness matrix is computed as

$$\mathrm{Tr}\,\mathrm{K}_a = \sum_{b} \left[\phi''(r_{ab}) + 2 \frac{\phi'(r_{ab})}{r_{ab}} \right] \tag{A.7}$$

. In the quasi-harmonic case, the local stiffness matrices are not constants, but depend on the macroscopic deformation of the crystal. Taking partial derivative of the traces of K_a and K_b with respect to $\boldsymbol{q}_a$, respectively, yields

$$\frac{\partial}{\partial \boldsymbol{q}_a}\mathrm{Tr}\,\boldsymbol{K}_a = \sum_b \left[\phi'''(r_{ab}) + 2\frac{\phi''(r_{ab})}{r_{ab}} - 2\frac{\phi'(r_{ab})}{r_{ab}^2}\right]\frac{\boldsymbol{r}_{ab}}{r_{ab}} \tag{A.8a}$$

$$\frac{\partial}{\partial \boldsymbol{q}_a}\mathrm{Tr}\,\boldsymbol{K}_b = \left[\phi'''(r_{ab}) + 2\frac{\phi''(r_{ab})}{r_{ab}} - 2\frac{\phi'(r_{ab})}{r_{ab}^2}\right]\frac{\boldsymbol{r}_{ab}}{r_{ab}}\,. \tag{A.8b}$$

A.2 EAM-Johnson potential

The embedded-atom method is an empirical many body potential developed for modelling the behavior of fcc transition metals ([7], [18]). The total potential energy of the crystal is given as

$$V = \sum_{a=1}^{N}\left[\frac{D}{2}\sum_b \phi(r_{ab}) + F(\rho_a)\right]\,, \tag{A.9}$$

where the first term is a pairwise repulsive term, while the second represents a density dependent cohesion term known as the embedding function. In our calculations, we use the analytical forms for these functions proposed in the work of Johnson [18].

$$\phi(r) = \phi_e \exp[-\gamma(\frac{r}{r_e} - 1)] \tag{A.10a}$$

$$F(\rho) = -E_c\left[1 - \frac{\alpha}{\beta}\ln\frac{\rho}{\rho_e}\right](\frac{\rho}{\rho_e})^{\alpha/\beta} - \Phi_e(\frac{\rho}{\rho_e})^{\gamma/\beta} \tag{A.10b}$$

$$\rho_a = \sum_b f(r_{ab}) \tag{A.10c}$$

$$f(r) = f_e \exp[-\beta(\frac{r}{r_e} - 1)]\,, \tag{A.10d}$$

where r_e and ρ_e are, respectively, the nearest neighbor distance and the density at equilibrium at 0 K. α, β, γ, ϕ_e, E_c and f_e are material parameters optimized by fitting material properties such as cohesive energy and bulk modulus at 0 K. For Cu, the parameters have the following values:

$$\begin{aligned} &a = 0.361\ nm,\ \ E_c = 3.54\ eV,\ \ \phi_e = 0.59\ eV \\ &\alpha = 5.09,\ \ \beta = 5.85,\ \ \gamma = 8.00\,. \end{aligned} \tag{A.11}$$

The force experienced by each atom is, then, given by

$$\begin{aligned} \frac{\partial V}{\partial \boldsymbol{q}_a} &= \frac{\partial F}{\partial \boldsymbol{q}_a}(\rho_a) + \sum_b \frac{\partial F}{\partial \boldsymbol{q}_a}(\rho_b) + \sum_b \frac{\partial}{\partial \boldsymbol{q}_a}\phi(r_{ab}) \\ &= F'(\rho_a)\frac{\partial \rho_a}{\partial \boldsymbol{q}_a} + \sum_b F'(\rho_b)\frac{\partial \rho_b}{\partial \boldsymbol{q}_a} + \sum_b \phi'(r_{ab})\frac{\partial r_{ab}}{\partial \boldsymbol{q}_a} \\ &= \sum_b \left\{ \left[F'(\rho_a) + F'(\rho_b)\right] f'(r_{ab}) + \phi'(r_{ab}) \right\} \frac{\boldsymbol{r}_{ab}}{r_{ab}}\,, \end{aligned} \tag{A.12a}$$

where

$$\frac{\partial \rho_a}{\partial \boldsymbol{q}_a} = \sum_b f'(r_{ab})\frac{\partial r_{ab}}{\partial \boldsymbol{q}_a}, \quad \frac{\partial \rho_b}{\partial \boldsymbol{q}_a} = f'(r_{ab})\frac{\partial r_{ab}}{\partial \boldsymbol{q}_a} \tag{A.13}$$

and

$$\frac{\partial r_{ab}}{\partial \boldsymbol{q}_a} = \frac{1}{2r_{ab}}\frac{\partial}{\partial \boldsymbol{q}_a}\,\boldsymbol{r}_{ab}\cdot\boldsymbol{r}_{ab} = \frac{1}{r_{ab}}\boldsymbol{r}_{ab} \tag{A.14}$$

with

$$\boldsymbol{r}_{ab} = \boldsymbol{q}_a - \boldsymbol{q}_b\,.$$

The summations over b exclude the case where $a = b$. The 3×3 dynamical matrix, K_a, associated with each atom a has the form

$$\begin{aligned}\frac{\partial^2}{\partial \boldsymbol{q}_a \partial \boldsymbol{q}_a} V = {} & F''(\rho_a) \left[\sum_c f'(r_{ac}) \frac{\boldsymbol{r}_{ac}}{r_{ac}} \right] \otimes \left[\sum_b f'(r_{ab}) \frac{\boldsymbol{r}_{ab}}{r_{ab}} \right] \\ & + \sum_b F''(\rho_b) [f'(r_{ab})]^2 \frac{1}{r_{ab}^2} \boldsymbol{r}_{ab} \otimes \boldsymbol{r}_{ab} \\ & + \sum_b [F'(\rho_a) + F'(\rho_b)\,] \left[\frac{f'(r_{ab})}{r_{ab}} \delta + \left(f''(r_{ab}) - \frac{f'(r_{ab})}{r_{ab}} \right) \frac{1}{r_{ab}^2} \boldsymbol{r}_{ab} \otimes \boldsymbol{r}_{ab} \right] \\ & + \sum_b \left[\frac{\phi'(r_{ab})}{r_{ab}} \delta + \left(\phi''(r_{ab}) - \frac{\phi'(r_{ab})}{r_{ab}} \right) \frac{1}{r_{ab}^2} \boldsymbol{r}_{ab} \otimes \boldsymbol{r}_{ab} \right] .\end{aligned} \tag{A.15}$$

The trace of the stiffness matrix is of the form

$$\begin{aligned}\operatorname{Tr} \boldsymbol{K}_{aa} = {} & \sum_b \left[\phi''(r_{ab}) + 2 \frac{\phi'(r_{ab})}{r_{ab}} \right] \\ & + \sum_b F''(\rho_b)\, [f'(r_{ab})]^2 + \sum_b F''(\rho_a) f'(r_{ab}) \left\{ \sum_c f'(r_{ac}) \frac{\boldsymbol{r}_{ac}}{r_{ac}} \right\} \cdot \frac{\boldsymbol{r}_{ab}}{r_{ab}} \\ & + \sum_b [F'(\rho_a) + F'(\rho_b)\,] \left[f''(r_{ab}) + 2 \frac{f'(r_{ab})}{r_{ab}} \right] .\end{aligned} \tag{A.16}$$

Differentiating the trace of $\boldsymbol{K}_a$ with respect to $\boldsymbol{q}_a$ yields

$$
\begin{aligned}
\frac{\partial}{\partial \boldsymbol{u}_a}\mathrm{Tr}\,\boldsymbol{K}_a = &\sum_b \left[\phi'''(r_{ab}) + 2\frac{\phi''(r_{ab})}{r_{ab}} - 2\frac{\phi'(r_{ab})}{r_{ab}^2}\right]\frac{\boldsymbol{r}_{ab}}{r_{ab}} \\
&+ \sum_b [F'(\rho_a) + F'(\rho_b)]\left[f'''(r_{ab}) + 2\frac{f''(r_{ab})}{r_{ab}} - 2\frac{f'(r_{ab})}{r_{ab}^2}\right]\frac{\boldsymbol{r}_{ab}}{r_{ab}} \\
&+ \sum_b 2F''(\rho_b)\, f''(r_{ab}) f'(r_{ab})\frac{\boldsymbol{r}_{ab}}{r_{ab}} \\
&+ \sum_b F''(\rho_b) f'(r_{ab})\left[f''(r_{ab}) + 2\frac{f'(r_{ab})}{r_{ab}}\right]\frac{\boldsymbol{r}_{ab}}{r_{ab}} \\
&+ \sum_b F'''(\rho_b)[f'(r_{ab})]^3\frac{\boldsymbol{r}_{ab}}{r_{ab}} \\
&+ \sum_b F''(\rho_a)\left[f''(r_{ab}) + 2\frac{f'(r_{ab})}{r_{ab}}\right]\left\{\sum_c f'(r_{ac})\frac{\boldsymbol{r}_{ac}}{r_{ac}}\right\} \\
&+ \sum_b F'''(\rho_a)\left[\left\{\sum_c f'(r_{ac})\frac{\boldsymbol{r}_{ac}}{r_{ac}}\right\}\cdot\left\{\sum_c f'(r_{ac})\frac{\boldsymbol{r}_{ac}}{r_{ac}}\right\}\right] f'(r_{ab})\frac{\boldsymbol{r}_{ab}}{r_{ab}} \\
&+ \sum_b 2F''(\rho_a)\left[\sum_c \left\{\frac{f'(r_{ac})}{r_{ac}}\delta + \left(f''(r_{ac}) - \frac{f'(r_{ac})}{r_{ac}}\right)\frac{1}{r_{ac}^2}\boldsymbol{r}_{ac}\otimes\boldsymbol{r}_{ac}\right\}\right] f'(r_{ab})\frac{\boldsymbol{r}_{ab}}{r_{ab}}\,.
\end{aligned}
\tag{A.17}
$$

Differentiating the trace of $\boldsymbol{K}_b$ with respect to $\boldsymbol{q}_a$, b being a neighbor of atom a, yields

$$
\begin{aligned}
\frac{\partial}{\partial \boldsymbol{u}_a}\mathrm{Tr}\,\boldsymbol{K}_b = &\left[\phi'''(r_{ab}) + 2\frac{\phi''(r_{ab})}{r_{ab}} - 2\frac{\phi'(r_{ab})}{r_{ab}^2}\right]\frac{\boldsymbol{r}_{ab}}{r_{ab}} \\
&+ [F'(\rho_a) + F'(\rho_b)\,]\left[f'''(r_{ab}) + 2\frac{f''(r_{ab})}{r_{ab}} - 2\frac{f'(r_{ab})}{r_{ab}^2}\right]\frac{\boldsymbol{r}_{ab}}{r_{ab}} \\
&+ 2F''(\rho_a)\, f''(r_{ab}) f'(r_{ab})\frac{\boldsymbol{r}_{ab}}{r_{ab}} \\
&+ F''(\rho_b) f'(r_{ab})\left[\sum_c \{f''(r_{bc}) + 2\frac{f'(r_{bc})}{r_{bc}}\}\right]\frac{\boldsymbol{r}_{ab}}{r_{ab}} \\
&+ F'''(\rho_b) f'(r_{ab})\left[\left\{\sum_c f'(r_{bc})\frac{\boldsymbol{r}_{bc}}{r_{bc}}\right\}\cdot\left\{\sum_c f'(r_{bc})\frac{\boldsymbol{r}_{bc}}{r_{bc}}\right\}\right]\frac{\boldsymbol{r}_{ab}}{r_{ab}} \\
&- 2F''(\rho_b)\left(f''(r_{ab}) - \frac{f'(r_{ab})}{r_{ab}}\right)\left[\left\{\sum_c f'(r_{bc})\frac{\boldsymbol{r}_{bc}}{r_{bc}}\right\}\cdot\frac{\boldsymbol{r}_{ab}}{r_{ab}}\right]\frac{\boldsymbol{r}_{ab}}{r_{ab}} \\
&- 2F''(\rho_b)\frac{f'(r_{ab})}{r_{ab}}\left\{\sum_c f'(r_{bc})\frac{\boldsymbol{r}_{bc}}{r_{bc}}\right\} \\
&+ F''(\rho_a)[f''(r_{ab}) + 2\frac{f'(r_{ab})}{r_{ab}}]\left\{\sum_c f'(r_{ac})\frac{\boldsymbol{r}_{ac}}{r_{ac}}\right\} \\
&+ F'''(\rho_a)[f'(r_{ab})]^2\left\{\sum_c f'(r_{ac})\frac{\boldsymbol{r}_{ac}}{r_{ac}}\right\} \\
&+ \sum_d F'''(\rho_d) f'(r_{ad})[f'(r_{ab})]^2\frac{\boldsymbol{r}_{ad}}{r_{ad}} \\
&+ \sum_d F''(\rho_d) f'(r_{ad})\left[f''(r_{bd}) + 2\frac{f'(r_{bd})}{r_{bd}}\right]\frac{\boldsymbol{r}_{ad}}{r_{ad}}\,.
\end{aligned}
\tag{A.18}
$$

The last two terms include the contributions from those neighbors of b, which are also neighbors of a and we denote them by d.

A.3 Sutton-Chen potential

This is another empirical many-body potential developed for fcc transition metals by Sutton and Chen [37]. Since the potential energy in the case of the embedded-atom method has the same form as Eq. (A.9), all expressions derived in section A.2 remain valid. Only the

analytical forms given in Eqs. (A.10a-A.10d) are replaced by the following:

$$\phi(r) = D\left(\frac{\sigma}{r}\right)^n \tag{A.19a}$$

$$F(\rho_a) = -Dc_a\sqrt{\rho_a} \tag{A.19b}$$

$$\rho_a = \sum_b f(r_{ab}) \tag{A.19c}$$

$$f(r) = \left(\frac{\sigma}{r}\right)^m , \tag{A.19d}$$

where σ is the lattice constant for the metal at 0 K. The parameters D, c, m, and n are optimized to fit material properties such as the cohesive energy and the bulk modulus at 0 K. For Cu, the parameters have the following values:

$$\begin{aligned} &a = 0.361\ nm,\ \ D = 0.012382\ eV, \\ &c = 39.432,\ \ m = 6,\ \ n = 9\,. \end{aligned} \tag{A.20}$$

Appendix B

Gauss Quadrature for multiple integrals

This appendix presents a brief summary of the third and fifth degree quadrature rules for multiple integrals in a space of dimension n used in our calculations. The expressions and the quadrature tables were obtained from the work of A. H. Stroud [36]. In particular, we are interested in the following integrals with gaussian weighting functions:

$$I(f) = \int_{-\infty}^{\infty} \cdots \int_{-\infty}^{\infty} f(x_1, \ldots, x_n) \, \exp[-x_1^2 - \cdots - x_n^2] dx_1 \ldots dx_n \, . \tag{B.1}$$

An M-point numerical quadrature approximates the integral as

$$I(f) \approx \sum_{k=1}^{M} f(\nu_k) W_k \, , \tag{B.2}$$

where ν_k is an n-dimensional vector at the k^{th} quadrature point:

$$\nu_k = \nu_{1k}, \ldots, \nu_{nk} \, .$$

The expressions for the quadrature points and the associated weights are given below.

B.1 Third degree quadrature

This formula has $2n$ points. The points and coefficients are obtained by requiring that the formula should integrate all monomials of degree ≤ 3 exactly. Since the domain of integration is $\mathbb{R}^n$ and the gaussian weight has the property

$$w(\boldsymbol{x}) = w(-\boldsymbol{x})\,,$$

the distribution of quadrature points is assumed to be fully symmetric. That is, we assume that the formula consists of $2n$ points ν_k and $-\nu_k$ and that the coefficient of ν_k equals that of $-\nu_k$. Thus, for an n-dimensional space, the points are

$$\begin{aligned}
&(\pm r, 0, \ldots, 0)\\
&\vdots\\
&(0, \ldots, 0, \pm r)
\end{aligned}$$

with the coefficient

$$W_k = \frac{1}{2n} V, \;\; k = 1, \ldots, n\,,$$

where

$$V = I(1) = \pi^{n/2}, \;\; r^2 = \frac{n}{2}\,. \tag{B.4}$$

B.2 Fifth degree quadrature

This formula has n^2+n+2 points. The formula is obtained by requiring that it be exact for all monomials of degree ≤ 5. Owing to the symmetry of the domain, the formula consists of

$\frac{1}{2}(n^2+n+2)$ points ν_k and their negatives, $-\nu_k$. The coefficient of ν_k equals that of $-\nu_k$. For an n-dimensional space, the 5^{th} degree quadrature points and their coefficients can be written as follows using 8 parameters:

$$
\begin{aligned}
&(\eta, \eta, \ldots, \eta, \eta) \quad A \\
&(\lambda, \xi, \ldots, \xi, \xi) \quad B \\
&\vdots \\
&(\xi, \xi, \ldots, \xi, \lambda) \quad B \\
&(\mu, \mu, \gamma, \ldots, \gamma) \quad C \\
&(\mu, \gamma, \mu, \ldots, \gamma) \quad C \\
&\vdots \\
&(\gamma, \ldots, \gamma, \mu, \mu) \quad C \\
&(-\eta, -\eta, \ldots, -\eta, -\eta) \quad A \\
&(-\lambda, -\xi, \ldots, -\xi, -\xi) \quad B \\
&\vdots \\
&(-\xi, -\xi, \ldots, -\xi, -\lambda) \quad B \\
&(-\mu, -\mu, -\gamma, \ldots, -\gamma) \quad C \\
&(-\mu, -\gamma, -\mu, \ldots, -\gamma) \quad C \\
&\vdots \\
&(-\gamma, \ldots, -\gamma, -\mu, -\mu) \quad C\,.
\end{aligned}
$$

The values of the eight parameters for different dimensions are provided in [35].

Appendix C

The WKB approximation

The WKB method is a perturbation technique for obtaining approximate global solutions to linear differential equations whose highest derivative is multiplied by a small parameter ϵ. The WKB approximation for such singularly perturbed problems is illustrated using the following example from [2]. Consider the ODE

$$\epsilon^2 \ddot{y}(t) + \omega^2(t) y(t) = 0\,. \tag{C.1}$$

We wish to ascertain the asymptotic behavior of the solutions in the limit of $\epsilon \to 0$. The formal WKB expansion is

$$y(t) \sim \exp\left(\epsilon^{-1} \sum_{n=0}^{\infty} \epsilon^n S_n(t)\right)\,. \tag{C.2}$$

The first and the second derivatives of $y(t)$ are

$$\dot{y}(t) \sim \epsilon^{-1} \left(\sum_{n=0}^{\infty} \epsilon^n \dot{S}_n(t)\right) \exp\left(\epsilon^{-1} \sum_{n=0}^{\infty} \epsilon^n S_n(t)\right) \tag{C.3a}$$

$$\ddot{y}(t) \sim \left\{\epsilon^{-1} \sum_{n=0}^{\infty} \epsilon^n \ddot{S}_n(t) + \epsilon^{-2} \left(\sum_{n=0}^{\infty} \epsilon^n \dot{S}_n(t)\right)^2\right\} \exp\left(\epsilon^{-1} \sum_{n=0}^{\infty} \epsilon^n S_n(t)\right)\,. \tag{C.3b}$$

Substituting these in Eq. (C.1) and gathering terms of order 1 and ϵ we obtain

$$\dot{S}_0^2 + \omega^2(t) = 0 \Rightarrow S_0 = \pm \int_0^t i\omega(s) ds \tag{C.4a}$$

$$\ddot{S}_0 + 2\dot{S}_0\dot{S}_1 = 0 \Rightarrow S_1 = -\frac{1}{4} \ln\{i\omega^2(t)\} \,. \tag{C.4b}$$

Therefore, the first–order WKB approximation is

$$\begin{aligned} y(t) &\sim \mathrm{e}^{\epsilon^{-1}S_0 + S_1} \\ &\sim \omega^{-1/2}(t) \left\{ A \cos\left(\epsilon^{-1} \int_0^t \omega(s)\, ds\right) + B \sin\left(\epsilon^{-1} \int_0^t \omega(s)\, ds\right) \right\} . \end{aligned} \tag{C.5}$$

Appendix D

Dimensionless units

In the computational implementation of the methods developed in Chapters 2 - 4, we express all physical quantities in dimensionless units. Here, we present an overview of all the reduced units used in the calculations. The mass, distance, and energy are regarded as fundamental quantities and have the following material constants, respectively, as units:

- m – mass of an atom of the material under consideration. For solid argon and copper, m has the following values:

$$\begin{aligned} \text{Ar}: \ m &= 39.948 \times 1.6726 \times 10^{-27} \text{ kg} \\ \text{Cu}: \ m &= 63.55 \times 1.6726 \times 10^{-27} \text{ kg} \end{aligned} \tag{D.1}$$

- σ_0 – nearest neighbor distance for a crystal structure. For solid Ar, $\sigma_0 = 0.34$ nm, and for Cu, $\sigma_0 = 0.3615$ nm.

- e – the energy constant for the empirical interatomic potential. For solid Ar, $e = 0.0104$ eV for the Lennard-Jones potential, and for Cu, $e = 0.59$ eV for the EAM-Johnson potential.

The units of the remaining quantities are derived as appropriate combinations of these. We shall denote the normalized quantities by the superscript "$*$". Thus, the reduced energy

functional E^* has the units of e. Recall that we introduced mass-reduced coordinates in order to simplify our analyses. Consequently, all distances may be expressed in dimensionless units as

$$\boldsymbol{q}^* = \frac{\boldsymbol{q}}{\sqrt{m}\sigma_0},\ \ \bar{\boldsymbol{q}}^* = \frac{\bar{\boldsymbol{q}}}{\sqrt{m}\sigma_0},\ \ \boldsymbol{u}^* = \frac{\boldsymbol{u}}{\sqrt{m}\sigma_0}\,. \tag{D.2}$$

In the mass-reduced coordinates given in (2.1), the momentum has the unit of the square root of energy. Hence,

$$\boldsymbol{p}^* = \frac{\boldsymbol{p}}{\sqrt{e}},\ \ \sigma^* = \frac{\sigma}{\sqrt{e}}\,, \tag{D.3}$$

where σ is the standard deviation of the atomic momenta defined in the *max-ent* approach. The dimensionless unit of force is obtained as $e/\sqrt{m}\sigma_0$ since

$$\boldsymbol{f}^* = \frac{\partial E^*}{\partial \boldsymbol{q}^*} = \frac{\partial E}{\partial \boldsymbol{q}}\frac{\sqrt{m}\sigma_0}{e} = \frac{\sqrt{m}\sigma_0}{e}\,\boldsymbol{f}\,, \tag{D.4}$$

where $\boldsymbol{f}$ is the force in mass-reduced coordinates expressed in $N/\sqrt{kg}$. Similarly, the stiffness matrix K is expressed in $N/kg.m$ and, hence, it follows that

$$\mathrm{K}^* = \frac{m\sigma_0^2}{e}\,\mathrm{K}\,. \tag{D.5}$$

Since the frequencies are square roots of the eigenvalues of the stiffness matrix, K,

$$\omega^* = \sigma_0\sqrt{\frac{m}{e}}\,\omega\,. \tag{D.6}$$

The unit of temperature is e/k_B, where k_B is the Boltzmann constant and has the value 8.617×10^{-5} eV. This comes from the fact that k_BT has the unit of energy. Normalizing it

with e gives

$$T^* = \frac{k_B}{e}\,T,\;\; k_B^* = 1\,. \tag{D.7}$$

Similarly, since TS also has the unit of energy, the dimensionless unit of entropy is k_B. We note that $\hbar\omega$ also has the unit of energy, where $\hbar$ is the Planck constant. By normalizing $\hbar\omega$ with e and using Eq. (D.6), we can derive the dimensionless unit for $\hbar$ consistent with the above as

$$\hbar^* = \frac{\hbar}{\sigma_0\sqrt{m\,e}}\,. \tag{D.8}$$

Using the values of mass, energy and σ_0 in consistent units, we obtain the following values for $\hbar^*$ for Ar and Cu

$$\begin{aligned} &\text{Ar}: \;\; \hbar^* = 0.029395 \\ &\text{Cu}: \;\; \hbar^* = 0.004158\,. \end{aligned} \tag{D.9}$$

Finally, since the time enters our computations explicitly only as the time step $\triangle t$, we use the heat equation to derive a convenient dimensionless unit for the time step. The calculation is performed by normalizing Eq. (3.48) by e and all physical quantities by the appropriate constants provided above. This yields

$$\triangle t^* = \frac{\kappa\sigma_0}{k_B}\,\triangle t,\;\; \kappa^* = 1\,, \tag{D.10}$$

where κ is the conductivity of the material. For solid Ar and Cu we have the following correspondence between the reduced and the physical units:

$$\begin{aligned} &\text{Ar}: \ \kappa = 0.7 \ W\, m^{-1} K^{-1} \ \Rightarrow 1 \triangle t^* = 0.05798 \text{ ps} \\ &\text{Cu}: \ \kappa = 401 \ W\, m^{-1} K^{-1} \ \Rightarrow 1 \triangle t^* = 0.135 \text{ fs}\,. \end{aligned} \tag{D.11}$$

Bibliography

[1] N. W. Ashcroft and N. D. Mermin. *Solid state physics*. Brooks Cole, 1976.

[2] C. M. Bender and S. A. Orszag. *Advanced mathematical methods for scientists and engineers*. McGraw-Hill, 1978.

[3] F. A. Bornemann. *Homogenization in time of singularly perturbed mechanical systems*. Springer, 1998.

[4] T. Çağin, G. Dereli, M. Uludoğan, and M. Tomak. Thermal and mechanical properties of some fcc transition metals. *Physical Review B*, 59:3468–3473, 1999.

[5] P. M. Chaikin and T. C. Lubensky. *Pinciples of condensed matter physics*. Cambridge University Press, 1995.

[6] D. Chandler. *Introduction to modern statistical mechanics*. Oxford University Press, 1987.

[7] M. S. Daw and M. I. Baskes. Embedded-atom method: Derivation and application to impurities, surfaces and other defects in metals. *Physical Review B*, 29:6443–6453, 1984.

[8] S. R. deGroot and P. Mazur. *Non-equilibrium thermodynamics*. North-Holland, 1962.

[9] E. R. Dobbs and G. O. Jones. Theory and properties of solid argon. *Rep. Prog. Phys.*, 20:516–564, 1957.

[10] L. M. Dupuy, E. B. Tadmor, R. E. Miller, and R. Phillips. Finite-temperature quasicontinuum: Molecular dynamics without all the atoms. *Physical Review Letters*, 95:060202–1–060202–4, 2005.

[11] W. E and B. Engquist. Heterogeneous multiscale methods. *Communications in mathematical sciences*, 1:87–132, 2003.

[12] W. E, B. Engquist, and Z. Huang. Heterogeneous multiscale method: A general methodology for multiscale modelling. *Physical Review B*, 67:092101–1–092101–4, 2003.

[13] F. B. Hildebrand. *Introduction to numerical analysis.* Dover, 1987.

[14] T. J. R. Hughes. *The finite element method: Linear static and dynamic finite element analysis.* Dover, 2000.

[15] D. Hull and D. J. Bacon. *Introduction to dislocations.* Butterworth-Heinemann, 2001.

[16] E. Jaynes. Information theory and statistical mechanics. *Physical Review*, 106:620–630, 1957.

[17] H. Jiang, Y. Huang, and K. C. Hwang. A finite-temperature continuum theory based on interatomic potentials. *Transactions of the ASME*, 127:408–416, 2005.

[18] R. A. Johnson. Analytic nearest-neighbor model for fcc metals. *Physical Review B*, 37:3924–3931, 1988.

[19] D. Jou, J. Casas-Vázquez, and G. Lebon. *Extended irreversible thermodynamics.* Springer, 1996.

[20] C. L. Kelchner, S. J. Plimpton, and J. C. Hamilton. Dislocation nucleation and defect structure during surface nanoindentation. *Physical Review B*, 58:11085–11088, 1998.

[21] J. Knap and M. Ortiz. An analysis of the quasicontinuum method. *Journal of the Mechanics and Physics of Solids*, 49:1899–1923, 2001.

[22] C. Lanczos. *The variational principles of mechanics*. Dover, 1986.

[23] R. LeSar, R. Najafabadi, and D. Srolovitz. Finite-temperature defect properties from free-energy minimization. *Physical Review Letters*, 63:624–627, 1989.

[24] G. Lu and K. Kaxiras. An overview of multiscale simulations of materials. In *Handbook of Theoretical and Computational Nanotechnology*. American Scientific, 2005.

[25] J. Marian, J. Knap, and M. Ortiz. Nanovoid cavitation by dislocation emission in aluminum. *Physical Review Letters*, 93:165503–1–165503–4, 2004.

[26] J. Marian, J. Knap, and M. Ortiz. Nanovoid deformation in aluminum under simple shear. *Acta Materialia*, 53:2893–2900, 2005.

[27] R. E. Miller and E. B. Tadmor. The quasicontinuum method: Overview, applications and current directions. *Journal of Computer-Aided Materials Design*, 9:203–239, 2002.

[28] F. C. Nix and D. MacNair. The thermal expansion of pure metals: Copper, gold, aluminum, nickel and iron. *Physical Review*, 60:597–605, 1941.

[29] O. G. Peterson, D. N. Batchelder, and R. O. Simmons. Measurements of x-ray lattice constant, thermal expansivity, and isothermal compressibility of argon crystals. *Physical Review*, 150:703–711, 1966.

[30] D. C. Rapaport. *The art of molecular dynamics simulation.* Cambridge University Press, 1995.

[31] R. E. Rudd and J. Q. Broughton. Coarse-grained molecular dynamics: Nonlinear finite elements and finite temperature. *Physical Review B*, 72:144104–1–144104–32, 2005.

[32] C. A. Schuh, J. K. Mason, and A. C. Lund. Quantitative insight into dislocation nucleation from high-temperature nanoindentation experiments. *Nature Materials*, 4:617–621, 2005.

[33] V. Shenoy, V. Shenoy, and R. Phillips. Finite temperature quasicontinuum methods. *Materials Research Society Symposium Proceedings*, 538:465–471, 1999.

[34] V. B. Shenoy, R. Phillips, and E. B. Tadmor. Nucleation of dislocations beneath a plane strain indenter. *Journal of the Mechanics and Physics of Solids*, 48:649–673, 2000.

[35] A. H. Stroud. Some fifth degree integration formulas for symmetric regions ii. *Numerische Mathematik*, 9:460–468, 1967.

[36] A. H. Stroud. *Approximate Calculation of Multiple Integrals.* PrenticeHall, 1971.

[37] A. P. Sutton and J. Chen. Long range finnis-sinclair potentials. *Philosophical Magazine Letters*, 61:139–146, 1990.

[38] E. B. Tadmor, M. Ortiz, and R. Phillips. Quasicontinuum analysis of defects in solids. *Philosophical Magazine*, 73:1529–1563, 1996.

[39] A. F. Voter, F. Montalenti, and T. C. Germann. Extending the time scale in atomistic simulation of materials. *Annual Review of Materials Research*, 32:321–346, 2002.

[40] D. C. Wallace. *Thermodynamics of crystals.* Dover, 1972.

[41] J. H. Weiner. *Statistical mechanics of elasticity.* Dover, 2002.

[42] E. Y. Wu. A method for treating thermal expansion effects in molecular dynamics simulation for solids. *Journal of Physics: Condensed Matter*, 2:9335–9344, 1990.

[43] Z. B. Wu, D. J. Diestler, R. Feng, and X. C. Zeng. Coarse-graining description of solid systems at nonzero temperature. *Journal of Chemical Physics*, 119:8013–8023, 2003.

[44] Q. Yang, L. Stainier, and M. Ortiz. A variational formulation of the coupled thermo-mechanical boundary-value problem for general dissipative solids. *Journal of the Mechanics and Physics of Solids*, 54:401–424, 2006.

[45] D. N. Zubarev. *Non-equilibrium statistical thermodynamics.* Consultants Bureau, 1974.